Electronic Structure of Transition Metal Dichalcogenides and Molecular Semiconductors

Dissertation

Zur Erlangung des akademischen Grades
doctor rerum naturalium
(Dr. rer. nat.)
im Fach Chemie
eingereicht an der

Mathematisch-Naturwissenschaftlichen Fakultät
der Humboldt-Universität zu Berlin
von
Herrn M. Sc. Jie Ma

Präsident der Humboldt-Universität zu Berlin
Prof. Dr. Julia von Blumenthal

Dekan der Mathematisch-Naturwissenschaftlichen Fakultät
Prof. Dr. Caren Tischendorf

Gutachter:
1. Prof. Emil List-Kratochvil
2. Prof. Norbert Koch
3. Prof. Wei Chen

Tag der mündlichen Prüfung: 17.11.2022

Abstract

Two-dimensional (2D) transition metal dichalcogenides (TMDCs) are amongst the most attractive emerging materials for next-generation optoelectronic devices. To realize the superior functionality of the TMDCs related devices, a comprehensive understanding of their electronic structure, including but not limited to the impact of defects on the electronic properties and energy level alignment (ELA) at TMDCs interfaces, is essential but presently not sufficient. In an attempt to get a deep insight into the electronic properties of TMDCs and the related interfaces combined with molecular semiconductors (MSCs), we investigate i) the fundamental band structure of monolayer (ML) TMDCs and band structure renormalization induced by sulfur vacancies (SVs), in order to provide a solid foundation for a better understanding the electronic properties of polycrystalline thin films and ii) the optoelectronic properties of selected MSC/ML-TMDC interface. In addition, iii) the impact of the substrate on the electronic properties of the MSC/ML-TMDC interface is investigated for guiding device design. The characterization is mainly performed by using angle-resolved photoelectron spectroscopy (ARPES), with complementary techniques including photoluminescence (PL), Raman spectroscopies, UV-vis absorption, scanning transmission electron microscopy (TEM), and atomic force microscopy (AFM) measurements.

Firstly, the band structures of two widely used semiconducting ML-TMDCs (ML-MoS_2 and ML-WS_2) films are assessed, featuring the expected dispersion of top valence bands (VB) with global valence band maximum at the K-point of the Brillouin zone. The impact of a high density of SVs, produced by in-situ sample annealing, on the electronic properties of ML-MoS_2 and ML-WS_2 on sapphire is investigated by ARPES. The ARPES spectra indicate that the electrons from SVs-induced defect states are ionized at room temperature, resulting in free charge carriers occupying the dispersive conduction band, strong bandgap reduction due to charge carrier screening, and band structure renormalization. Such band structure renormalization could be attributed to SVs-induced compressive strains and the increased electron density by self-doping. We further demonstrate that the graphite substrate masks most of the doping-induced effects by SVs on the electronic structure of the ML-TMDCs. Eventually, the impact of O_2-exposure on the density of SVs of defective ML-MoS_2 is studied, demonstrating the possibility to passivate SVs and to help recover the pristine optoelectronic properties of defective TMDC films.

Secondly, the energy level line-up at the C_{60}/ML-WS_2 interface supported on the insulating (sapphire) and semi-metallic (HOPG) substrates are unraveled by PES, demonstrating that vacuum level alignment prevails on both substrates. Neglecting the effect of SVs-induced band renormalization on the insulating substrate, the interfacial energy diagram of C_{60}/"perfect" ML-WS_2 on both substrates is proposed, which demonstrates an identical staggered type-II level alignment for both substrates. These insights should be considered in the future design of functional heterostructures of inorganic ML and MSCs.

Finally, we study optoelectronic properties of van der Waals interfaces comprising the molecular electron acceptor 1,3,4,5,7,8-hexafluoro-tetracyano naphthoquinodimethane (F_6TCNNQ) and ML-WS_2 as a function of the abundance of SVs. Distinct optical transitions from F_6TCNNQ/defective ML-WS_2 heterostructure are observed by UV-Vis absorption spectroscopy, while those are absent from F_6TCNNQ/pristine ML-WS_2 heterostructure. The impact of defect on optical/electronic transition from F_6TCNNQ/defective ML-WS_2 heterostructure and its functional mechanisms are further correlated to the ELA at the corresponding interfaces determined from ARPES measurements.

Our findings contribute to achieving a better understanding of the impact of defects on ML-TMDC and related interfaces with MSCs considering the substrates' effect and should help refine our understanding of the electronic behavior in TMDC-related devices.

Keywords:

2D TMDCs, optoelectronic properties, energy level alignment, SVs, band structure renormalization, MSC/ML-TMDC interface, ARPES

Zusammenfassung

Zweidimensionale (2D) Übergangsmetalldichalcogenide (TMDCs) gehören zu den attraktivsten neuen Materialien für optoelektronische Bauelemente der nächsten Generation. Um die überlegene Funktionalität der mit TMDCs verbundenen Bauelemente zu realisieren, ist ein umfassendes Verständnis ihrer elektronischen Struktur, einschließlich, aber nicht beschränkt auf die Auswirkungen von Defekten auf die elektronischen Eigenschaften und die Ausrichtung der Energieniveaus (ELA) an den TMDCs-Grenzflächen, unerlässlich, aber derzeit nicht ausreichend. Um einen tieferen Einblick in die elektronischen Eigenschaften von TMDCs und den damit verbundenen Grenzflächen in Kombination mit molekularen Halbleitern (MSCs) zu erhalten, untersuchen wir i) die fundamentale Bandstruktur von Monolagen (ML) TMDCs und die durch Schwefelfehlstellen (SVs) induzierte Renormierung der Bandstruktur, um eine solide Grundlage für ein besseres Verständnis der elektronischen Eigenschaften von polykristallinen dünnen Filmen zu schaffen, und ii) die optoelektronischen Eigenschaften ausgewählter MSC/ML-TMDCs-Grenzflächen. Darüber hinaus wird iii) der Einfluss des Substrats auf die elektronischen Eigenschaften einer MSC/ML-TMDC-Grenzfläche untersucht, um das Bauelementedesign zu steuern. Die Charakterisierung erfolgt hauptsächlich durch winkelaufgelöste Photoelektronenspektroskopie (ARPES), ergänzt durch Photolumineszenz (PL), Raman-Spektroskopie, UV-Vis-Absorption, Rastertransmissionselektronenmikroskopie (TEM) und Rasterkraftmikroskopie (AFM).

Zunächst wird die Bandstruktur von zwei weit verbreiteten halbleitenden ML-TMDC-Filmen (ML-MoS_2 und ML-WS_2) untersucht, die die erwartete Dispersion der oberen Valenzbänder (VB) mit einem globalen Valenzbandmaximum am K-Punkt der Brillouin-Zone aufweisen. Die Auswirkung einer hohen Menge an SVs, die durch in-situ-Heizen der Probe erzeugt wurde, auf die elektronischen Eigenschaften von ML-MoS_2 und ML-WS_2 auf Saphir wird mit ARPES untersucht. Die ARPES-Spektren zeigen, dass SVs-bezogene Zustände bei Raumtemperatur ionisiert werden, was dazu führt, dass freie Ladungsträger das dispersive Leitungsband besetzen, die Bandlücke aufgrund von Ladungsträgerabschirmung stark reduziert wird und die Bandstruktur renormalisiert wird. Eine solche Renormalisierung der Bandstruktur könnte auf SVs-induzierte Druckspannungen und eine durch Selbstdotierung erhöhte Elektronendichte zurückzuführen sein. Wir zeigen außerdem, dass ein Graphitsubstrat den größten Teil der

durch die SVs induzierten Dotierungseffekte auf die elektronische Struktur der ML-TMDCs überdeckt. Schließlich wird die Auswirkung einer O_2-Bestrahlung auf die Dichte von SVs in defekten ML-MoS_2 untersucht, um die Möglichkeit zu demonstrieren, SVs zu passivieren und die ursprünglichen optoelektronischen Eigenschaften defekter TMDC-Filme wiederherzustellen.

Zweitens werden die Energieniveaus an der C_{60}/ML-WS_2-Grenzfläche auf isolierendem (Saphir) und halbmetallischem (HOPG) Substrat durch PES aufgedeckt, was zeigt, dass eine Anpassung der Vakuumniveaus auf beiden Substraten vorherrscht. Unter Vernachlässigung des Effekts der SVs-induzierten Bandrenormalisierung auf isolierendem Substrat wird das Grenzflächenenergiediagramm von C_{60}/"perfektem" ML-WS_2 auf beiden Substraten vorgeschlagen, das eine identische gestaffelte Typ-II-Niveauausrichtung für beide Substrate zeigt. Diese Erkenntnisse sollten bei der künftigen Entwicklung von funktionalen Heterostrukturen aus anorganischen ML und MSC berücksichtigt werden.

Schließlich untersuchen wir die optoelektronischen Eigenschaften von Van-der-Waals-Grenzflächen, die den molekularen Elektronenakzeptor 1,3,4,5,7,8-Hexafluor-Tetracyano-Naphthochinodimethan (F_6TCNNQ) und ML-WS_2 enthalten, in Abhängigkeit von der Häufigkeit der SVs. Durch UV-Vis-Absorptionsspektroskopie werden deutliche optische Übergänge von F_6TCNNQ/defekten ML-WS2-Heterostrukturen beobachtet, während diese bei F_6TCNNQ/unversehrten ML-WS_2-Heterostrukturen fehlen. Die Auswirkungen der Defekte auf die optischen/elektronischen Übergänge von F_6TCNNQ/defekten ML-WS_2 Heterostrukturen und ihre Funktionsmechanismen werden mit den ELA an den entsprechenden Grenzflächen korreliert, die durch ARPES-Messungen bestimmt wurden. Unsere Ergebnisse tragen zu einem besseren Verständnis der Auswirkungen von Defekten auf ML-TMDC und verwandte Grenzflächen mit MSCs bei, wobei auch die Auswirkungen der Substrate berücksichtigt werden, und sollten dazu beitragen, unser Verständnis des elektronischen Verhaltens in TMDC-verwandten Geräten zu verbessern.

Schlagwörter:

2D-TMDCs, optoelektronische Eigenschaften, Ausrichtung der Energieniveaus, SVs, Renormierung der Bandstruktur, MSC/ML-TMDC-Schnittstelle, ARPES

Abbreviations

AFM	Atomic force microscopy
(AR) PES	(Angle-resolved) photoelectron spectroscopy
(AR) UPS	(Angle-resolved) ultraviolet photoelectron spectroscopy
BE	Binding energy
BZ	Brillouin zone
CB/CBM	Conduction band/conduction band minimum
CT	Charge transfer
CVD	Chemical vapor deposition
DFT	Density functional theory
DI	Deionized
DOS	Density of states
EA	Electron affinity
EBE	Exciton binding energy
EDC	Energy distribution curves
$\boldsymbol{E_F}$	Fermi level
ELA	Energy level alignment
ETS/STS	Electron/scanning tunneling spectroscopy
FET	Field-effect transistor
FWHM	Full-width at half maximum
HIB	Hole injection barrier
HOMO	Highest occupied molecular orbitals
IE	Ionization energy
IMFP	Inelastic mean free path
LCAO	Linear combination of atomic orbitals
LED	Light emitting diodes

LUMO	Lowest unoccupied molecular orbitals
ML	Monolayer
MSC	Molecular semiconductor
NIR	Near inferred
PBE	Perdew-Burke-Ernzerhof
PCE	Power conversion efficiency
PL	Photoluminescence
SECO	Secondary electron cut-off
SFM/SPM	Scanning force/Scanning probe microscopy
STEM	Scanning transmission electron microscopy
TMDC	Transition metal dichalcogenide
UHV	Ultra-high vacuum
UV	Ultraviolet
VBM	Valence band/valence band maximum
XPS	X-ray photoelectron spectroscopy
Φ	Work function

Contents

1 Introduction

Two-dimensional (2D) materials represent an ever-growing research area that encompasses multiple disciplines and spans from fundamental investigations to novel device applications [1-8]. Unlike graphene with semi-metallic electronic properties [9], 2D transition metal dichalcogenides (TMDCs) with chemical composition MX_2 (e.g., with M = Mo, W and X = S, Se) can feature a finite bandgap, rendering them semiconductors with unique structural [10], (opto-)electronic [11-13], and magnetic properties [14, 15]. Remarkable properties of TMDCs associated with their decreased dimensionality include valley polarization [16], phase-stability of a monolayer (ML), the emergence of a direct bandgap [17, 18], and large exciton binding energies [19], making them promising semiconductor materials for applications [11, 20, 21] in the fields of thin-film transistors [5, 22-24], photovoltaic cells [8, 25, 26] and photodetectors [27, 28]. In addition, TMDCs are comparably chemically inert and exhibit no dangling bonds, particularly in ML form [29, 30]. This provides opportunities for the fabrication of van der Waals heterostructures built in conjunction with molecular semiconductors (MSCs) to combine the advantages of the two distinct classes of material [29, 31, 32], which can potentially exhibit advanced (or hybrid) optoelectronic properties [33, 34].

The optoelectronic properties of ML-TMDCs and MSC/ML-TMDC heterostructures can be (partially) rationalized from their electronic band structures. Therefore, it is crucial to assess the electronic structure of ML-TMDCs and understand how the energy levels at MSCs/ML-TMDCs interfaces align, in order to further optimize the performance of TMDC-based devices. Numerous studies have been devoted to characterizing the intrinsic electronic properties of the TMDC materials both theoretically [35-38] and experimentally [17, 39-43]. However, investigations regarding the impact of defects on the electronic properties of TMDCs and interfacial ELA at MSC/TMDC interfaces are still insufficient. Meanwhile, knowledge of the MSC/ML-TMDC interfaces' electronic properties supported on different substrates is needed for guiding device design, but only a few systems have been studied to date, particularly on insulating substrates.

In an attempt to achieve a better understanding of the electronic structure and the resulting energy level alignment (ELA) at MSC/ML-TMDC interfaces, in this thesis, studies of the band dispersion and sulfur vacancies (SVs) induced band structure renormalization of ML-TMDCs (ML-MoS_2 and ML-WS_2) are firstly carried out since SV is the most abundant

type of defect in mechanically exfoliated and CVD-grown samples [44, 45] and can strongly impact on the electronic structure of TMDCs [46, 47]. Based on that, the ELA at C_{60}/ML-WS_2 interfaces is investigated considering the impact of the supporting substrates [48-50]. Finally, the electronic and optical properties of the strong organic p-dopant, 1,3,4,5,7,8-hexafluoro-tetracyano naphthoquinodimethane (F_6TCNNQ), absorbed on ML-WS_2 with different defect densities supported on the sapphire substrate are investigated.

This thesis is divided in the following way: some fundamental concepts of solid state physics with the focus laid on electronic band structure are described in chapter 2. This chapter starts with introductions of different theoretical models for approaching the electronic band structure of different solids, followed by the concept of density of states (DOS) (section 2.1). The chapter continues with the models and mechanisms of the ELA at semiconductors' interfaces, associated with the description of Fermi level (E_F), band bending, and gap states (section 2.2). The fundamental aspects of TMDCs are briefly introduced in chapter 3. The crystal structure (section 3.1) and optoelectronic properties (section 3.2) of TMDCs are firstly described, with a particular focus on the electronic structure of ML-TMDCs. Then, applications of TMDCs in different fields (section 3.3) are summarized. Subsequently, section 3.4 is centered on the fabrication methods of ML-TMDCs. Chapter 4 starts with a description of sample preparation associated with a summary of relevant characteristics of used materials (section 4.1). Employed experimental techniques are introduced in section 4.2, with a detailed guide on photoelectron spectroscopy (PES), including the photoemission process and its working principles. Experimental setups are also described in this section.

Results and discussion are presented in chapter 5. It starts with the basic characterization, in terms of morphological and optical properties (section 5.1) of produced ML-TMDCs samples. Then, in section 5.2, band dispersion and SVs-induced band structure renormalization of ML-TMDCs are investigated by means of ARPES. Supported by the stimulation results (section 5.2.3), the band structure renormalizations of ML-TMDCs on the sapphire substrate are attributed to either SVs-induced compressive strain within the layer [51] and/or the increased electron density by self-doping [52]. In contrast, for ML-TMDCs on HOPG, the absence of band structure renormalization implies an indirect doping mechanism proposed in section 5.2.4 and the release of stress on HOPG compared to sapphire. Subsequently, in section 5.2.5, the passivation/healing of the SVs for ML-TMDCs can be achieved by O_2-exposure at elevated temperature in vacuum. Globally, the

results in chapter 5.2 comprehensively describe the electronic properties of TMDCs in the presence of a high density of SVs on vastly different substrates.

In section 5.3, the electronic properties of the C_{60}/ML-WS_2 interface supported on sapphire and HOPG are investigated. Vacuum level alignment is found to prevail on both substrates and, except for minor dielectric screening effects, the ELAs are similar for the most part. In addition, the interfacial energy diagram of C_{60}/"perfect" ML-WS_2 on both substrates is proposed in section 5.3.3.

In section 5.4, the change of interfacial electronic and optical properties of F_6TCNNQ absorbed on as-grown and defective ML-WS_2 on sapphire are investigated by ARPES and UV-Vis absorption. We notably identified the presence of molecular anion only in the case of F_6TCNNQ molecules deposited on defective ML-WS_2. Concomitantly, additional "hybrid" optical transitions were observed from this system. In contrast, when employing a ML-WS_2 with low defect density, the optical properties of the F_6TCNNQ/ML-WS_2 can approximately be described as a simple sum of the contribution of its individual components.

Finally, the last part of this thesis, chapter 6, closes with a summary and an outlook.

2 Fundamentals

2.1 Electronic structure theory

To get a deep understanding of the band structure of a solid, some of the concepts and terms of solid state electronic structure theory will be introduced in this section. Here, two models, known as nearly-free electron and tight-binding approximations will be briefly discussed to compute the band structure of a solid.

2.1.1 Nearly free electron approximation

In this model, we approximate that the electrons can move almost free through a solid with a perfectly periodic structure. The eigenstates for the electrons in such periodic system can be described by the time-independent Schrödinger equation [53],

$$\widehat{H}\Psi(\boldsymbol{r}) = \left(-\frac{\hbar^2}{2m}\nabla^2 + U(\boldsymbol{r})\right)\Psi(\boldsymbol{r}) = E\Psi(\boldsymbol{r}) \tag{2.1}$$

Here, $\widehat{H}$ is the Hamiltonian associated with the kinetic and potential energies of the particles. In a periodic structure, the potential obeys $U(\boldsymbol{r}) = U(\boldsymbol{r} + \boldsymbol{R})$ (R is the lattice vector). Based on Bloch's theorem [54], solutions to the Schrödinger equation can be regarded as a plane wave modulated by a periodic function as,

$$\Psi_{nk}(\boldsymbol{r}) = e^{ikr}u_{nk}(\boldsymbol{r}) \tag{2.2}$$

Here the $u_{nk}(\boldsymbol{r})$ is a lattice periodic function and can be written as $u_{nk}(r) = u_{nk}(\boldsymbol{r} + \boldsymbol{R})$. Under these conditions, energy eigenvalues $E_n(k)$ obey a periodic function of $\boldsymbol{k}$ in reciprocal space as follows, $E_n(\boldsymbol{k}) = E_n(\boldsymbol{k} + \boldsymbol{G})$, while $\boldsymbol{G} = m_1\boldsymbol{g_1} + m_2\boldsymbol{g_2} + m_2\boldsymbol{g_2}$ (m_j are integers) are reciprocal vectors.

Further, the periodic potential U can be expressed as a Fourier series with reciprocal vectors $\boldsymbol{G}$,

$$U(\boldsymbol{r}) = \sum_{\boldsymbol{G}} U_{\boldsymbol{G}}e^{i\boldsymbol{G}\boldsymbol{r}} \tag{2.3}$$

The wave function can be written as a Fourier series [55],

$$\Psi_{\boldsymbol{k}}(\boldsymbol{r}) = \sum_{\boldsymbol{k}} C_{\boldsymbol{k}}e^{i\boldsymbol{k}\boldsymbol{r}} \tag{2.4}$$

By substitution of 2.3 and 2.4 into Schrödinger equation 2.1, one can finally obtain a set of algebraic equations, formed as,

$$\left(\frac{\hbar^2 k^2}{2m} - E\right) c_{\boldsymbol{k}} + \sum_{\boldsymbol{G}} U_{\boldsymbol{G}} C_{\boldsymbol{k}-\boldsymbol{G}} = 0 \tag{2.5}$$

Therefore, one can eventually obtain energy dispersion curves by solving equation 2.5 for very $\boldsymbol{k}$ in the first Brillouin zone. Here, if one neglects the potential ($U = 0$), i.e., free electron approximate, the dispersion is rationalized as,

$$E(\boldsymbol{k}) = \frac{\hbar^2 \boldsymbol{k}^2}{2m} \tag{2.6}$$

However, neglecting the lattice potential is a special case for real solids since electron wave function is mostly determined by the atomic core. Here, we briefly discuss the equation 2.5 in the case of a one-dimensional solid with the reciprocal lattice potential as,

$$U(x) = 2U_0 cos(\boldsymbol{G}x) \tag{2.7}$$

Where $\boldsymbol{G} = 2\pi/a$, assuming the potential U_0 is much smaller than the kinetic energy of the electrons, the wave function can be expressed by first Fourier expansion,

$$\Psi_k(x) = Ae^{i\boldsymbol{k}x} + Be^{i(\boldsymbol{k}-\boldsymbol{G})x} \tag{2.8}$$

By substitution of 2.7 and 2.8 into Schrödinger equation 2.1, a set of linear equations can be obtained,

$$\begin{vmatrix} \frac{\hbar^2 \boldsymbol{k}^2}{2m} - E & U_0 \\ U_0 & (\hbar^2/2m)(\boldsymbol{k}-\boldsymbol{G})^2 - E \end{vmatrix} \begin{pmatrix} A \\ B \end{pmatrix} = 0 \tag{2.9}$$

Therefore, the energy dispersion relation is obtained as,

$$E(k) = U_0 + E_0 + \frac{\hbar^2 \boldsymbol{k}^2}{2m} \pm \sqrt{{U_0}^2 + 4E_0 \frac{\hbar^2 \boldsymbol{k}^2}{2m}} \tag{2.10}$$

Where $E_0 = \frac{\hbar^2}{2m}(\boldsymbol{G}/2)^2$. At $\pm\frac{\boldsymbol{G}}{2}$, the energy values are,

$$E_{\pm} = \frac{\hbar^2 \boldsymbol{k}^2}{2m} \pm U_0 \tag{2.11}$$

The energy difference in the equation is $2U_0$, such energy splitting at the Brillouin zone boundary is called bandgap, i.e., no electronic wave function exists within such energy gap.

2.1.2 Tight-binding approximation

In the previous section, the nearly free electron approximation was presented to explain the band occurrence of a solid with periodic potential and this model is applicable for metal

conduction electrons. However, for most solids, the electron cannot be considered as "nearly free". Here, the tight-binding model or linear combination of atomic orbitals (LCAO) will be introduced to calculate the electronic state of a solid under the approximation that the electrons are tightly bonded to the atom to which they belong [53, 56, 57]. Focus is put on the superposition of wave functions for isolated atoms while neglecting the interaction between the electrons on neighbor atoms. This approximation is applicable for a wide variety of solids, such as for electrons on the 3d orbitals of transition metals.

In tight-binding theory, the full periodic crystal Hamiltonian in the vicinity of each lattice point can be approximated by the Hamiltonian of a single atom located at the lattice point ($\widehat{H}_{at}$) [57],

$$\widehat{H}_{at}\Psi_i = \left(-\frac{\hbar^2}{2m}\nabla^2 + U_{at}(\boldsymbol{r})\right)\Psi_i = E_i\Psi_i \tag{2.12}$$

In the formula above, $U_{at}(\boldsymbol{r})$ is the potential of the isolated atom. Ψ_i is considered normalized and non-degenerated. In the tight-binding approximation, one-electron wave function is considered as the linear superposition of N degenerated atomic wave function (N is the lattice number of the crystal), written as,

$$\Psi(\boldsymbol{r}) = \sum_{\boldsymbol{r_m}} a_m \Psi_i(\boldsymbol{r} - \boldsymbol{r_m}) \tag{2.13}$$

The Ψ_i exhibits normalized property at the same lattice point and shows the orthogonality at different lattice points due to the negligible overlap, written as,

$$\int \Psi_i^* = (\boldsymbol{r} - \boldsymbol{r_n})\Psi_i(\boldsymbol{r} - \boldsymbol{r_m})d\boldsymbol{r} = \delta_{nm} \tag{2.14}$$

$\Psi(\boldsymbol{r})$ is considered as the atomic wave function at the position near every lattice point, and can be approximated by a linear combination of atomic orbitals $\Psi_i(\boldsymbol{r} - \boldsymbol{r_m})$, which obeys the Bloch function. Hence, with the coefficient $a_m = \frac{1}{\sqrt{N}}e^{i\boldsymbol{k}\boldsymbol{r_m}}$. The equation can be formed as,

$$\Psi_k(\boldsymbol{r}) = \sum_{\boldsymbol{r_m}} \frac{1}{\sqrt{N}} e^{i\boldsymbol{k}\boldsymbol{r_m}} \Psi_i(\boldsymbol{r} - \boldsymbol{r_m}) \tag{2.15}$$

Inserting 2.15 into 2.12, one can obtain,

$$\sum_{\boldsymbol{r_m}} e^{i\boldsymbol{k}\boldsymbol{r_m}} \left(E_i - E(\boldsymbol{k}) + U(\boldsymbol{r}) - U_{at}(\boldsymbol{r} - \boldsymbol{r_m})\right)\Psi_i(\boldsymbol{r} - \boldsymbol{r_m}) = 0 \tag{2.16}$$

According to the normalized property and orthogonality of Ψ_i^*, One can multiply 2.16 by Ψ_i^* and after integration, and the $E(\boldsymbol{k})$ can be obtained,

$$E(\boldsymbol{k}) = E_i + \int \Delta U(\boldsymbol{r},0)|\Psi_i(\boldsymbol{r})|^2\, d\boldsymbol{r} + \sum_{r_m \neq 0} e^{i\boldsymbol{k}\boldsymbol{r_m}} \int \Psi_i^*(\boldsymbol{r}) \Delta U(\boldsymbol{r},\boldsymbol{r_m}) \Psi_i(-\boldsymbol{r_m}) d\boldsymbol{r} \quad 2.17$$

Here, $\Delta U(r, r_m)$ refers to the energy difference between lattice periodic potential and atomic potential at r_m, which is written as, $\Delta U(\boldsymbol{r},\boldsymbol{r_m}) = U(\boldsymbol{r}) - U_{at}(\boldsymbol{r}-\boldsymbol{r_m})$. Thus, the equation 2.17 can be further simplified as,

$$E(\boldsymbol{k}) = E_i - J(0) - \sum_{n.n} J(\boldsymbol{r_m})\, e^{i\boldsymbol{k}\boldsymbol{r_m}} \quad 2.18$$

The summation is merely regarding the nearest neighbors, where the two quantities are,

$$J(0) = -\int \Delta U(\boldsymbol{r},0)|\Psi_i(\boldsymbol{r})|^2\, d\boldsymbol{r} \qquad J(\boldsymbol{r_m}) = -\int \Psi_i^*(\boldsymbol{r}) \Delta U(\boldsymbol{r},\boldsymbol{r_m}) \Psi_i(\boldsymbol{r}-\boldsymbol{r_m}) \quad 2.19$$

In addition, we use the tight-binding model to discuss a simple case, that is, to calculate the band structure of s orbital in primitive cubic. In this lattice, $\Psi_s(\boldsymbol{r})$ exhibit spherically symmetric property, that is, $\Psi_s(\boldsymbol{r}) = \Psi_s(-\boldsymbol{r})$. Meanwhile, the overlapping integral J_1 shows the same value for the nearest neighbors with the distance of a. Inserting vectors of nearest neighbors $(\pm a, 0, 0)$, $(0, \pm a, 0)$, $(0, 0, \pm a)$ into 2.18, one can obtain,

$$E(\boldsymbol{k}) = E_s - J(0) - 2J_1\left(cos\, k_x a + cos\, k_y a + cos\, k_z a\right) \quad 2.20$$

2.1.3 Density of states (DOS)

As discussed above, the band structure of a solid can be obtained under two specific approximations and describes the relations between the energy of an electron $E(\boldsymbol{k})$ and its wave vector $\boldsymbol{k}$. It is crucial to calculate the number of states available at certain energies, as called density of states (DOS) [55, 58], in order to understand the charge distribution and transportation. The quantities are the number of the states within an energy interval $[E, E + dE]$, denoted $D(E)$ [58].

$$D(E) = \frac{2}{V} \cdot \frac{V}{8\pi^3} \int \delta\boldsymbol{k}\, dS \quad 2.21$$

$D(E)$ is calculated by counting the number of vectors in the range of $[E, E + dE]$. $\delta\boldsymbol{k}$ is the vertical distance between $S(E)$ and $S(E + dE)$, where $S(E)$ refers to the surface energy plane in the first Brillouin zone with energy E. Coefficient 2 is due to the fact that every state occupies two electrons with opposite spins. Since $dE = |\nabla_k E(\boldsymbol{k})|\, \delta\boldsymbol{k}$, $D(E)$ can be determined according to the known band dispersion, formed as,

$$D(E) = \int \frac{1}{|\nabla_{\boldsymbol{k}} E(\boldsymbol{k})|} \frac{dS}{4\pi^3} \tag{2.22}$$

Since $E(\boldsymbol{k})$ is a periodic function in the reciprocal lattice, there always exist some points with $|\nabla_{\boldsymbol{k}} E(\boldsymbol{k})| = 0$. The integrated function becomes divergence and one can still get a limited value of D(E) after integration with a divergence slope of $dD(E)/dE$. Such points are called van Hove singularities and can be normally considered as the band edges of the conduction and valence band.

As mentioned above, DOS can be calculated if the band dispersion is known. Here, we will calculate the DOS near the band edge, and within that region, the bands are often nearly parabolic [57],

$$E(\boldsymbol{k}) = E_1 + \frac{\hbar^2 \boldsymbol{k}^2}{2m^*} \tag{2.23}$$

In order to get the DOS in energy space, one can calculate the DOS in k-space $N(\boldsymbol{k})$ since states are uniformly distributed in k-space. Here, we will use a finite volume cuboid with length, width, and height of L_x, L_y, and L_z as the model.

The wave function should obey the Bloch's theorem, written as,

$$\Psi(x) = e^{ik_x x} u_k(x) \tag{2.24}$$

In x-direction where $L_x = Na$ (a is the lattice spacing), considering the boundary conditions, $\Psi(0) = \Psi(L_x)$, for a periodic lattice $u_k(x) = u_k(x + Lx)$, hence, the equation can be obtained as,

$$k_x L_x = 2\pi j \;\; j = 1, 2, 3 \ldots \tag{2.25}$$

The number of states at the range of $[k_x, k_x + dk_x]$ is $\frac{dk_x}{2\pi/L_x}$, formed as,

$$N_k dk = \frac{2dk_x}{2\pi/L_x} \tag{2.26}$$

The density of states in k-space for 1D, 2D, and 3D spaces can be calculated as,

$$\begin{aligned} N_k &= \frac{L}{\pi}, for\ 1D \\ N_k &= \frac{A}{2\pi^2}, for\ 2D \\ N_k &= \frac{V}{4\pi^3}, for\ 3D \end{aligned} \tag{2.27}$$

Then relations of the density of states per unit energy can be written as,

$$D_{1D}(E)dE = \frac{N_k}{L}dk$$
$$D_{2D}(E)dE = \frac{N_k}{A}dk^2 \qquad 2.28$$
$$D_{3D}(E)dE = \frac{N_k}{V}dk^3$$

Thus, the DOS in energy space can be obtained by inserting 2.23 into the equations 2.28 [58],

$$D_{1D}(E) = \frac{1}{\pi\hbar}\sqrt{\frac{2m^*}{E - E_1}}$$
$$D_{2D}(E) = \frac{m^*}{\pi\hbar^2} \qquad 2.29$$
$$D_{3D}(E) = \frac{m^*\sqrt{2m^*(E - E_C)}}{\pi^2\hbar^3}$$

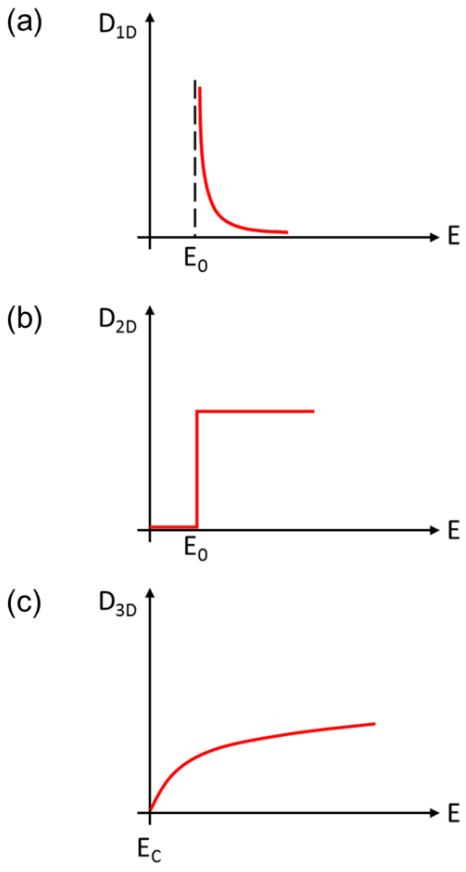

Figure 2.1 *Sketch of the density of states per unit volume and energy for (a) 1D, (b) 2D, and (c) 3D systems.*

2.2 Energy level alignment

The band structure of some specific materials was discussed through concepts of electronic structure theory and density of states in the previous subchapter. In order to optimize the performance of (opto-) electronic devices, it is also highly important to know the electronic structure upon forming the interfaces, in particular, how the energy levels of the individual materials align at interfaces. The key metrics to characterize the alignment at the interfaces are the relative positions of the valence band maximum and conduction band minimum (known as highest occupied and lowest unoccupied molecular orbitals for organic semiconductors) with respect to the Fermi level of the substrate, which determines the injection barrier at the electrodes/semiconductor interfaces [59, 60]. In this chapter, Fermi level will be defined at 2.2.1 followed by a brief description of doping mechanism in section 2.2.2. Then, two fundamental models, i.e., vacuum level alignment and Fermi level pinning are shortly discussed in sections 2.2.3 and 2.2.4.

2.2.1 Fermi level

Fermi level (E_F) [56] is one of the fundamental concepts to analyze the energy levels in a solid. The probability that a state with energy is occupied by an electron in equilibrium is given by the Fermi-Dirac distribution,

$$f(E) = \frac{1}{e^{\frac{E-E_F}{k_B T}} + 1} \tag{2.30}$$

In the function above, k_B refers to the Boltzmann constant ($\approx 1.38\times10^{-23}\ J{\cdot}K^{-1}$) and T is the absolute temperature. E_F is the Fermi-level of a solid that is defined as a hypothetical energy level with a 50% probability of occupation in equilibrium. In a metal, the boundary between the occupied and unoccupied states is marked by E_F, and that makes the ionization energy equals to their work function. On the other hand, in a nondegenerate semiconductor, E_F is generally located somewhere within the bandgap where no states exist, which is the reason why it is considered as a "hypothetical" level. As shown in schematic **Figure 2.2** for Fermi-Dirac distribution, the electron occupation probabilities are close to 1 for the states with energy much lower than the E_F and approache to 0 for the states with energy way above the E_F. There is some transition between 1 and 0 with a width of a few $k_B T$ which is in positive correlation to the temperature of a semiconductor.

It becomes a step function at absolute 0 K, and in this case, all the states below the E_F are filled, while the states above the E_F are empty.

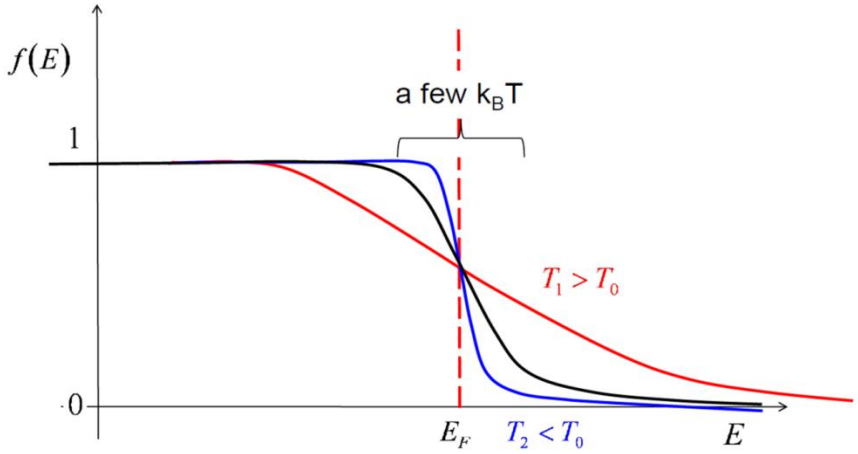

Figure 2.2 *Sketch of the temperature dependence Fermi-Dirac distribution. Red, black, and blue curves refer to Fermi functions at different temperatures.*

Electron and hole distribution at given energy in CB and VB can be determined, respectively [61],

$$n(E)dE = D_C(E)f(E)dE \qquad p(E)dE = D_V(E)[1 - f(E)]dE \qquad 2.31$$

D_c and D_v are the density of states in the conduction and valence bands, respectively. Here, we discuss the case of a nondegenerate semiconductor with parabolic bands structure as mentioned in section 2.1.3. Since the E_F is at least $3k_BT$ away from the band edges, the equation 2.31 related formula can be approximated as,

$$n(E) \propto \sqrt{E - E_C}e^{-(E-E_F)/k_BT} \qquad p(E) \propto \sqrt{E_V - E}e^{(E-E_F)/k_BT} \qquad 2.32$$

From 2.32, we notice most of the electrons and holes are close to the band edges.

Further, the total number of electrons in the conduction band and holes in the valence band can be calculated in the following,

$$n = \int_{E_C}^{E_{top}} f(E)\, D_c(E)dE \qquad p = \int_{E_{bottom}}^{E_V} [1 - f(E)]\, D_v(E)dE \qquad 2.33$$

n and p can be finalized as,

$$n \approx N_C e^{(E_F-E_C)/k_BT} \qquad p \approx N_V e^{(E_V-E_F)/k_BT} \qquad 2.34$$

Where N_C and N_V represent the effective density of states in the conduction and valence band, respectively, written as,

$$N_C = \frac{1}{4}\left(\frac{2m_n^* k_B T}{\pi\hbar^2}\right)^{3/2} \qquad N_V = \frac{1}{4}\left(\frac{2m_p^* k_B T}{\pi\hbar^2}\right)^{3/2} \qquad 2.35$$

The intrinsic semiconductors feature charge neutrality, i.e., $n_i = n = p$, where n_i is the intrinsic charge density,

$$n_i = \sqrt{np} = \sqrt{N_C N_V} e^{-E_g/2k_B T} \quad 2.36$$

Here, $E_g = E_C - E_V$, therefore, the E_F position of an intrinsic semiconductor is obtained by inserting $n = p$ into equation 2.34,

$$E_F = \frac{E_g}{2} + \frac{k_B T}{2} ln \frac{N_V}{N_C} \quad 2.37$$

where $\frac{N_V}{N_C} = (\frac{m_p^*}{m_n^*})^{2/3}$, the values of the effective mass of hole and electron are proximate at room temperature, indicating the location of E_F in the middle of the bandgap.

2.2.2 Doping

Semiconductor is a material class with the conductivity between metals and insulators. (e.g., 9.65×10^9 cm^{-3} at 300 K for Si) [62]. Conductivity of an intrinsic semiconductor (E_F located close to the middle of the bandgap) is relatively low and heavily depends on the width of the bandgap, as the intrinsic carrier density increases exponentially by decreasing the bandgap value. However, the conductivity of a semiconductor can be tuned by doping to meet the various demands of functional devices. The doping mechanism will be briefly explained in the case of Si [53, 63].

Each silicon atom is bonded to 4 neighboring atoms through covalent interaction with four shared valence electrons. Doping is achieved by introducing foreign atoms into the crystal lattice to replace the Si. For example, by introducing phosphorus or arsenic with five valence electrons (Gallium or boron with three valence electrons) into the Si lattice, n-type (p-type) doping can be obtained. In the case of n-type doping, after introducing one phosphorus atom into the Si lattice, four valence electrons of phosphorus are shared with its neighboring atoms and form covalent bonds. As a result, there is one electron left which is weekly bound to the phosphorus atoms with binding energy less than 0.1 eV [63].

$$E_B = -\frac{m_n^* q^4}{2(4\pi\varepsilon\hbar)^2} \quad 2.38$$

Such weak interaction can be easily broken by the thermal energy at room temperature and produce an electron that can wander around in the crystal. After that, the phosphorus atom is ionized and left with a net positive charge, called ionized donors (N_D^+). Each ionized donor donates an electron to the conduction band. Typical doping concentrations (from 10^{13} cm^{-3} for ultra-low doping to 10^{21} cm^{-3} for degenerate doping) overwhelm the intrinsic

carrier concentration (ca. 10^{10} cm^{-3}), so the concentration of electrons in the conduction band can be approximated to the concentration of ionized concentrations, $n \approx N_D^+$ and concentration of holes in the valence band is $p \approx n_i^2/N_D^+$.

In terms of p-type doping, one of the Si atoms is replaced by an atom from column III in the periodic table of elements, like Boron, three valence electrons are shared with four nearest neighbors and one of the covalent bonds is missing. The missing bond induces a hole sitting at the specific boron atom and can be filled up by adjacent electrons from neighbor Si atoms. That boron atom is negatively charged and considered an ionized acceptor (N_A^-), with the hole moving throughout the Si lattice. The concentration of holes in the valence band can be approximated as $p \approx N_A^-$.

The binding energy of donors and acceptors is very small, which means the doping atoms can be easily ionized by the thermal energy under room temperature so that the concentration of carriers can be roughly approximated by the concentration of the dopants. Thus, given the doping concentration, the E_F position of the doped semiconductors (n-type and p-type doping) can be roughly determined as,

$$E_F = E_C - k_B T ln \frac{N_C}{N_D} \qquad E_F = E_V - k_B T ln \frac{N_A}{N_V} \qquad 2.39$$

2.2.3 Gap states

The electrical properties and energy level alignment of intrinsic semiconductors can be comprehended if knowing their CB/VB positions and the bandgap. However, semiconductors with perfect crystallinity rarely exist in nature, most of which house defects which induce energy states in between the bandgap, called gap states. Gap states mostly originate from the atomic vacancies, interstitial and impurities such as oxygen defects in ZnO [64, 65] and sulfur vacancy in monolayer (ML) TMDC materials [44, 66]. Since these states are very close to the E_F, it is of paramount importance to figure out their occupation in order to grasp the change in energy level alignment. Depending on their relative position in bandgap with respect to the band edges, gap states can be classified as shallow states and deep states [67]. Energy difference between the shallow states and band edges (either CB or VB) can be in the region of several tens meV, and such small energy offsets are prone to the ionization process between the shallow states and band edges, which is similar to the doping mechanism. Thus, the shallow states are generally classified as dopant levels when discussing the energy level alignment of semiconductor with shallow states. In contract, deep states locate away from the band edges, thus the electronic

transition from deep states to the band edge are exceptionally difficult under room temperature. However, for the case of 2D semiconductors, bandgap can shrink by hundreds meV owing to the effect of substrate screening [68] and/or carrier screening [68, 69]. The bandgap shrink decreases the ionization energy of the deep states, which can probably lead to a similar ionization process as occurs for shallow states discussed above.

The optical properties of semiconductors can be influenced by the gap states as well. Luminescence occurs due to band-to-band radiative recombination (CB to VB) or via defect-mediated recombination (optical transitions between gap states and band edges). In the latter case, when considering the shallow states, only electrons (holes) in the CB (VB) can be captured by the shallow states close to CB (VB) with a non-radiative process and then recombine radiatively. Thus, the emission energy from shallow states is close to the band-to-band recombination energy. However, deep states are deemed as recombination center since they are capable to capture both electrons and holes and are considered as most effective recombination centers as the electron capture time is nearly the same as that of holes. Thus, the emission energy is much lower than the band-to-band emission for the deep states' case.

2.2.4 Band bending

The dissimilar electrochemical potential of the materials around a junction or interface will lead to carriers rearrangement until an equilibrium state is reached, as a result, a space-charge region and subsequent band bending establish around the interface [70]. It is crucial to understand the process of band bending in order to analyze the energy level alignment at the interface so that the energy losses at the interface can be minimized.

Here, a p-n homojunction is used to demonstrate the energy bending. A p-n homojunction origins from a contact of the same semiconductors with p- and n-type doping [71]. Some assumptions are made to simplify the analysis:

1. The junction is one-dimensional
2. The semiconductors are homogeneously doped.

When the p-n homojunction forms, the electrons at the interface diffuse from the n-doped semiconductor to the p-doped semiconductor with ionized donor N_D^+ left. Similarly, the holes at the interface diffuse from p-doped semiconductor to n-doped semiconductor with ionized acceptor N_A^- left. Hence, there exists a positive/negative space charge region on the side of the n/p-doped semiconductor. Then a built-in electric field is generated by the

ionized donor and acceptor with a direction from n to p-doped semiconductor, which counterbalances the diffusion process. Finally, an equilibrium state is reached where all the free carriers diffuse away from the space charge region (also called the depletion region). According to one-dimensional Poisson's equation, the build-in electric field can be calculated from,

$$\frac{dE(x)}{dx} = \frac{q}{\varepsilon_0 \varepsilon}(p - n + N_D^+ - N_A^-) \tag{2.40}$$

ε_0 and ε refer to the dielectric constant in vacuum and of the semiconductor, respectively. In equilibrium, free carrier concentration is deemed as 0 in the depletion region and the concentration of the ionization can be approximated as the concentration of dopants. Thus, at the side of the p/n-doped semiconductor, the electric field can be expressed as,

$$\frac{dE(x)}{dx} = -\frac{qN_A}{\varepsilon_0 \varepsilon} \qquad \frac{dE(x)}{dx} = \frac{qN_D}{\varepsilon_0 \varepsilon} \tag{2.41}$$

After integration of equation 2.41, a linear function of the electric field in the depletion region of the p/n-doped side can be written as,

$$E(x) = -\frac{qN_A}{\varepsilon_0 \varepsilon}(x + x_p) \qquad E(x) = \frac{qN_D}{\varepsilon_0 \varepsilon}(x - x_n) \tag{2.42}$$

The edge of the depletion region at p and n-doped semiconductor are marked as -x_p and x_n. The build-in potential in the depletion region can be obtained by the integral of the electric field. The band bending is illustrated in **Figure 2.3** (d). In this case, the bending amounts to the E_F difference of the individual n/p-doped semiconductors and can be further expressed as,

$$qV_{bi} \approx k_B T ln\left(\frac{N_A N_D}{n_i^2}\right) \tag{2.43}$$

From equation 2.43, it can be seen that the magnitude of band bending highly depends on the doping concentration.

In the case of surface states induced bending [72-74], the charged surface states act similarly as a donor/acceptor and charge carriers diffuse between surface states and the surface region of the semiconductor. As a result, the depletion and band bending regions are formed beneath the surface.

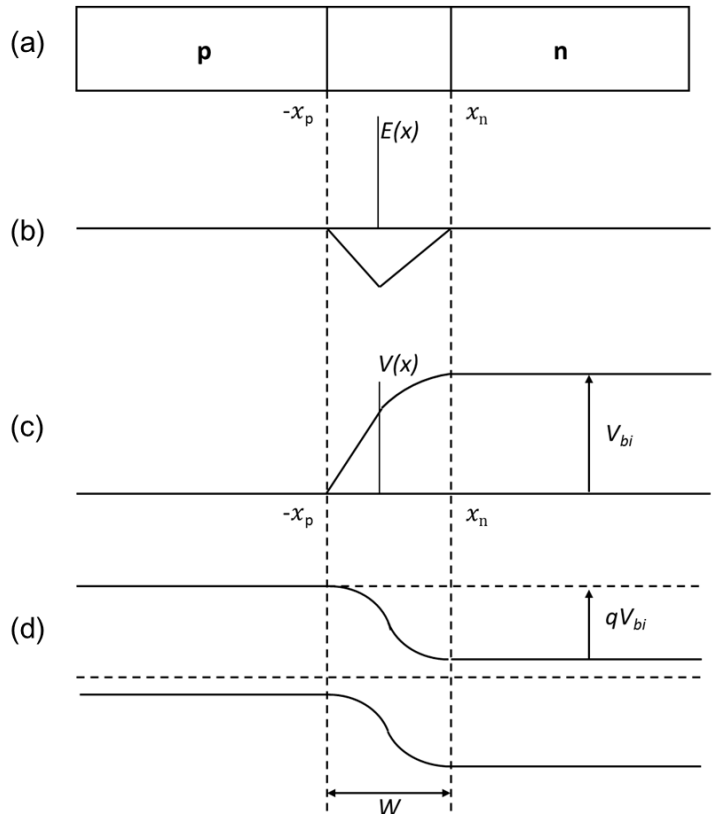

Figure 2.3 *(a) A p-n junction in thermal equilibrium with zero-bias voltage applied. Under the junction, plots for (b) the electric field, (c) the electric potential, and (d) the band diagram are reported. W refers to the width of the depletion region.*

2.2.5 Vacuum level alignment and Fermi level pinning

Vacuum level alignment (Schottky-Mott limit) [75-78] has been applied as a common assumption to understand the energy level alignment at weakly interacting interfaces. In the case of electrode/organic interfaces, when the E_F of electrode lies within the bandgap of the organic semiconductor, no charge rearrangement occurs upon contact as a result of the weak interaction between the electrode and the organic semiconductor. The energy level of these two materials can be predicted assuming a vacuum level alignment at the interface. In contrast, if the electrode E_F is located above/below the HOMO/LUMO of organic semiconductor, carriers redistribute at the electrode/organic interface to reach electrostatic equilibrium upon contact. Abrupt changes in vacuum level at the interface occur and the E_F is "pinned" just above/below the HOMO/LUMO of organic semiconductor [60, 79-81]. This is called Fermi level pinning as shown in **Figure 2.4**.

A schematic depiction of the work function of organic semiconductor ϕ_{org} as a function of electrode work function ϕ_{sub} is displayed in **Figure 2.5**. Vacuum level alignment occurs in

the energy range where $\phi_{org} = \phi_{sub}$. Slope S, defined as $S = d\phi_{org}/d\phi_{sub}$ [76], equals to 1 for this energy range. Another way to describe the situation is by plotting the hole/electron injection barriers Δh (or Δe) as a function of ϕ_{sub} and vacuum level alignment refers to the range where $S = d\Delta h(d\Delta e)/d\phi_{sub}$ equals to 1. Notable exceptions like large intrinsic dipole moment of organic semiconductors or push-back effect at metal/organic interface will induce a shift in the energy range of vacuum level alignment [81-83]. In this case, the slope is unity ($S = 1$) while $\phi_{org} \neq \phi_{sub}$. In the case of Fermi level pinning, where the ϕ_{sub} is out of the range mentioned above ($S = 0$) [79, 84-87], the ϕ_{org} remains constant upon varying ϕ_{sub}. Constant Minimal $\Delta h/\Delta e$ of ca. 0.3 eV is obtained, demonstrating that the E_F is located at ca. 0.3 eV above/below HOMO/LUMO in this situation. It is noted that the Fermi level pinning here does not require any extrinsic factors (like surface states and gap states) as the redistributed carriers are expected to originate from the electrode or organic semiconductor.

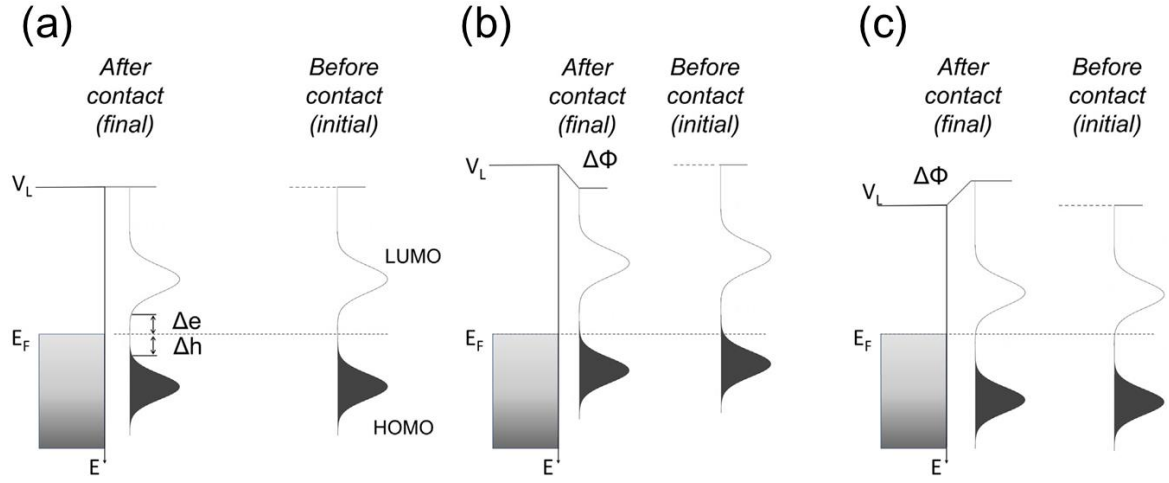

Figure 2.4 *(a) Schematic energy-level diagram corresponding to a situation where vacuum-level alignment occurs. (b, c) Schematic energy-level diagrams corresponding to situations where the HOMO and LUMO are Fermi level pinned, respectively. Figure reprinted with permission from [76]*

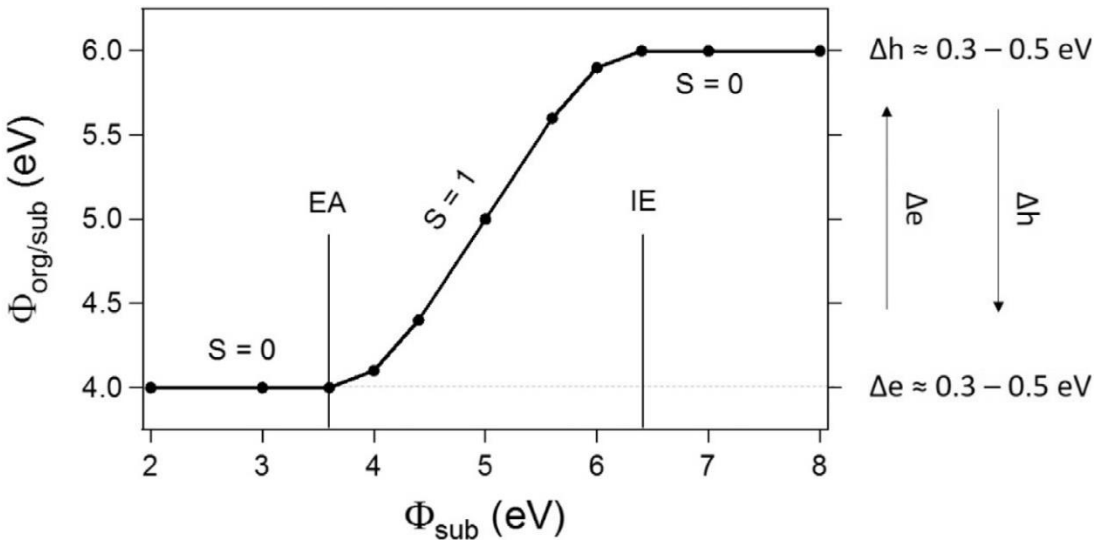

Figure 2.5 *Left axis: Work function $\phi_{org/sub}$ after deposition of an organic semiconductor as a function of the initial substrate work function ϕ_{sub}. Right axis: Injection barriers Δe and Δh for electrons and holes, respectively, as a function of ϕ_{sub}. The arrows indicate the direction of increasing Δe and Δh. The region where $S = 1$ 1 corresponds to the situation encountered in* ***Figure 2.4*** *(a). For ϕ_{sub} larger than 6 eV and lower than 4 eV, the situations correspond to* ***Figure 2.4*** *(b) and (c), respectively. Figure reprinted with permission from [76]*

3 Fundamentals of TMDCs

2D materials refer to the material where the free motion of electrons is limited to two dimensions. Research of 2D materials has been steadily growing since 2004, when the first graphene monolayer (deemed as a "dream material") was exfoliated by Andre Geim and Kostya Novoselov [88]. Due to its unique 2D structure, graphene features many excellent chemical and physical properties, such as extremely high thermal conductivity [89] and carrier mobility [88, 90] at room temperature. Meanwhile, the discovery of graphene promoted a new rush in studying of graphene-like materials [91-94]. The lack of a bandgap restricts graphene's potential applications in optoelectronic devices. Based on that, other 2D materials can fill the material gap to establish a complete 2D material system consisting of metal (graphene) [9], semiconductor (like TMDCs) [11] and insulator (like h-BN) [95, 96]. Multiple categories of 2D materials have a broad prospect in applications [10, 97-100]. A brief summary of the characteristics regarding TMDCs will be introduced in this chapter. The lattice structure of TMDCs will firstly be introduced in section 3.1. Then, the electronic structure and optoelectronic properties of bulk to monolayer TMDCs will be explicitly discussed in 3.2 and 3.3, respectively. After grasping the unique properties, applications will be briefly introduced in 3.4. Finally, experimental methods in fabrications of 2D TMDCs will be shortly summarized in 3.5.

3.1 Crystal structure of TMDCs

The chemical formula of TMDCs is MX_2, where M refers to transition metal elements like Mo, W, Ta, Nb, and X is chalcogen atoms of S, Se, and Te [101]. In this thesis, we mainly focused on S-based TMDCs including MoS_2 and WS_2. Bulk TMDCs consist of a multilayered structure and each layer, with a thickness of 6-7 Å [102, 103], is composed of two layers of S atoms with a layer of transition metal atoms sandwiched in between. Such layers are called monolayers in most cases. The atomic interaction within one layer is covalent, which is similar to other semiconductors, while the orbital hybridization in TMDC is of great difference from that in traditional semiconductors. In the formation of covalent bonding, transition metal atoms provide empty d-s-p hybridized orbitals which are bonded to the lone pair electrons generated from chalcogen atoms [103]. Such type of covalent bond is also called coordinate covalent bond (shared electrons to form a covalent

bond are supplied from one atom) with a stronger interaction between the atoms, which results in higher mechanical stability of TMDCs [104]. In addition, all bonding and non-bonding orbitals are fully occupied and participate in the formation of covalent bonds of layered TMDCs, while only anti-bonding orbitals with higher energy remain to interact with other materials or interfaces. Therefore, the absence of bonding orbitals left on the surface enables the high chemical stability of TMDCs [105].

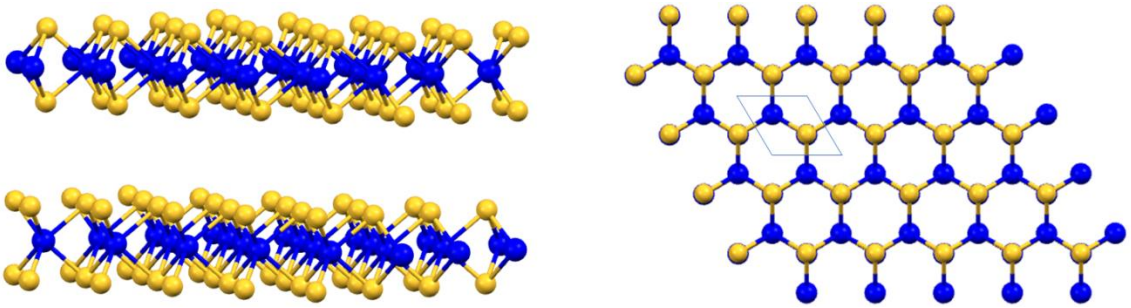

Figure 3.1 *Three-dimensional diagram of a typical layered MX_2 structure, with the metal atoms shown in blue and the chalcogen atoms shown in yellow in the left panel. The right panel shows the top view of the TMDCs hexagonal crystal structure where the unit cell is shown by the solid line.*

Three structural polytypes called $1T$, $2H$, and $3R$ are found in TMDCs, while the positions of M atoms relative to X atoms are different in these three types. The number refers to the layer number in the unit cell and the letters stand for different symmetries (see detailed description in captions of **Figure 3.2**). Distinct crystal phases arise due to the various stacking types and different coordinate types in M atoms. There are 11 different polymorphs [106] in TMDCs and the same TMDC could have different crystal structures. For instance, natural MoS_2 exhibits the $2H$ crystal structure while artificial MoS_2 (generally synthesized under high temperature and pressure) presents a structure of $3R$ [14, 101, 107].

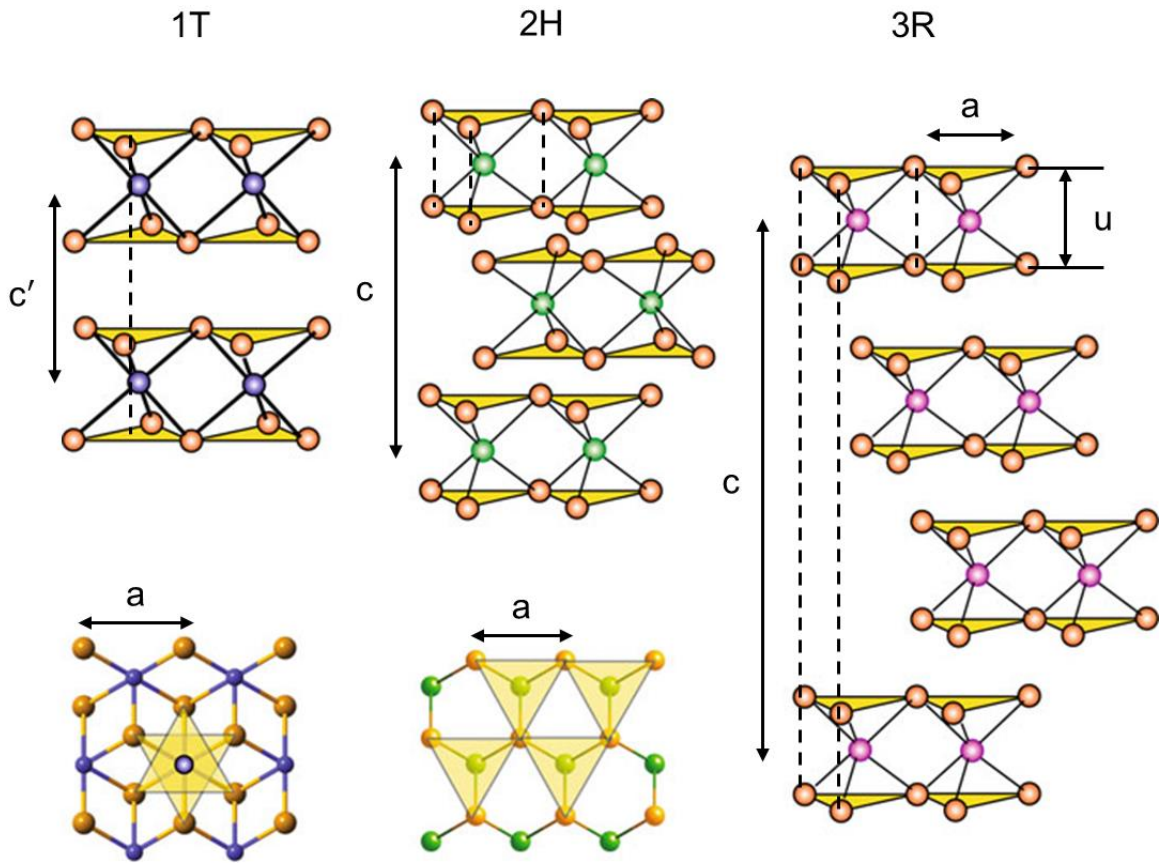

Figure 3.2 *Schematics of the structural polytypes of TMDC from left to right 1T (tetragonal symmetry, one layer per repeat, octahedral coordination of the metal), 2H (hexagonal symmetry, two layers per repeat, trigonal prismatic coordination), and 3R (rhombohedral symmetry, three layers per unit cell, trigonal prismatic coordination). The yellow-filled triangles highlight the spatial position of the chalcogen atoms. For the 1T and 2H polytypes, top views are additionally shown. Note that in these images the yellow triangles highlight spatial positions of the chalcogen species within just one layer. Figures adapted with permission from [103]*

3.2 Optoelectronic structure of TMDCs

3.2.1 Electronic structure of bulk TMDCs

The electronic structure of TMDCs mostly depends on its crystal structure and number of electrons at *d* orbitals, which gives rise to an array of electronic and magnetic properties summarized in table 1 [101, 108]. Since merely two polymorphs of trigonal prismatic and octahedral phases are found in monolayer TMDCs, the electronic structure of 2*H* and 1*T* will be discussed in this section.

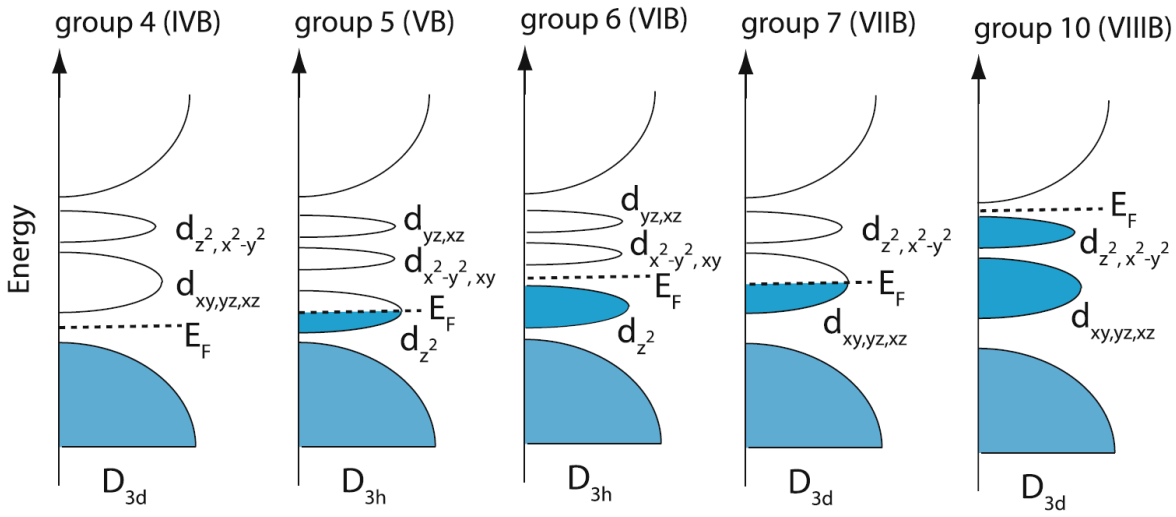

Figure 3.3 *Schematic DOS of layered TMDCs from different groups of the periodic table. Note different d-orbital splitting in structures with octahedral and trigonal prismatic geometry of transition metals. The symbols under DOS describe the symmetries of the structures. Figures reprinted with permission from [103]*

Non-bonding *d* orbitals are located between the bonding states (σ) and anti-bonding states (σ*) as shown in **Figure 3.3**. For the octahedral crystal structure (1T, tetragonal symmetry D_{3d}), two degenerate states of $d_{z^2} + d_{x^2-y^2}$ and $d_{xy} + d_{xz} + d_{yz}$ arise between σ and σ*, while three degenerate states of d_{z^2}, $d_{x^2-y^2} + d_{xy}$, and $d_{xz} + d_{yz}$ [109] form for crystal structures of trigonal prismatic coordination (2 H , hexagonal symmetry D_{3h}). As summarized in **Figure 3.3**, DOS describe different symmetries of crystal structures of TMDCs. When the highest orbitals are partially filled, indicating the E_F lies well within the continuous degenerate states (VB and VIIB), then, this kind of material groups feature metallic properties. In contrast, group IVB, VIB, and VIIB TMDCs, for which E_F locates in the gap of degenerate states, are semiconductors. We note the chalcogen atoms will change the band structure of TMDCs (broadening the d states and shrinking the bandgap), but the effect is minor compared with that of M atoms [103].

Electronic character of different layered TMDCs			
Group	M	X	Properties
4	Ti, Hf, Zr	S, Se, Te	Semiconducting ($E_g = 0.2 \sim 2$ eV). Diamagnetic
5	V, Nb, Ta	S, Se, Te	Narrow band metals ($\rho \sim 10^{-4}$ Ω cm) or semimetals. Superconducting. Charge density wave. Paramagnetic, antiferromagnetic, or diamagnetic.
6	Mo, W	S, Se, Te	Sulfides and selenides are semiconducting (E_g ~ 1 eV). Tellurides are semimetallic ($\rho \sim 10^{-3}$ Ω cm)
7	Tc, Re	S, Se, Te	Small-gap semiconductors. Diamagnetic.
10	Pd, Pt	S, Se, Te	Sulfides and selenides are semiconducting (E_g ~ 0.4 eV) and diamagnetic. Tellurides are metallic and paramagnetic. $PdTe_2$ is superconducting

Table 1. *Electronic character of different layered TMDCs. Figure adapted with permission from [101]*

3.2.2 Electronic structure of 2D TMDCs

Theoretical studies of the electronic structure of TMDCs based on first principles calculations have been rapidly grown in recent years [37], among which, two iconic models known as a tight-binding approximation and $\boldsymbol{k} \cdot \boldsymbol{p}$ model are frequently used to understand the optoelectronic and magnetic properties of mono and multilayer TMDCs [35, 36], particularly for the band edges. A more complicated three-band tight-binding model supplemented with a third-nearest-neighbor metal-metal hopping was sufficiently applied to capture the energy bands properties in the entire Brillouin zone [38]. Since the focus of this thesis is put on the S-based TMDCs, the band structure, in particular the property of indirect to direct gap transition and functional optical properties (such as the dielectric function) of group VI TMDCs (ML-MoS_2 or ML-WS_2 with 2*H* phase), will be introduced in this subsections [17, 39-43].

As presented in **Figure 3.4**, band structures calculated by density functional theory (DFT) demonstrate a variation of bandgap in TMDCs (MoS_2 and WS_2) by changing the number of layers [110]. For bulk MoS_2, known as indirect bandgap material, the valence band

maximum (VBM) locates at the Γ-point (center of hexagonal Brillouin zone) while the conduction band minimum (CBM) is at low symmetry Q (also written as Λ in some papers) point, which is between Γ- and K-point (six corners of hexagonal Brillouin zone). When the number of layers decreases to 1, the bandgap in TMDCs gradually increases, and the band edges (both VBM and CBM) will change to K-point, indicating the emergence of a direct bandgap in monolayer TMDCs. The increase in the bandgap and indirect-direct bandgap transformation of TMDCs were experimentally proved via photoluminescence (PL) measurements [17, 39, 111]. As shown in **Figure 3.5** [17], a drastic decrease in the PL intensity is observed for the bilayer of MoS_2 compared to that of their monolayer, accompanied by an occurrence of red shift of PL peak as the layer number increased, which are attributed to the indirect-direct bandgap transformation. We note the peak positions measured by PL demonstrate the exciton (bound state of electron-hole pair) energy with the same value of the optical bandgap (E_{opt}) which obeys $E_{opt} = E_g - E_B$, in which E_B refers to the exciton binding energy due to the electrostatic attraction of the free electrons in CBM and holes in VBM, normally a few hundred meV in the case of TMDCs [19, 48, 112].

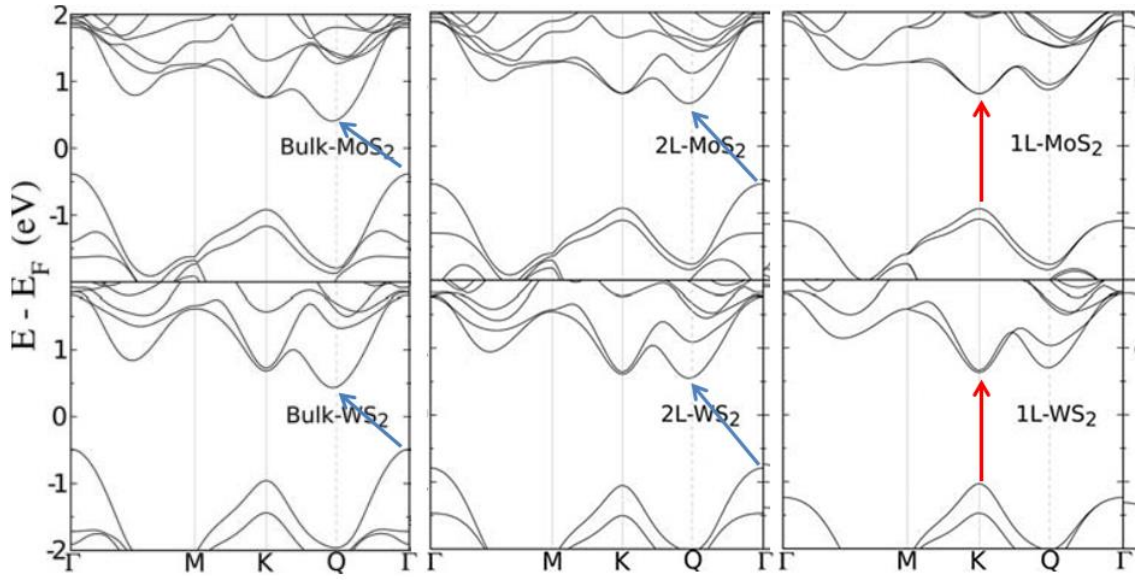

Fig. 3.4 *Band structure of single layer, bilayer, and bulk TMDCs (MoS_2 and WS_2) obtained from DFT calculations. Dashed vertical lines indicate the position of the Q-, K- and M-points in the BZ. Figures adapted with permission from [110]*

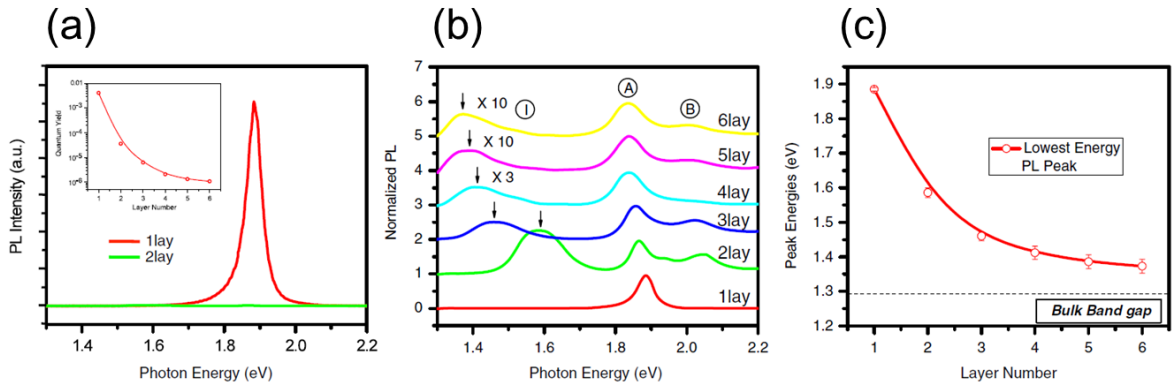

Figure 3.5 *(a) PL spectra for mono- and bilayer MoS_2 samples in the photon energy range from 1.3 to 2.2 eV. Inset: PLQY of thin layers for N = 1-6. (b) Normalized PL spectra by the intensity of peak A of thin layers of MoS_2 for N = 1-6. Feature I for N = 4-6 is magnified and the spectra are displaced for clarity. (c) Band-gap energy of thin layers of MoS_2, inferred from the energy of the PL feature I for N = 2-6 and from the energy of the PL peak A for N = 1. The dashed line represents the (indirect) band-gap energy of bulk MoS_2. Figures reprinted with permission from [17].*

3.2.3 Optical properties of 2D TMDCs

Optical dielectric function and Raman scattering, two crucial optical properties regarding group VI 2D TMDCs, will be briefly summarized in this subsection.

The dielectric function expresses a complex quantity as a function of frequency and wave number vector. Optical properties such as refractive index or reflectivity can be derived based on the function. Dielectric functions including real and imaginary parts were derived based on the experimental result of their reflectance via Kramer-Kronig constrained analysis as shown in **Figure 3.6**. The spectra of monolayer TMDCs are overall similar compared to that of the corresponding bulk TMDCs. Broadening of the features was observed in comparison to the monolayers, which can be attributed to the interlayer coupling that gives rise to additional optical transitions and carrier relaxation channels. In addition, modest red shifts of resonance energies were obtained in the bulk TMDCs dielectric function compared to that in monolayer TMDCs.

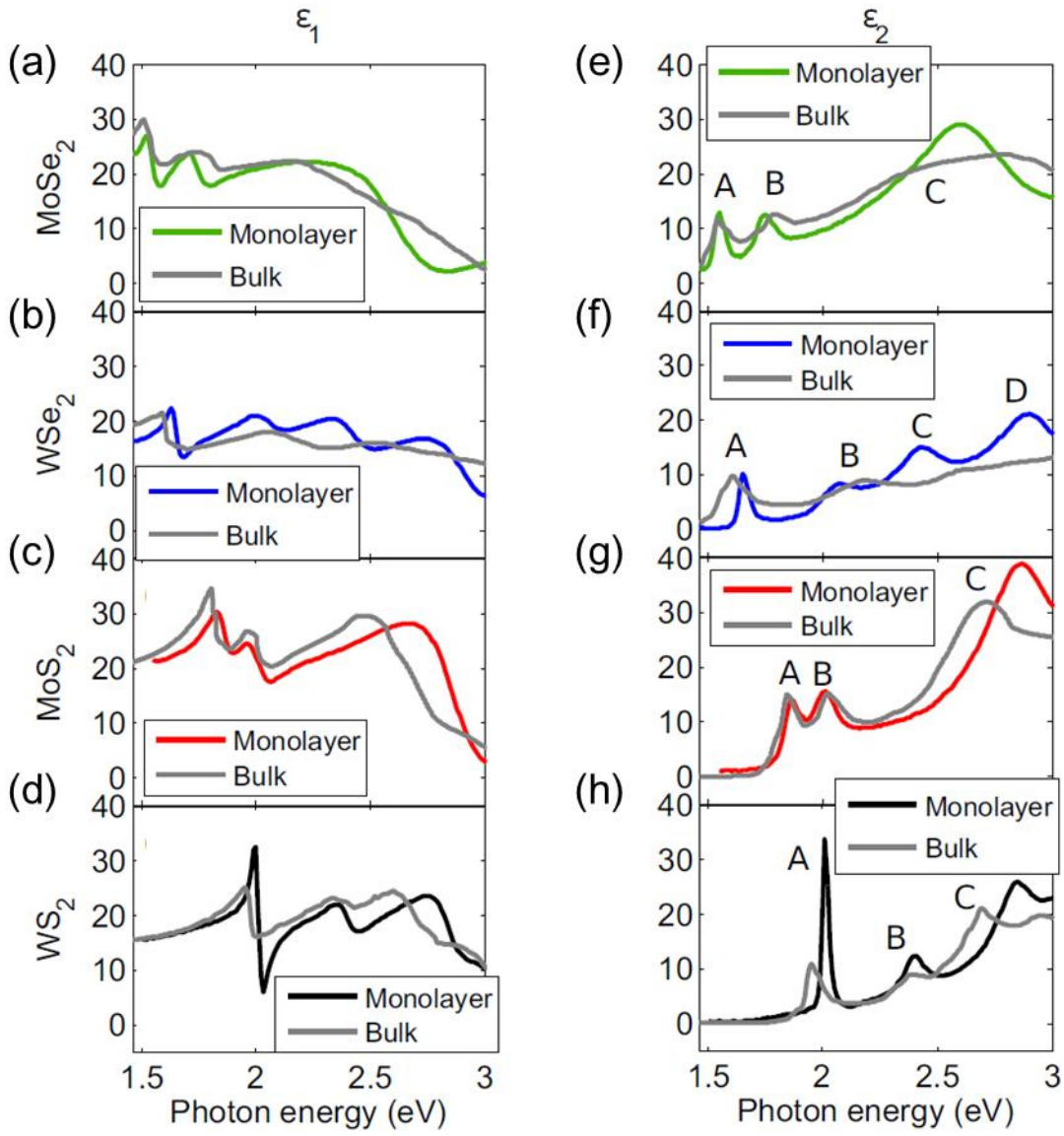

Figure 3.6 *Comparison of the dielectric functions of monolayer TMDC crystals with those of the corresponding bulk materials (gray) for (a, e) $MoSe_2$, (b, f) WSe_2, (c, g) MoS_2, and (d, h) WS_2. The peaks in ε_2 are labeled A, B, C, and D. Figures reprinted with permission from [113]*

Raman scattering is an effective measurement for the characterization of mono- and few-layer TMDCs, especially to identify the number of layers in TMDC [114-117]. A_{1g} and E^1_{2g} mode [118] of $2H$ WS_2 [117] with different thickness are clearly observed in **Figure 3.7**. A_{1g} mode at ca. 420 cm^{-1} refers to the motion of S atoms perpendicular to the WS_2 plane and E^1_{2g} around 357 cm^{-1} involves the W+S atom motion in the plane [115]. A red (blue) shift of the E^1_{2g} (A_{1g}) is obtained and the difference between E^1_{2g} and A_{1g} increases with the increasing number of layers for WS_2. The shifting trend in the frequency of A_{1g} mode is consistent with bonding interactions [103, 119] of atoms from surface to bulk

layers. The opposite of the trend for E^1_{2g} could be attributed to long-range Coulomb interlayer interaction [120]. The similar trend of A_{1g} and E^1_{2g} mode can be observed in other S or Se based TMDCs [117, 121, 122].

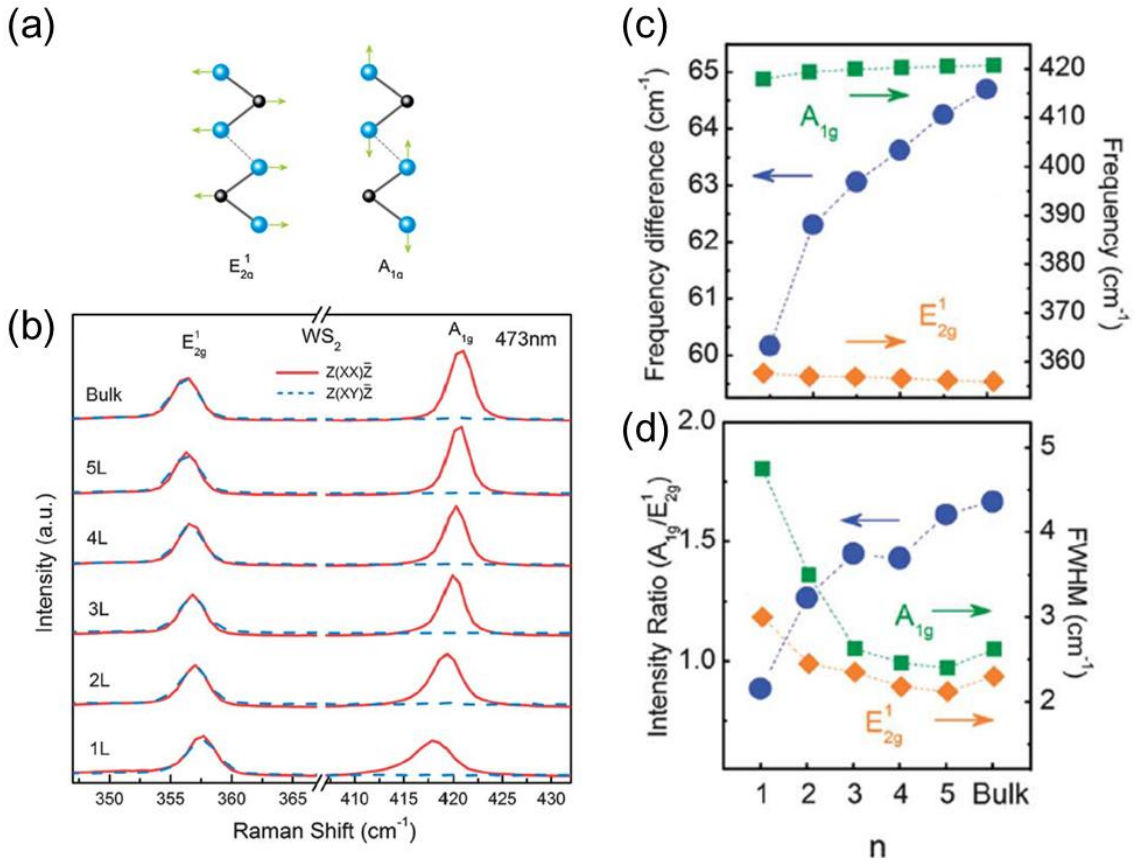

Figure 3.7 *(a) Schematics showing atomic displacement of two Raman active modes. (b) Raman spectra of 1 to 5 layers and bulk WS_2 flakes obtained in the parallel and cross-polarization conditions with 473 nm excitation. The spectra are normalized and vertically offset for clarity. (c) Position of the A_{1g} and E^1_{2g} modes (right vertical axis) and their difference (left vertical axis) as a function of the number of layers (n). (d) Intensity ratio (left vertical axis) and FWHM (right vertical axis) of A_{1g} and E^1_{2g} modes as a function of the number of layers. The spectral resolution is about 0.8 cm^{-1}. Figures adapted with permission from [117]*

3.3 Emerging applications of 2D TMDCs

So far, compared to graphene, 2D TMDCs feature outstanding properties including, but not limited to, direct bandgap [17, 39, 42, 111] which guarantees its wide applications in many fields[123] such as transistors [5, 124-127], lithium batteries [128, 129], photovoltaic devices [130-132], photodetectors [133-135], and photocatalysis [136, 137]. Some of the

representative applications, like transistors and optoelectronic devices, will be introduced in this section.

Transistors

In 2011, B. Radisavljevic and coworkers fabricated the first TMDC-based field-effect transistor (FET) with a top-gate bottom-contact structure at room temperature [5]. As presented in **Figure 3.8**, a MoS_2 layer of 6.5 Å (considered as monolayer MoS_2) achieved by the scotch tape exfoliation method was transferred to SiO_2 (270nm)/degenerately doped Si substrate as the carrier channel. Then, 50 nm gold was deposited on the ML-MoS_2 as the electrode (source and drain) and 30 nm HfO_2, which was deemed as gate dielectric material in the FET, was covered on the surface. This FET demonstrated outstanding properties such as high mobility (over 200 $cm^2\ V^{-1}\ s^{-1}$), massive current on/off ratio (10^8), and low off-state currents (25 fA/μm) at room temperature. Higher mobility (ca. 1000 $cm^2\ V^{-1}\ s^{-1}$) can be achieved by using the vacuum annealing method [124]. WS_2-based FETs were subsequently reported with slightly inferior performance (mobility ca. 200 $cm^2\ V^{-1}\ s^{-1}$, on/off ratio at ca. 10^7) [125].

Photodetector

A photodetector based on the MoS_2 transistor with a ferroelectric gate was reported [134]. The detector exhibited an ultrahigh local electrostatic field (ca. 109 V/m) by using a stale remnant polarization material polyvinydene fluoride-trifluoroethylene to depress the dark current of the semiconducting channel, which consists of a few-layer MoS_2. Such high electrostatic field demonstrates the detector with high sensitivity even without extra gate voltage. This MoS_2-based photodetector approached extremely high directivity (2.2×10^{12} Jones) and photoresponsivity (2570 A/W), additionally with a wide detecting range (0.85-1.55 μm).

Solar cell

Tunable bandgap associated with the high carrier mobility of TMDCs make them pronounced candidates for photovoltaic devices. MoS_2 and WS_2 nanosheets, serving as electron transport layers in organic solar cells, were reported with power conversion efficiencies (PCE) of 3.35% and 2.98%, respectively [130]. Photovoltaic devices based on

chemical vapor deposition-grown ML-MoS_2 were further fabricated with a PCE of 5.23% [132].

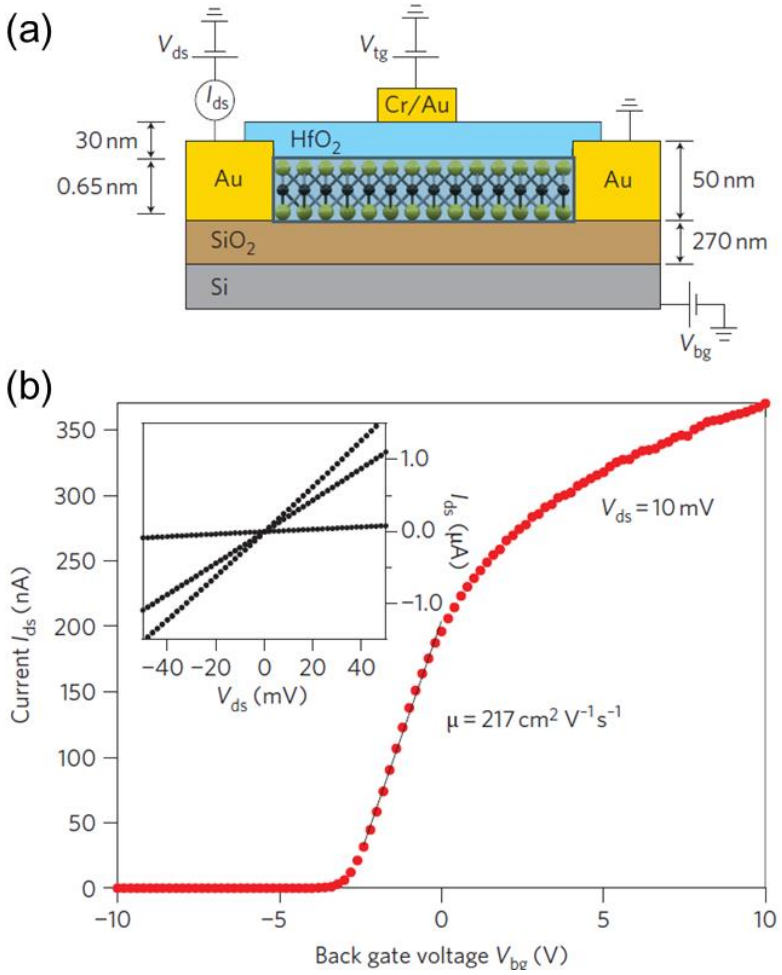

Figure 3.8 *Characterization of MoS_2 monolayer transistors. (a) Cross-sectional view of the structure of a monolayer MoS_2 FET together with electrical connections used to characterize the device. A single layer of MoS_2 (thickness 6.5 Å) is deposited on a degenerately doped silicon substrate with 270-nm-thick SiO_2. The substrate acts a back gate. One of the gold electrodes acts as drain and the other source electrode is grounded. The monolayer is separated from the top gate by 30 nm of ALD-grown HfO_2. The top gate width for the device is 4 mm and the top gate length, source–gate and gate–drain spacing are each 500 nm. (b) Room-temperature transfer characteristic for the FET with 10 mV applied bias voltage V_{ds}. Backgate voltage V_{bg} is applied to the substrate and the top gate is disconnected. Inset: I_{ds}–V_{ds} curve acquired for V_{bg} values of 0, 1 and 5 V. Figures reprinted with permission from [5]*

Light emitting devices

Due to their direct bandgaps, ML-TMDCs are regarded as potential electroluminescence materials for light-emitting diodes (LEDs). So far, ML-TMDCs based LEDs have been

successfully produced [138, 139]. However, the application of ML-TMDCs in LEDs was limited by their high power threshold for emission and their low electroluminescence efficiency (ca. 1%) [140] compared to traditional inorganic/organic LEDs (~20%) [141, 142]. In addition, LED with a stacked structure of graphene, h-BN and various ML-TMDCs exhibiting relatively high extrinsic quantum efficiency of ca. 10% [143] were reported, which is comparable to OLEDs.

3.4 Synthesis of 2D TMDCs

Two mainstream types of approaches, known as top-down and bottom-up methods, are used to synthesize 2D TMDCs and will be briefly introduced in this section.

3.4.1 Top-down methods

The top-down methods include mechanical cleavage [144-146], liquid and chemical exfoliation [147, 148], ion interaction [149], ultrasound [147, 150] and others [151]. Among those methods, chemical exfoliation has been widely employed in multiple categories of 2D TMDCs such as MoS_2 and WS_2 after successfully producing monolayer graphene [144]. The mechanical exfoliation method is deemed as the most efficient way to fabricate 2D materials with high crystallinity.

Typical fabrication processes by using mechanical exfoliation method will be introduced as shown in **Figure 3.9**. Firstly, 2D TMDCs with appropriate thickness is peeled off from the bulk crystal and stuck to the Scotch tape. These cleaved TMDCs on the tape are further pressed to the target substrate (i.e polydimethylsiloxane) for few seconds. Mono and multilayer TMDC nanosheets are left on the substrate after striping the Scotch tape. TMDC flakes obtained by this method demonstrate ultrahigh purity which can be used for fundamental studies and even meet the requirement for device fabrications. However, the limited size and uncontrollable thickness of 2D TMDC produced by mechanical exfoliation restrict its development in large-area ML-TMDCs manufacturing.

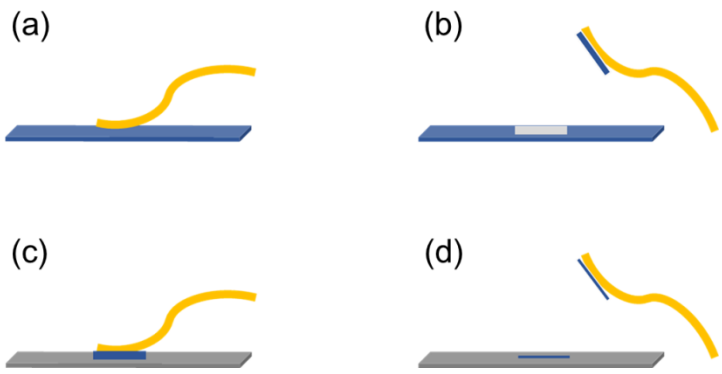

Figure 3.9 *Illustration of the mechanical cleavage technique (the Scotch tape method) for producing single or few-layer structures. From (a) to (b): The use of adhesive tape (yellow) to cleave the top few layers from a bulk crystal of the material (blue). (c) The tape with TMDC flakes is then pressed against the desired substrate (gray). (d) Some flakes stay on the substrate after removing the tape.*

3.4.2 Bottom-up methods

Since X. Li and coworkers demonstrated large-area graphene fabricated by CVD (chemical vapor deposition) [152], CVD is also regarded as an effective strategy to synthesize large area ML-TMDCs with high uniformity [153-155]. Since the thesis is focused on MoS_2 and WS_2, the CVD synthesis of ML S-based TMDCs will be introduced as followed. Two routes, known as the one-step growth route [115, 156] and the two-step growth route [157] are generally employed to obtain S-based ML-TMDCs. In the former route, gaseous M (M or MO_x) and S are introduced to form MS_2 absorbed on the substrate. While in the latter route, the substrate coated with the M-based precursor (simple substance of M simple substance or M-based compound) is sulfurized by introducing S gas. In general, the one-step growth route is considered as an effective way to synthesize wafer-scale ML-MS_2 continuous films while synthesis of single crystal domains of ML-MS_2 is approached by the two-step growth route. For the former, residues of MO_x may arise due to inappropriate reaction parameters (including but not limited to gas flow). For the latter, domain size and morphology are mainly due to the selection of precursors. In addition, high quality 2D TMDCs films are synthesized via other bottom-up methods such as magnetron sputtering [158], molecular beam epitaxy and pulsed laser deposition [159].

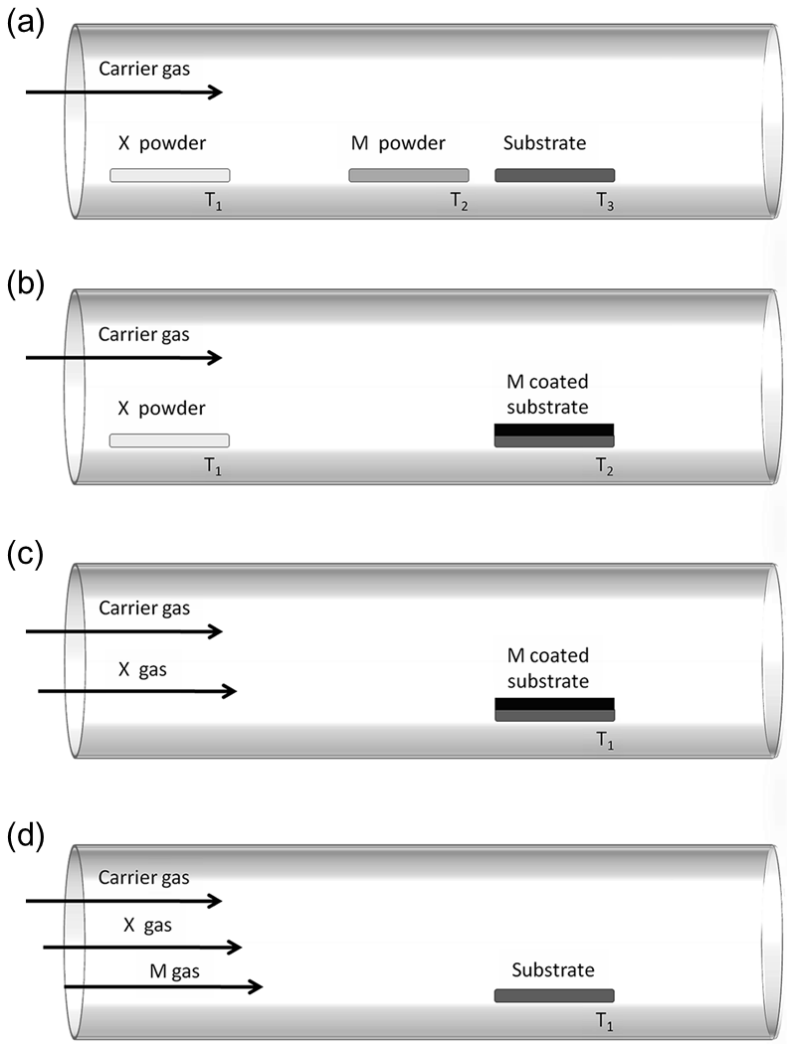

Figure 3.10 *Schematics of the most common methods used to deposit TMDCs from vapor phase. (a) Metal (M) and Chalcogen (X) powders. (b) Metal or metal oxides deposited on substrate and chalcogen powders. (c) Metal or metal oxides deposited on substrate and chalcogen supplied as gaseous precursors. (d) Metal and chalcogen compounds supplied by gaseous precursors. Figures reprinted with permission from [155]*

4 Materials and experimental setups

4.1 Materials and sample preparation

Sapphire cleaning:

Sapphire (Siegertwafer, double side polished with Ra < 0.2 nm) was employed as the substrate for TMDC growth. Sapphire wafers need to be cleaned and annealed before use. Firstly, the sapphire substrates were baked for 1 h at 1000°C in air. Then, the wafers were cut into the desired size and immersed in Piranha solution (3:1 mixture of concentrated sulfuric acid and hydrogen peroxide) for 1 h to decompose most organic materials and hydroxylate on the surface. Residual acid and other contaminations were washed by deionized water (DI water). Sapphire sheets were further cleaned by acetone, isopropanol (IPA), and DI water, each for 15 minutes, in the ultrasonic bath and dried under the flow of high purity nitrogen. Clean sapphire sheets were stored in the fume hood.

Synthesis of ML-WS_2 flakes:

ML-WS_2 flakes were synthesized by using a two-step growth route in the thesis. Solution of sodium tungstate dihydrate ($Na_2WO_4 \cdot 2H_2O$), as the W precursor, was papered by dissolving Na_2WO_4 into a solvent (3:7 mixture of DI water and IPA) with the concentration of ca. 1 mg/ml. Then Na_2WO_4 solution was spin-coated at 3000 rpm for 100 s on the sapphire substrate, followed by annealing at 100 ˚C for 10 minutes in air. The substrate coated with Na_2WO_4 was placed into the quartz tube and 2g sulfur (Sigma-Aldrich, 99,998%) was introduced upstream at low temperature region (below 250 ˚C). The tube was firstly evacuated with a rotary pump, then refilled with Ar till to the atmospheric pressure and kept a constant Ar flow of 50 sccm during the entire synthetic procedure. The temperature in the vicinity of the sapphire substrate was slowly raised (heating rate ca. 10°C/min) to 200°C for 10 minutes. This process was to remove the water of Na_2WO_4. Then the furnace was heated up to 850°C in 40 minutes, and held constant for 15 minutes. After the growth, the oven was open and fast cooled down to room temperature. The produced samples were further stored in the glove box in a dark environment to avoid unwanted degradation of the sample. The chemical reaction for the formation of WS_2 can be described as,

$$2Na_2WO_4 + 7S \rightarrow 2WS_2 + 2Na_2SO_3 + SO_2 \uparrow$$

Na_2SO_3 can be washed away during the wet transfer process, which will be discussed later.

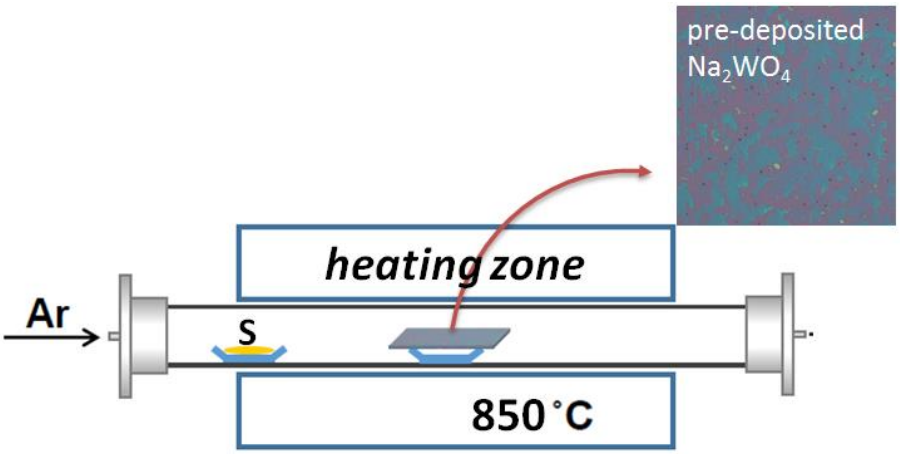

Figure 4.1 *Schematic of a two-step growth route approach to synthesizing ML-chemical vapor deposition (CVD). Insert: spin-coated Na_2WO_4 on SiO_2 substrate.*

ML-WS_2 films:

ML-WS_2 films were grown by CVD with a one-step growth route. 50 mg of WO_3 (Sigma-Aldrich, 99.995%) powder was placed in an alumina crucible in the heating zone of the furnace with a cleaned sapphire substrate placed right above the WO_3 powder. 2 g sulfur (Sigma-Aldrich, 99,998%) was introduced in a separate quartz boat at the upstream. After evacuating the tube till 10^{-2} mbar and refilling the tube with Ar till to the atmospheric pressure, the furnace was heated following the heating program,

- Slowly heat the tube to 200 °C (10 °C/min) and hold for 10 minutes.
- Heat to 900°C in 40 minutes and keeping constant for 20 minutes for the reaction.
- Turn off the heating process and open the furnace.

The chemical reaction can be described as,

$$2WO_3 + 7S \rightarrow 2WS_2 + 3SO_2 \uparrow$$

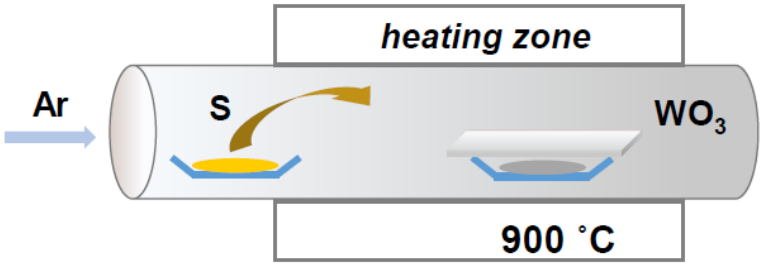

Figure 4.2 *Schematic of a one-step growth route approach to synthesize WS_2 monolayer by chemical vapor deposition (CVD).*

Wet transfer:

The as-grown ML-WS_2 was transferred from sapphire to other target substrates with the commonly used wet-transfer method [160]. The sample was spin-coated with poly (methyl methacrylate) (PMMA) (495 PMMA, Micro Chem) at 1500 rpm for 60 s and further baked at 80°C for 30 minutes. The PMMA-coated sample was kept in the fume hood overnight to form a stable film of PMMA. Hot base (KOH in DI water, 1g/ml) was then used as a substrate etchant to lift off the PMMA/WS_2 film, after which the PMMA/WS_2 film was cleaned in DI water and transferred to the HOPG substrate. The transferred sample was finally soaked in acetone for 30 min to remove PMMA.

Molecule deposition:

C_{60} powder (Sigma-Aldrich, purity >99.9%), 2,2-(perfluoronaphthalene-2,6-diylidene) dimalononitrile molecule (F_6TCNNQ, Novaled), and ruthenium pentamethylcyclopentadienyl methylene ([RuCp*(mes)]$_2$) were thermally evaporated from quartz crucibles. The crucibles were heated by the current through tantalum wire around it. The nominal thickness was monitored by a quartz crystal microbalance.

Fullerenes and their derivatives are prominent molecular semiconductors, widely employed in molecular-based optoelectronic devices [161, 162]. Due to their large bandgap [163, 164], they can be well used for investigating the subsequent energy level alignment, without inducing significant charge transfer itself.

F_6TCNNQ is a strong acceptor with a high electron affinity of 5.6 eV [165, 166], which makes it an excellent electron acceptor. High molecular weight makes them less volatile.

For [RuCp*(mes)]$_2$, during the evaporation, the dimer will break up into two monomers with a low ionization energy of 3.1 eV [167], which is sufficiently low for electron transfer to other materials.

All the deposition process was conducted in an ultrahigh vacuum (UHV) chamber at 10^{-8} mbar. The thickness of the deposited materials was monitored by a quartz crystal microbalance. The weight of a small amount of mater adsorbed on the quartz crystal can be quantified by the change of the resonance frequency [168],

$$\Delta f = -\frac{2{f_0}^2}{\sqrt{\rho_q u_q}}\frac{\Delta m}{A} \qquad 4.1$$

Where f_0 is the resonance frequency, ρ_q is the density of quartz (2.648 g/cm3), u_q is the shear modulus of quartz (2.947×1011 g/(cm·s^2)), and A is the effective area. The mass

change (Δm) can be determined by this formula, and thus the approximated thickness can be obtained according to the change of oscillation frequency with the given density of the material. Thickness of deposited materials in the thesis is considered as the nominal thickness.

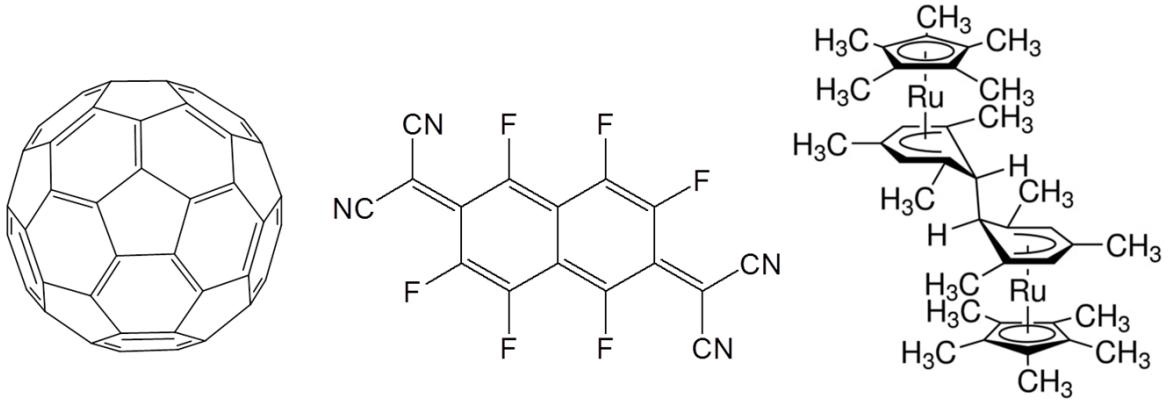

Figure 4.3 *Molecular structure of all molecules used in this thesis.*

4.2 Experimental setups

4.2.1 Optical characterization

It is of great interest to study and characterize the electronic transition between VBM (HOMO) and CBM (LOMO), which is the lowest energetic transition of the inorganic (organic) semiconductor. It can be approximately determined by the onset of the absorption (equals to the optical bandgap of the sample). The Raman Scattering is served as an effective measurement to identify the layer number of TMDCs.

4.2.1.1 UV-vis absorption

When incoming light passes through a transparent sample, the light intensity is attenuated due to the absorption of the sample and other effects such as scattering and reflection. The latter can be neglected since their attenuation contribution of light intensity is usually small compared to that of absorption [169]. The intensity of attenuation can be described by the following Beer-lambert law,

$$I = I_0 e^{-\alpha d} \qquad 4.2$$

I and I_0 are the intensity of transmitted light and incoming light, respectively. α is the absorption coefficient of the material depending on wavelength, and d is the thickness of the measured sample. The measured transmission $T = \frac{I}{I_0}$ is further converted into absorbance A,

$$A = \lg\left(\frac{I_0}{I}\right) = -lgT \qquad 4.3$$

Absorption spectra in this thesis were measured by using a LAMBDA 750 UV-vis-NIR spectrophotometer (Perkin Elmer Inc.). UV was generated by a deuterium lamp, and a tungsten-halogen lamp provided visible and near inferred (NIR) light. By cooperating optical filters with grating systems, two identical monochromatic light beams could pass through the reference sample and the measured sample. The attenuated intensity was detected via a photomultiplier for UV and visible regions and a Peltier-controlled PbS detector for NIR region.

4.2.1.2 PL and Raman Scattering

The electrons in the VB are excited to the CB via a photoexcitation process, leaving holes in the VB. Then, due to the electrostatic attraction, bounded electron-hole pair arises, which is also called exciton. Exciton can be categorized into Frenkel exciton with high exciton binding energy (EBE) (ca. 0.1-0.6eV) and Mott-Wannier exciton with low EBE (ca. 0.01eV) [170]. PL spectra are obtained by measuring the radiation energies of excitons, while Raman spectra are used to determine the vibrational mode of material due to the inelastic scattering of the photons, also known as Raman scattering. Raman spectra are obtained by detecting the energy shift of the photons from the light source, which results from the interaction between the photons and molecules in the measured sample.

Raman and PL measurements were conducted with a confocal microscope (XploRA, Horiba Ltd.)-based Raman spectrometer using a 532 nm (2.33 eV) laser. The laser was focused by a 100×objective to a spot size of about 1 μm. The excitation power was maintained at lower than 150 μW for PL measurement to avoid nonlinear optical effects and ablation. The 520 cm^{-1} phonon mode from a silicon substrate was used for calibration.

4.2.2 Scanning probe microscopy

Atomic force microscope (AFM), also called scanning probe microscopy (SPM) or scanning force microscopy (SFM), is one of the most effective methods to investigate the

topography of a sample surface (i.e. surface roughness, film thickness) on the nanoscale [171]. The surface morphology is characterized by the analysis of force between the sample surface and a sharp tip mounted to a flexible cantilever. When the tip is approaching the surface, it firstly comes out with the attractive force (Van-der Waals or permanent dipole-dipole interactions) and then the strong repelling force appear (due to the Pauli exclusion principle and repulsion of atomic nuclei) [172]. At a certain point, attractive and repelling forces are in equilibrium. The effective forces are described by the Lenard-Jones potential. This force results in the deflection of the cantilever. Thus, surface information can be obtained by monitoring the displacement of the cantilever by measuring the reflection of a laser from the cantilever onto a four-segment photodetector.

All AFM measurements in the thesis were conducted by using Bruker Icon Analyst cantilevers in ambient air based on PeakForce Tapping mode [173], where the oscillation frequency of the cantilever is set much lower than its resonance frequency.

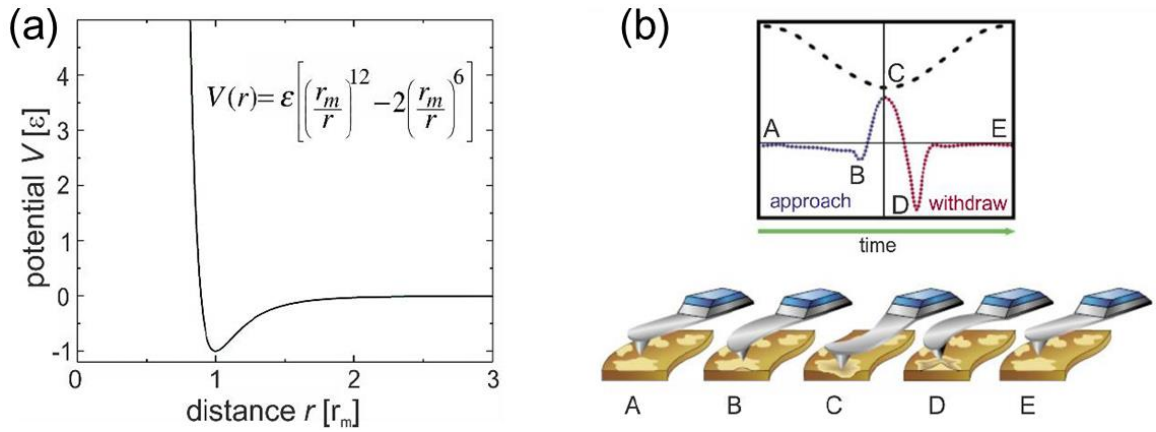

Figure 4.4 *Working principle of atomic force microscopy (AFM). a) Lennard-Jones potential, with r_m being the distance where attractive and repulsive forces are equal. b) Working principle of Bruker's Peak Force Tapping™ mode. Figures reprinted with permission from [173-175]*

4.2.3 Scanning transmission electron microscopy (STEM)

High-resolution STEM images in this thesis were obtained using a Nion HERMES aberration-corrected dedicated STEM at 60 kV acceleration voltages with 36 mrad semi-convergence angle and 72 mrad inner detector angle of the high-angle annular dark-field detector. Series of fast images were acquired, rigidly registered and integrated utilizing the Nion Swift software suite [176] to reduce scanning and sample movement artifacts. The resulting images were then processed using a homemade Python-based algorithm (that makes use of the Trackpy [177] and OpenCV [178] libraries) to automatically find SVs

and highlight and count them. The code finds all atom positions, integrates the HAADF intensity for each and displays these values in a histogram.

4.2.4 Photoelectron spectroscopy (PES)

Photoelectron spectroscopy, also called photoemission spectroscopy, is one of the most effective techniques to investigate the electronic properties of materials [179, 180]. PES technique is based on the external photoelectric effect, described as a manifestation of the quantum nature of light by Einstein in 1905(awarded the Nobel Prize in 1921) [181]. When light with photon energy *hv* is incident on the metal surface, electrons can be excited and escape from the solid to the vacuum with a maximum kinetic energy $E_{kin} = h\upsilon - \Phi_s$. Φ_s is the work function of the metal defined as the energy necessary to remove an electron originally at the E_F deep inside the material and place it at rest at a point in free space just outside the surface, i.e. at E_{Vac} [182-184]. The external photoelectric effect requires the energy of incident photon higher than the Φ_s. Information on the density of occupied states N can be obtained by measuring the kinetic energy distributed Intensity of the escaped photoelectrons $I(E_{kin})$ ($I \propto N$).

From the quantum mechanical point of view, photoemission process could be described as a single quantum-mechanically coherent process including all multiple-scattering events instead of several independent events, known as a one-step photoemission model [185]. However, this model consists of a sophisticated system including many-body effects and is hard to solve, thus a more intuitive three-step model is introduced to understand the photoemission process [186, 187].

4.2.4.1 Three-step model

The three-step model is generally subdivided into three independent steps

- Optical excitation of electrons in the bulk,
- Transport of the electrons to the surface,
- Escape of the photoelectron into the vacuum after transmission through the surface potential barrier.

The total photoemission intensity is determined by the product of probabilities of as-mentioned three steps. The first step donates the overall probability for the optical transition, while the scattering probabilities of electron and transmission probability through the surface are attributed to the second and third steps, respectively.

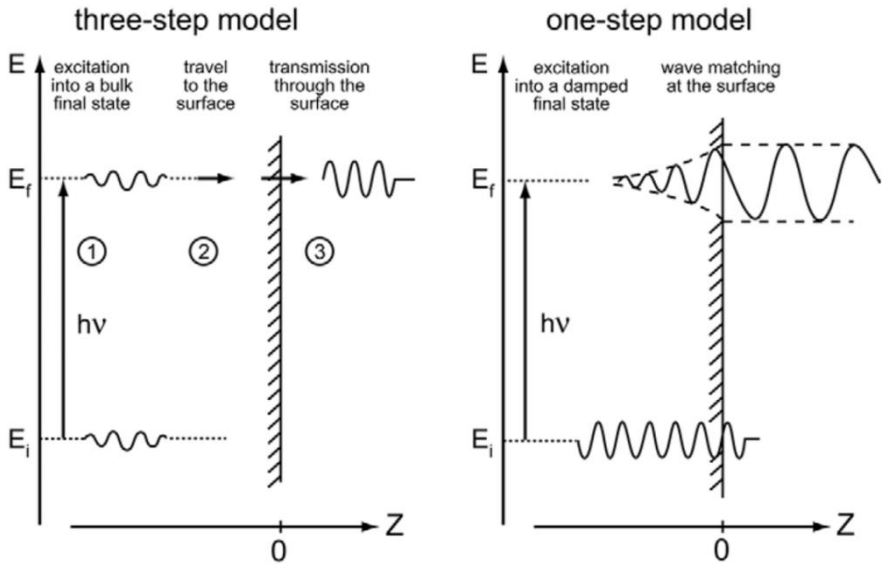

Figure 4.5 *Pictorial representation of three-step and one-step model descriptions of the photoemission process. Figures reprinted with permission from [186]*

Optical excitation of the electrons:

The probability w_{fi} for the electrons excited from an N-electron initial state Ψ_i^N to the final states Ψ_f^N can be approximated based on the Fermi's golden rule [187],

$$w_{fi} = \frac{2\pi}{\hbar}\left|\langle\Psi_f^N|\hat{H}_{int}|\Psi_i^N\rangle\right|^2\delta\left(E_f^N - E_i^N - h\nu\right) \quad 4.4$$

Where E_f^N and E_i^N refer to the energy of initial and final states in the N-electron system, respectively. The perturbation induced by the interaction with the photon is given by using $[\boldsymbol{p}, \boldsymbol{A}] = -i\hbar\boldsymbol{\nabla}\cdot\boldsymbol{A}$ and dipole approximation ($\boldsymbol{\nabla}\cdot\boldsymbol{A} = 0$ in which A keep constant over atomic dimensions),

$$\hat{H}_{int} = \frac{e}{2mc}(\boldsymbol{A}\cdot\boldsymbol{p} + \boldsymbol{p}\cdot\boldsymbol{A}) = \frac{e}{mc}\boldsymbol{A}\cdot\boldsymbol{p} \quad 4.5$$

$\boldsymbol{p}$ and $\boldsymbol{A}$ are the electronic momentum operator and electromagnetic vector potential. It should be noted that the dipole approximation is applicable for the surfaces where electromagnetic fields with weak spatial dependence.

Transport of the electron to the surface:

After optical absorption, the excited electrons may undergo inelastic scattering due to the collisions between electrons and atoms. This process results in the reduction of kinetic energy and contributes to the background in the PES spectra. Intensity of electron beams

can be determined following Lambert-Beer law $I = I_0 e^{-d/\lambda(E)}$. $\lambda(E)$ is the inelastic mean free path (IMFP) [188] defined as the distance an electron can travel where its intensity decays to $1/e$ of I_0 (initial intensity before transport) and is proportional to the probability of electron transport to the surface without scattering.

As shown in **Figure 4.6**, the energy dependence of IMFP is independent of materials. The IMFP is in the range of 5-20 Å for electron energy of 10-2000 eV (photon generated by PES system), demonstrating that the electronic structures of the topmost surface layer can be reflected from PES spectra at the valence band region.

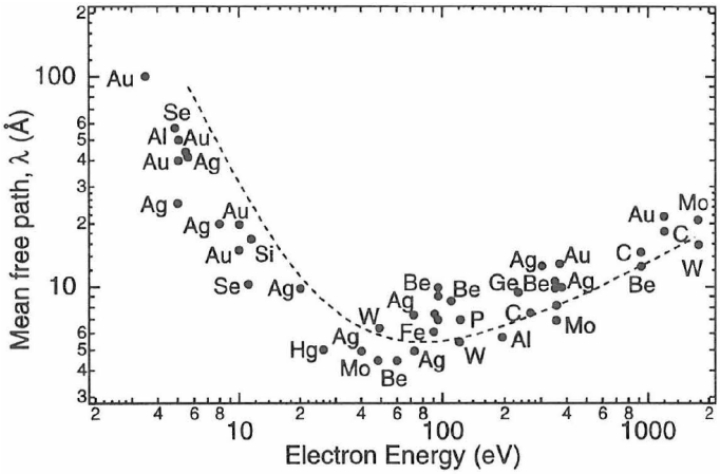

Figure 4.6 *Energy dependence of the inelastic mean free path λ for electrons in a solid. It is material independent and therefore also known as a universal curve. λ is in the order of a few nm, making photoelectron spectroscopy a very surface sensitive technique. Figure reprinted with permission from [189]*

Escape of the photoelectron into the vacuum:

The last step is described by the escaping probability of the excited electrons at the surface inside the solid into the vacuum. Apparently, the electrons need certain energy to overcome the surface potential barrier to have any finite escape probability ($\hbar k_\perp^2 \geq |E_0| + \Phi_s$. E_0 is the bottom of the valence band, and $|E_0| + \Phi_s$ is the inner potential (V_0) referring the energy difference between the bottom of the valence band and vacuum level) [186]. After that, the electrons are emitted into the vacuum in all directions. The parallel momentum wave vector is conserved when electrons pass through the surface and emit in vacuum, which can be described as $\boldsymbol{K}_\parallel = \boldsymbol{k}_\parallel = \boldsymbol{k}_\parallel + \boldsymbol{G}$, where $\boldsymbol{k}$ and $\boldsymbol{K}$ indicate the momentum inside the solid and in vacuum, respectively. The perpendicular wave vector

attenuates during this process. Valence band structure can be obtained by simultaneously collecting energy and momentum vector information of the photoelectrons.

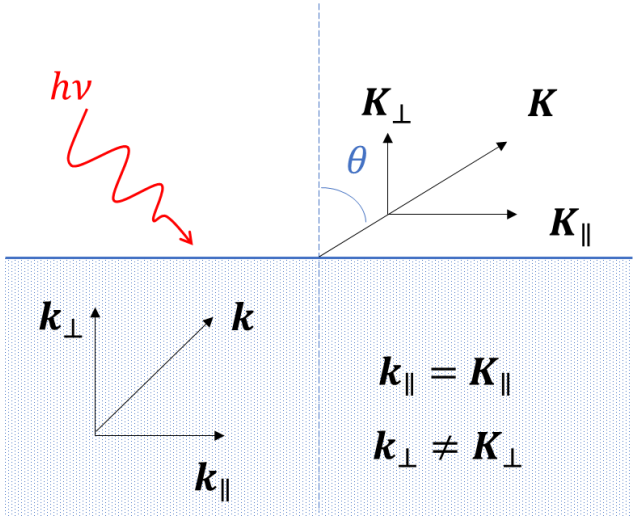

Figure 4.7 *Electron momentum relations at the solid-vacuum interface. During the photoemission process, the parallel electron momentum is conserved while the perpendicular wave vector changes.*

4.2.4.2 Characteristic parameters obtained by PES

After the escape of the photoelectron into vacuum, the photoemission spectra can be obtained by characterizing the kinetic energy of photoelectrons via an analyzer. This section will introduce how PES data are analyzed including the determination of sample work function, the analysis of valence band region, and core level.

As mentioned in the second step of photoemission, the majority of electrons undergo inelastic collisions, which leads to the reduction of their kinetic energy (called secondary electrons). Therefore, PES spectra consist of two components: i) electrons without undergoing inelastic collisions (called as primary electrons) and ii) secondary electrons. Based on the photoelectric effect, the kinetic energy of primary electrons is written as [190],

$$E_{kin} = h\upsilon - \Phi_s - E_b \qquad 4.6$$

Where E_b is the binding energy (with respect to E_F) of the electron. The primary electrons result in spectral peaks which reflect the DOS of corresponding energy levels of the sample. The binding energies of electronic states (valence band region and core levels) can be determined by referring to these primary electron peaks. Meanwhile, a continuous spectrum down to $E_{kin} = 0$ arises from secondary electrons. The Φ_s is determined by the

cut-off of the PES in the low E_{kin} region due to secondary electrons. Since the slowest secondary electrons lost their energy to $E_{kin} = 0$ after passing through the surface potential barrier, in order to effectively detect these secondary electrons by the analyzer, an external negative bias is applied to the sample.

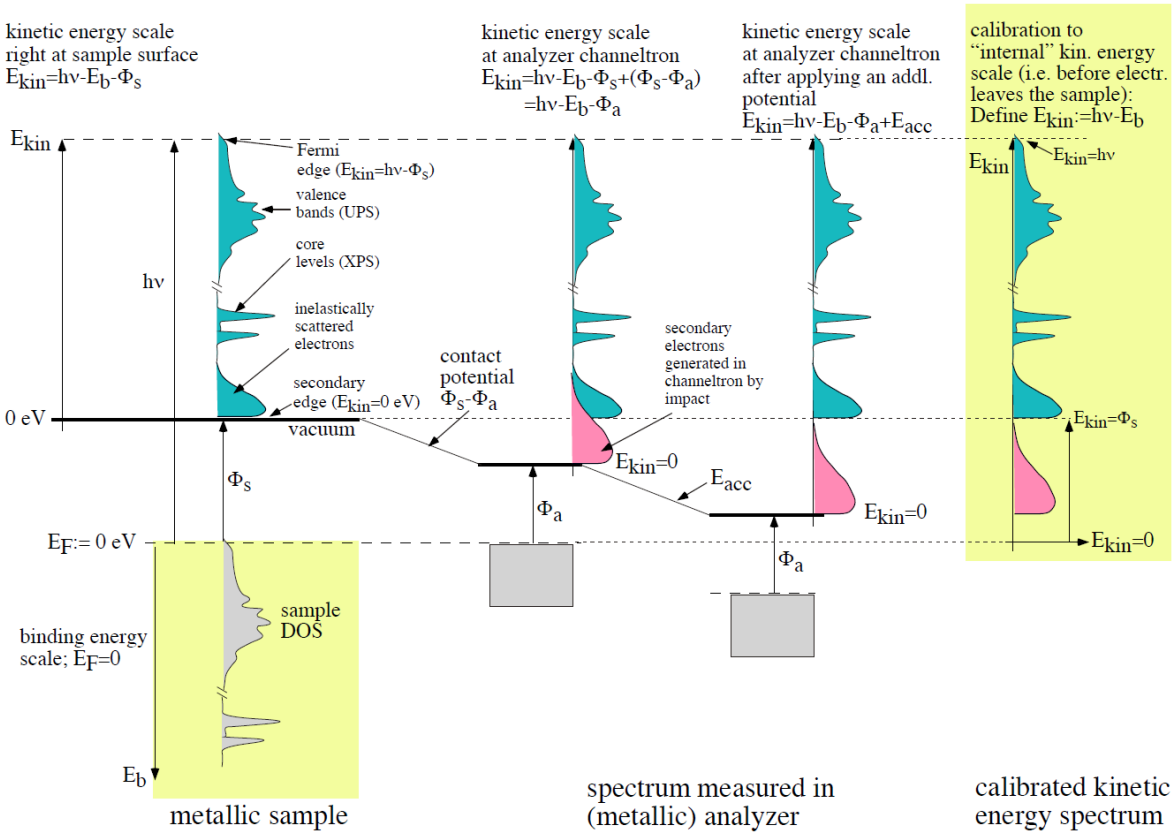

Figure 4.8 *Schematic of photoemission spectroscopy (PES) process on metallic sample. Figure reprinted with permission from [191]*

A PES spectrum of a metal sample is schematically illustrated in **Figure 4.8**. The resulting spectrum consists of the primary photoelectron with $E_{kin} = h\upsilon - \Phi_s - E_b$ and secondary electron signal. As shown on the left side, the primary photoelectrons exited from the E_F have $E_{kin} = h\upsilon - \Phi_s$, while the secondary electrons have kinetic energy down to 0 eV just at the surface. Since the analyzer is connected to the sample (their E_F is equal), the electron will be accelerated due to a contact potential of $\Phi_s - \Phi_a$ between the analyzer and sample (Φ_a is the work function of analyzer and is considered to be smaller than Φ_s here). Thus, all the E_{kin} of electrons increases by $\Phi_s - \Phi_a$, yielding $E_{kin} = h\upsilon - \Phi_a$ for the fastest primary electrons and $E_{kin} = \Phi_s - \Phi_a$ for slowest secondary electrons. The pink region refers to the secondary electrons of the analyzer generated from the collision of photoelectrons with the analyzer. Since they are not influenced by the contact potential,

one can separate the secondary edges of the analyzer and sample by applying an accelerating potential (E_{acc}). The Φ_a can be determined by the onset in the valence band region and the photon energy as $\Phi_a = h\upsilon - E_{kin}(max) + E_{acc}$. An "internal" PES spectrum is further obtained by shifting the valence band edge to the energy corresponding to the photon energy. This process is known as the calibration of PES, which needs to be done before measuring TMDCs samples. Φ_s, core level and VBM (HOMO) of a semiconductor can be determined by the secondary cut-off (SECO), VB onset and core level peak from the calibrated energy distributed spectrum.

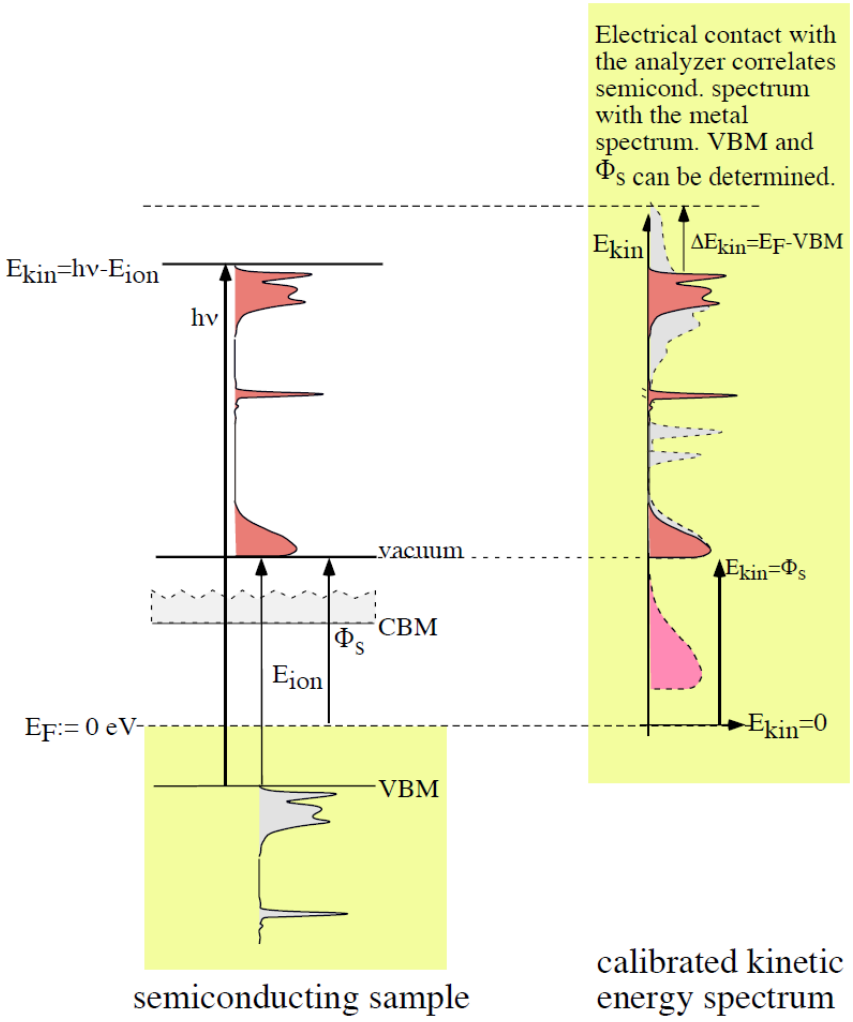

Figure 4.9 *Schematic of photoemission spectroscopy on a semiconducting sample. Figure reprinted with permission from [191]*

PES experiments are classified into two typical types depending on the photon energy [187]. One is ultraviolet photoelectron spectroscopy with photon energy in the range of 10-100 eV. The other is X-ray photoelectron spectroscopy, excited by an x-ray source with photon energy over 1000 eV.

Ultraviolet photoelectron spectroscopy (UPS)

The work function and electronic states in the valence band region ($E_b \leq 12\ eV$) are obtained by using UPS. A typical He discharged lamp is severed as the UV source with the photon energy of 21.21 eV. It features a good energy resolution (full width at half maximum ca. 8 meV) and a high flux, which is widely used for electronic structure study for functional materials in the VB (HOMO) region [80, 192-194]. For example, the hole injection barrier (HIB) between the semiconductor and the metal can be accessed by comparing the binding energy of VBM (HOMO) from the related UPS spectrum [81]. In addition, one can obtain the *IE* (ionization energy) of a material by adding the VBM to the Φ_s.

X-ray photoemission spectroscopy (XPS)

Characteristic X-ray emission lines of either Mg $\mathbf{K}_\alpha$ at 1253.6 eV or Al $\mathbf{K}_\alpha$ at 1486.6 eV are generally used for laboratory XPS to investigate the core level of the sample. The resolution can be improved by introducing a monochromator. Since each element has its characteristic emission line, the XPS is employed to identify and quantify the elements in the sample [180]. XPS is also used for obtaining information on the chemical environment and charged states of the compounds by analyzing variation and line shapes of the atomic core levels [195-197]. The number of atoms of the element (n) for a homogeneous sample is proportional to the number of photoelectrons in a peak (I), and can be given as,

$$n = I/f\sigma\theta y\lambda AT \tag{4.7}$$

Where I is the number of photoelectrons per second in a peak, which is proportional to the integrated peak area (after removing the Shirley background), f is the x-ray flux, σ is photoelectric cross-section for the atomic orbital of the interest, θ is an angular efficiency factor for the instrumental arrangement based on the angle between the photon path and the detected electrons, y is the efficiency in the photoelectric process for the formation of photoelectrons of the normal photoelectron energy, λ is the mean free path of the electron as discussed in section 4.2.3.1, A is the area of the sample from which photoelectrons are detected and T is the detection efficiency for electrons emitted from the sample. S is defined as the atomic sensitive factor, given as, $S = f\sigma\theta y\lambda AT$. The detailed value can be obtained in reference [198]. The concentration of each element c_x can be accessed as,

$$c_x = \frac{I_x/S_x}{\sum I_i/S_i} \tag{4.8}$$

4.2.4.3 Angle-resolved photoemission spectroscopy (ARPES)

In ARPES, the direct experimental study of the momentum-dependent electronic structure can be achieved by collecting the kinetic energy of photoelectrons with an analyzer by a finite acceptance angle. The modulus of wave vector from collected photoelectrons is given by $|\boldsymbol{K}| = \left|\frac{\boldsymbol{p}}{\hbar}\right| = \sqrt{2mE_{kin}}/\hbar$ [187]. The vector in three directions ($\boldsymbol{K_x}$, $\boldsymbol{K_y}$, $\boldsymbol{K_z}$) can be expressed in terms of polar θ and azimuthal φ emission angles as [186],

$$\begin{aligned} |\boldsymbol{K}_x| &= \frac{1}{\hbar}\sqrt{2mE_{kin}}\sin\theta\cos\varphi \\ |\boldsymbol{K}_y| &= \frac{1}{\hbar}\sqrt{2mE_{kin}}\sin\theta\sin\varphi \\ |\boldsymbol{K}_z| &= \frac{1}{\hbar}\sqrt{2mE_{kin}}\cos\theta \end{aligned} \tag{4.9}$$

The parallel component $\boldsymbol{K}_{\parallel} = \boldsymbol{K}_x + \boldsymbol{K}_y$ of the vector can be obtained as,

$$|\boldsymbol{K}_{\parallel}| = \frac{1}{\hbar}\sqrt{2mE_{kin}}\sin\theta \tag{4.10}$$

As discussed in section 4.2.3.1, the parallel wave vector (momentum) is conserved due to the translational symmetry in the x-y plane across the surface. Thus, the parallel wave vector in the crystal $\boldsymbol{k}_{\parallel}$ can be written as,

$$|\boldsymbol{k}_{\parallel}| = |\boldsymbol{K}_{\parallel}| = \frac{1}{\hbar}\sqrt{2mE_{kin}}\sin\theta \tag{4.11}$$

Since the perpendicular wave vector is not conserved, several specific methods have been developed to determine the value of perpendicular vector in the lattice ($\boldsymbol{k}_{\perp}$). The final states are described here by using the nearly free electron approximation as,

$$E_f(\boldsymbol{k}) = \frac{\hbar^2\boldsymbol{k}^2}{2m} - |E_0| = E_{kin} + \Phi_s \tag{4.12}$$

Where E_f is with respect to E_F, and E_{kin} is referenced to the vacuum level E_v. E_0 refers to the bottom of the valence band indicated in **Figure 4.10**. By inserting 4.8 into 4.9, one can obtain the modulus of $|\boldsymbol{k}_{\perp}|$, written as,

$$|\boldsymbol{k}_{\perp}| = \frac{1}{\hbar}\sqrt{2m(E_{kin}\cos^2\theta + V_0)} \tag{4.13}$$

$V_0 = |E_0| + \Phi_s$ is the inner potential referring to the energy difference between the bottom of the valence band and the vacuum level. The dispersion along the *z* axis can be neglected for 2D systems, thus the electronic dispersion in the case of 2D TMDCs is mostly determined by $\boldsymbol{k}_{\parallel}$.

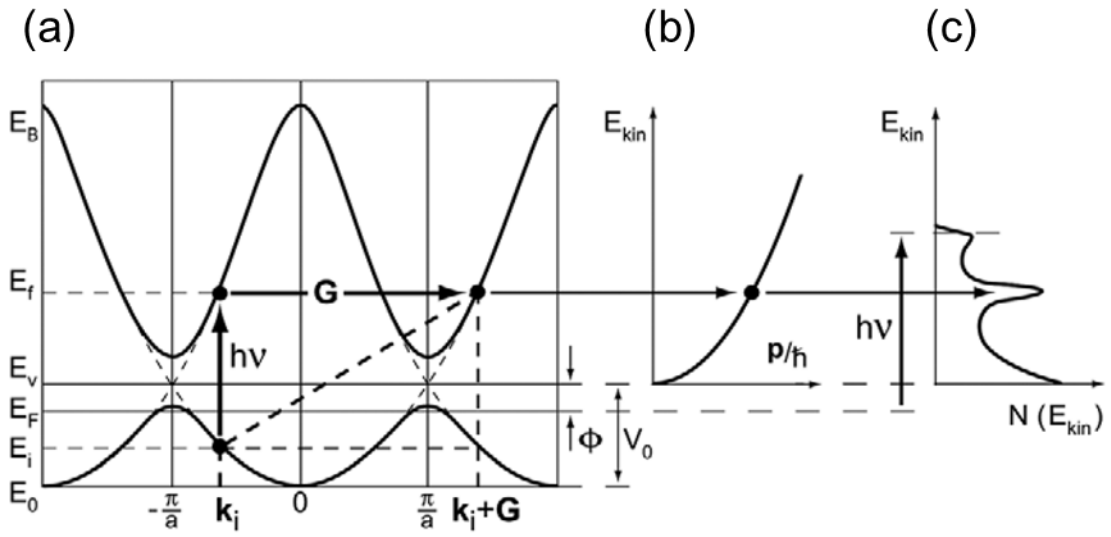

Figure 4.10 *Kinematics of the photoemission process within the three-step nearly-free-electron final state model: (a) direct optical transition in the solid (the lattice supplies the required momentum). (b) free-electron final state in vacuum. (c) corresponding photoelectron spectrum, with a background due to the scattered electrons ($E_b = 0$ at E_F). Figure reprinted with permission from [186]*

4.2.4.4 PES Set-up

Most of the PES results displayed in this thesis were performed in a UHV system composed of three main chambers (load-lock chamber, preparation chamber and analysis chamber). Samples were initially pumped down to 10^{-6}~10^{-7} mbar in the load-lock chamber. Then, we can transfer samples onto the manipulator of the preparation chamber (10^{-8} mbar) for further treatment such as annealing, sputtering, and material deposition. The manipulator can be heated up to 750°C in the preparation chamber. PES spectra were obtained at room temperature by using a SPECSPhoibos 100 hemispherical analyzer (analysis chamber base pressure 2 x 10^{-10} mbar). XPS measurements were carried out by using the Mg $\mathbf{K}_\alpha$ radiation from a XR-50 dual anode source and ARPES was performed by using a monochromated Helium discharge lamp combining a HIS-13 lamp mounted on a VUV5046 UV-monochromator. The overall energy resolution in XPS amounted to ca. 0.5 eV [199]. In ARPES, the overall energy resolution amounted to 117 meV (65 meV instrumental energy resolutions) at room temperature as determined from the Fermi edge of a polycrystalline gold sample. In the ARPES measurements, the angular resolution was about ± 2 degrees and the energy distribution curves (EDCs) were measured every two degrees. SECO spectra were measured with a sample bias of -10 V. The work function of

the analyzer was calibrated by a clean polycrystalline gold sample before sample measurement. Pass energy was at set 2-10 eV for ARPES and 20-50 eV for XPS.

5 Results and discussion

The results of this thesis will be presented and discussed in this chapter. This chapter starts with the characterization of homemade ML-WS_2 and ML-MoS_2 provided by our cooperator in section 5.1. The results indicate that the measured ML-TMDCs exhibit high quality and homogeneity. Part of these results were published in [200].

In section 5.2, increasing density of SVs together with an increasing band structure renormalization is observed in ML-MoS_2 and ML-WS_2 on sapphire by ARPES. In contrast, annealing-induced band structure renormalization is not observed for ML-TMDCs on HOPG. The impact of SVs on the electronic properties of MoS_2 and WS_2 monolayers will be discussed. Part of these results were published in [201].

In section 5.3, energy level alignments of C_{60}/ML-WS_2 on two different supporting substrates are investigated, including sapphire as an insulting substrate and HOPG as the conductive substrate. No indication of ground-state charge transfer is observed at C_{60}/ML-WS_2 on both substrates, demonstrating vacuum level prevails on both substrates. In addition, we ignored the effect of SVs-induced band renormalization and proposed the interfacial energy diagram of C_{60}/"perfect" ML-WS_2 on both substrates. Part of these results were published in [200].

The optoelectronic properties of F_6TCNNQ adsorbed on ML-WS_2 supported on the sapphire substrate are investigated using ARPES and UV-Vis absorption in section 5.3. Anionic features and an optical transition from F_6TCNNQ/defective ML-WS_2 heterostructure are observed by UV-Vis absorption spectroscopy, while none of these are observed from F_6TCNNQ/ pristine ML-WS_2 heterostructure. The electronic/optical interfacial transition and its functional mechanisms are further discussed by ultraviolet photoelectron spectroscopy (ARUPS).

5.1 Characterization of ML-TMDCs

People devoted extensive effort to synthesizing high-quality continuous ML-TMDC films for their potential application in optoelectronic devices [157, 158, 202, 203]. The focus of this thesis is on the electronic structure study of ML-TMDCs and optoelectronic properties at MSC/ML-TMDC interfaces, thus it is crucial to ensure our measured samples with high

quality and homogeneity. The surface morphology and optical properties of the produced sample are presented in this section.

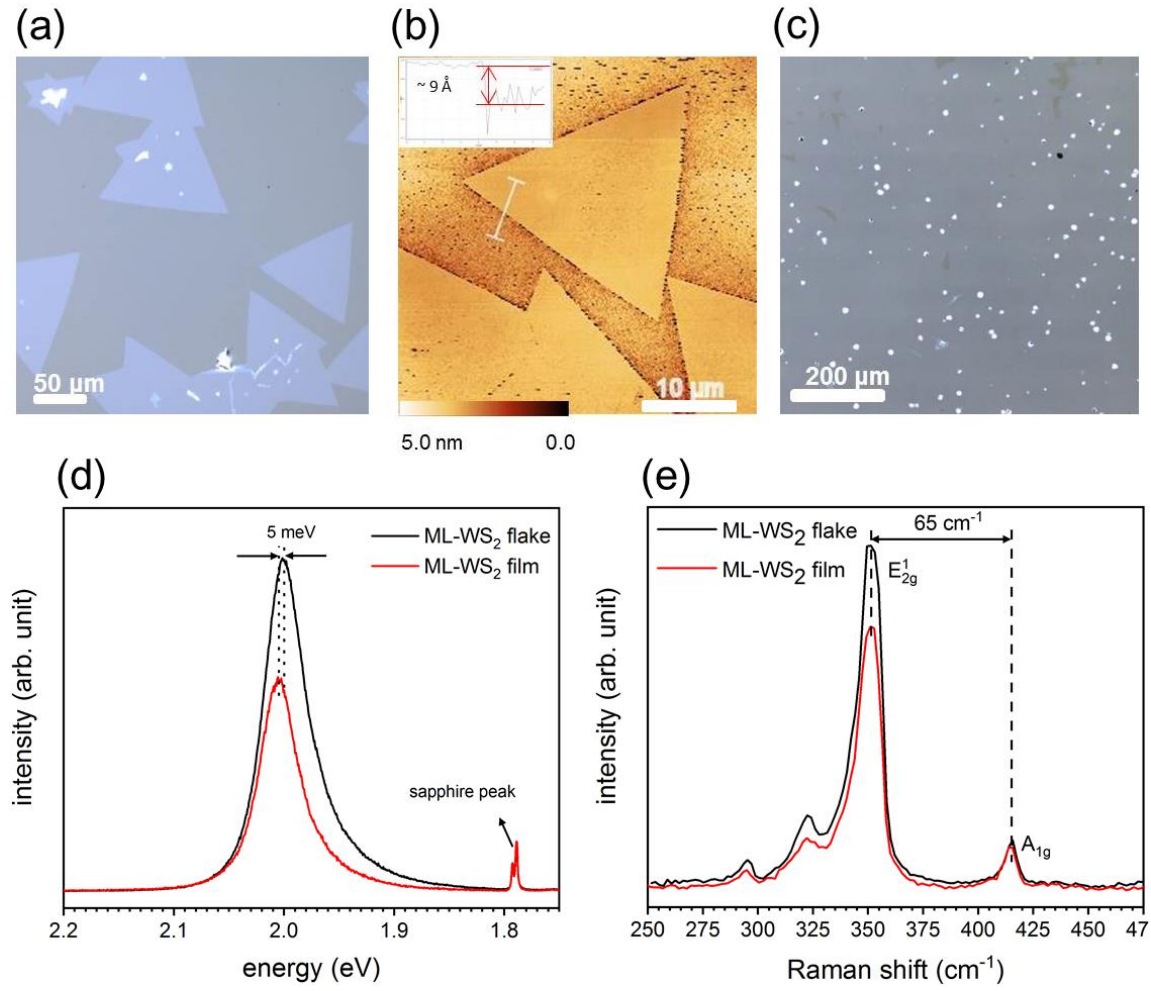

Figure 5.1 *Characterization of monolayer WS_2 flakes and film synthesized on the sapphire substrate. (a) Microscopic images of ML-WS_2 flakes and corresponding (b) AFM surface morphology on sapphire. (c) Microscopic images of ML-WS_2 films on sapphire (d) PL and (e) Raman spectra for WS_2 film and flakes on sapphire. PL intensity is normalized by the sapphire peak for better clarity.*

The surface morphology of the WS_2 flakes is presented in **Figure 5.1** (a) and (b). WS_2 flakes, with well-defined triangle shape, were synthesized via a two-step growth route by CVD. The individual crystallites exhibit large size up to 50 µm. As the AFM image shown in **Figure 5.1** (b), the triangle WS_2 flakes feature high homogeneity with an apparent height of ca. 9 Å, indicating them as monolayers. Using this ML-WS_2 flakes sample as the reference, our CVD-grown WS_2 films, with high substrate coverage of more than 90%, exhibit almost the same typical excitation transition of ML-WS_2 at ca. 2.0 eV [115, 204]. The declined PL intensity of WS_2 film compared with that of WS_2 flakes may result from

defects and residues of MO_x (as mentioned in 3.4) during the CVD process. In addition, both WS_2 flakes and films show the same peak positions of E^1_{2g} (ca. 351 cm^{-1}) and A_{1g} (ca. 415 cm^{-1}), as observed in **Figure 5.1** (e). The Raman shift distance of 65 cm^{-1} between E^1_{2g} and A_{1g} peaks, which is similar to that reported in the literature [115, 117], strongly suggests that both samples are monolayers. Few bright spots on sapphire correspond to the WS_2 multilayers present at growth nucleation sites, comprising less than 2% of the surface area in the ML-WS_2 film [200].

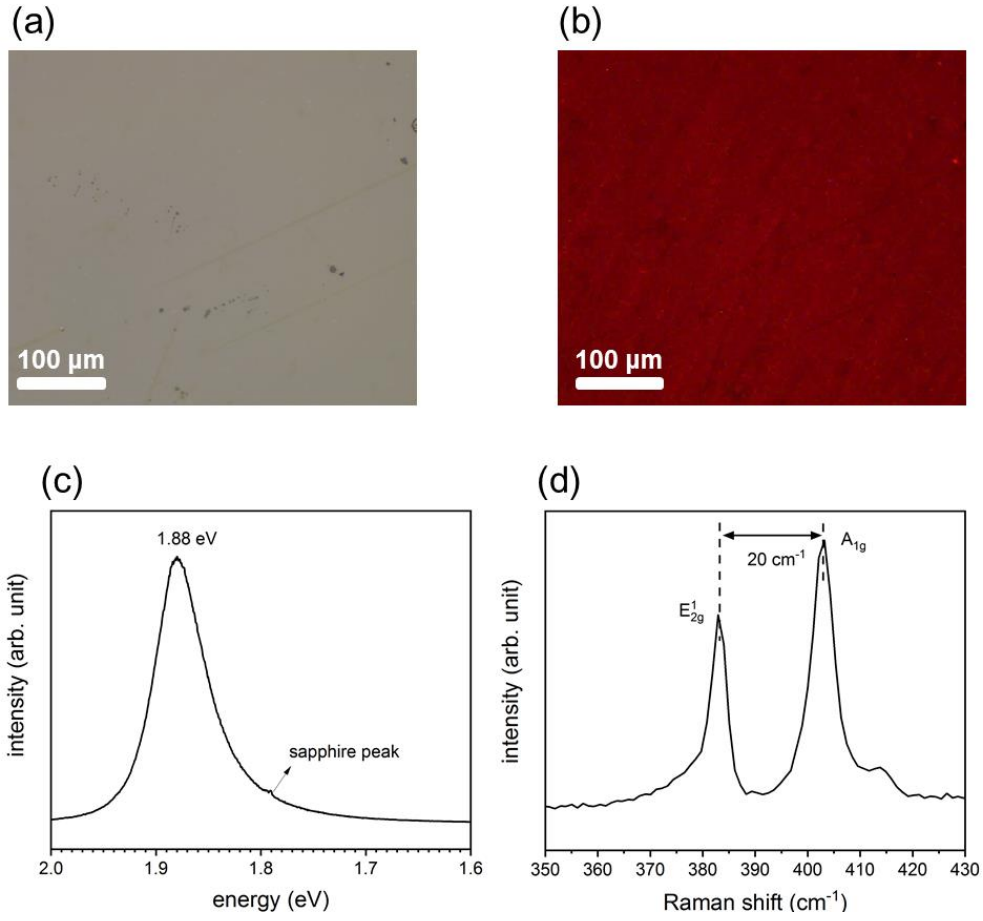

Figure 5.2 *(a) Optical image and (b) corresponding PL image of the typical large scale ML-MoS_2 film. (c) PL and (d) Raman spectra of the ML-WS_2 film and flakes on sapphire.*

Similarly, as revealed by the optical micrograph and corresponding PL image shown in **Figure 5.2** (a) and (b), the CVD-synthetized MoS_2 consists of continuous monolayer films. The typical excitation transition at ca. 1.9 eV with high intensity and the Raman shift distance of ca. 20 cm^{-1} between E^1_{2g} and A_{1g} peaks, observed from PL and Raman spectra of the MoS_2 films, are also deemed as decisive evidence to suggest they are monolayers [114, 205].

The characteristic results demonstrate all the measured WS_2 (MoS_2) films mainly consist of monolayers with high quality and homogeneity, which is the prerequisite for reliable assessment of the optoelectronic properties of ML-TMDCs and their interfaces in this thesis.

5.2 SVs-induced band structure renormalization of ML-MoS_2 and WS_2

Owing to the possibility of wafer-scale fabrication of ML-TMDCs with outstanding optoelectronic properties [1, 206, 207] by chemical vapor deposition (CVD), the interest in these materials has grown immensely over the last few years [1, 2]. Normally, these materials exhibit a range of structural defects [46, 208-211] including vacancies, interstitials, adatoms, grain boundaries, dislocation, and ripple, which can strongly impact the optoelectronic properties of TMDCs [46, 47]. However, investigations regarding the impact of defect states on the electronic structure of the 2D semiconductor are limited.

In terms of S-based TMDCs (MoS_2 and WS_2 in this thesis), SV is deemed as the most abundant defect in mechanically exfoliated and CVD-grown samples due to their low formation energy [44, 45]. The density of SVs from CVD-grown samples is in the range of 10^{12}-10^{13} cm^{-2} [66, 209, 212] and can be increased by vacuum annealing [66, 209, 213]. In this concentration range, SVs can induce n-type localized states within the bandgap, and low density electron transport is suggested to be dominated by hopping via these localized states [214]. Further, it was reported that ML-TMDCs with the higher density of SVs ($>10^{13}$ cm^{-2}) exhibit more n-type behavior as well as higher field effect mobility and larger on-off ratios in transistors [124, 215].

Consequently, due to the evident relevance of SVs, numerous studies have focused on understanding the electronic properties of defective ML-MoS_2. SVs, considered as donors, are predicted to induce deep gap states 0.3-0.5 eV below the CBM [45, 212]. The presence of unoccupied gap states, a few hundred meV lower than the conduction band, has been revealed by scanning and electron tunneling spectroscopy (STS, ETS) [209, 216], which is in line with theoretical results [45, 216]. In contrast to SV acting as the n-type dopant, another photoelectron spectroscopy (PES) study suggested that regions of low sulfur content of ML-WS_2 are actually *p*-type compared to more stoichiometric regions [217]. It should be noted that experimental results via STS/ETS or PES were based on conductive substrates (such as graphene, graphite, and metals). These conductive substrates are

considered as an additional reservoir of charge carriers that could result in charge redistribution at electronic equilibrium. Therefore, to access the intrinsic properties of SVs-induced defective samples, it is necessary to study the electronic properties of TMDCs supported by insulating substrates. In principle, sample charging in PES should prevent such kind of investigation, and this issue can be overcome by continuous large-area ML-TMDC films with sufficient connectivity [218, 219].

In this section, we employ angle-resolved PES (ARPES) to elucidate the effect of SVs on the intrinsic valence electronic properties of MoS_2 and WS_2 continuous monolayer films grown by CVD on the sapphire substrate. Due to the low density of defects and/or their passivation by substitutional oxygen (O_S) [220, 221], and the low density of intrinsic charge carriers [222] in the pristine ML-TMDCs, the samples initially exhibited pronounced charging, which precluded acquiring meaningful ARPES data. In-situ vacuum annealing of the ML-TMDCs results in the production of a large number of SVs and thus provides sufficient conductivity for ARPES measurements. For both MoS_2 and WS_2 monolayer samples on sapphire, we observe via the ARPES the progressive filling of the conduction band, indicating the occurrence of SVs-induced band structure renormalization, which is demonstrated previously only by alkali-metal deposition or electrostatic gating [223-225]. However, SVs-induced band structure renormalization is not observed for ML-WS_2 on HOPG. These notable findings are further corroborated by different conduction band filling behavior of pre-annealed ML-WS_2 on sapphire and HOPG upon doping with electron-donating molecules. Finally, we demonstrate that exposure of a SV-rich ML-MoS_2 to O_2 at elevated temperature (700 K) results in de-doping (i.e., more p-type) and further passivation/healing of the SVs.

5.2.1 Emergency of SVs by annealing

The emergence of SVs is demonstrated by the STEM measurements presented in **Figure 5.3**, showing the effect of a 60 hours annealing step at 950 K on the defect production for ML-MoS_2/sapphire. The STEM measurements were performed by Benedikt. Haas. To assess the density of SVs, multiple high-resolution STEM images including thousands of atoms are acquired and a homemade algorithm is developed and used to find defects and quantify their density (cf. Methods section). Two exemplary STEM images from before and after annealing of the ML-MoS_2/sapphire are depicted in **Figure 5.3** (a) and (c), respectively, and the output of the algorithm marking SVs with a circle in **Figure 5.3** (b) and (d), respectively. The density of SVs in the basal plane of the ML-MoS_2 increased

from about 1% (10^{13} cm^{-2}) in the as-grown ML-MoS_2 film to about 14% (1.5×10^{14} cm^{-2}) after the annealing procedure, indicating the density of SVs can be increased via annealing process in UHV chamber. In addition, the formation of isolated, di-vacancies, tri-vacancies and even vacancies clusters are observed.

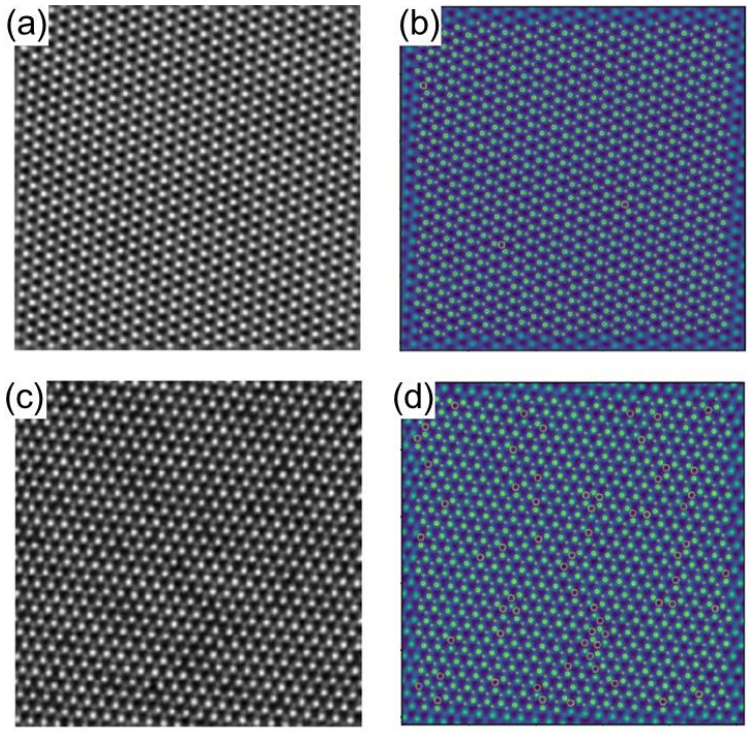

Figure 5.3 *(a, c) STEM images before and after annealing at 950 K for 60 hours. (b, d) analysis of the sulfur vacancies presented in (a, c) with the circles depicting detected SVs (cf. Methods section).*

To investigate the effect of annealing on the chemical properties of the ML-MoS_2/sapphire, XPS spectra of the S 2s-Mo 3d and S 2p core level regions on the ML-MoS_2 sample before and after annealing (same as 3rd annealing in section 5.2.2) are shown in **Figure 5.4** (a) and (b). It is noted that the sample "before annealing" has undergone a mild annealing process (650 K, 2 hours) in order to remove the surface contamination. The Mo 3d doublet peaks at binding energy (BE) of 230.2 eV and 233.3 eV (blue curve) correspond to Mo^{4+} oxidation state from MoS_2. A second doublet features with the Mo $3d_{3/2}$ component at 236.3 eV and the Mo $3d_{5/2}$ at 233.2 eV (green curve) correspond to Mo^{6+} from MoO_3 residues. The S 2s component from MoS_2 is found at 227.5 eV (yellow). As commonly observed [215], the oxide presented in the produced sample is related to unsulfurized MoO_3 during the CVD synthesis. High-temperature annealing leads to the clear broadening of the Mo 3d from MoS_2 suggesting the formation of defects upon annealing. However, due to the multiple contributions (including satellite lines) and the moderate energy resolution, a fitting

procedure of the S 2s-Mo 3d region is quite involved for a reliable determination of the change in sulfur content in the sample or to reveal the presence of defects. Herein, XPS spectra of S 2p are used to track the emergence of defects. The fitted purple curve, revealed in **Figure 5.4 (b)**, demonstrates the occurrence of defects after annealing. The energy difference of S 2p between the defect and main components (black) is about 400 meV, which is in good agreement with the previous studies [215, 217]. The contribution from the defect represents 9% of the total spectral weight, which is consistent with the charge carrier density estimated from the dispersion of the CBM (ca. 5×10^{13} cm^{-2}) for the 3rd annealing step as discussed in section 5.2.2.

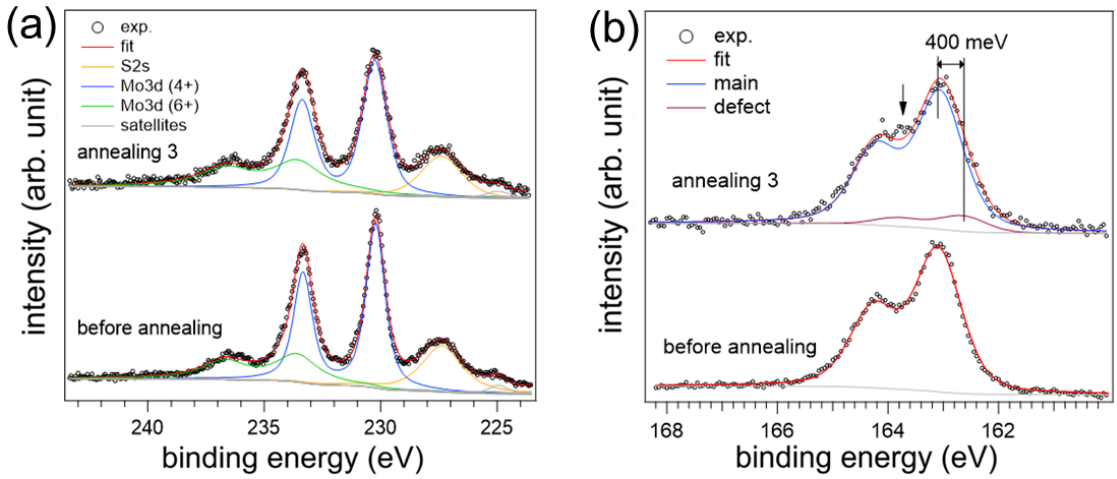

Figure 5.4 *(a) Mo 3d-S 2s XPS spectra of the ML-MoS_2 continuous film gently annealed for two hours at 650 K to remove surface contamination (bottom, here referred to before annealing) and for the 3rd annealing (900 K, 36 hours) (top). (b) S 2p XPS spectra for the mild annealing (bottom) and for the 3rd annealing (top). The fitting procedure includes two S 2p doublets due to stoichiometric MoS_2 (blue) and sulfur in the vicinity of the SVs-induced defect states (purple). The black arrow indicates the increased intensity between the two spin-orbit components of the stoichiometric MoS_2, which results from the presence of the defect component. The Mo 3d-S 2s and S 2p spectra before annealing include a shift of 2.75 eV to lower binding energy to correct for sample charging.*

5.2.2 Electronic structures of annealed ML-MoS_2/sapphire

The ARPES measurements were performed for ML-MoS_2 with a stepwise annealing process of the sample. ARPES spectra of the 1st, 2nd, and 3rd annealing are obtained after in-suit vacuum annealing at 900 K for 12, 24, and 36 hours, respectively. As shown in **Figure 5.5** (a) of 1st annealing (A1), the energy distribution curves (EDCs) measured at different take-off angles demonstrate the expected energy versus momentum $E(\boldsymbol{k})$

dispersion for ML-TMDC films consisting of azimuthally randomly orientated flakes, that is, due to angular averaging the photoemission spectra consist of a superposition of the k-DOS along the Γ-K and Γ-M directions [226]. One local VBM is observed at the Γ-point ($E_b = 2.16$ eV) and the global VBM at the K-point ($E_b = 2.11$eV) of the BZ (see **Figure 5.6**). The VBM located at the K-point instead of the Γ-point indicates measured MoS_2 sample consist of a monolayer on a macroscopic scale [227]. When paying attention close to the E_F region, a faint dispersive signal is observed at the K-point, while the spectra at other momentums are essentially featureless in this energy range. The signal arising at the K-point suggests that the annealing process results in n-type defect states and the electrons in these states will be further ionized to the conduction band minimum (CBM) at the K-point. These defects are attributed to SVs with low formation energy as pointed out previously [66, 209, 213, 217], either resulting from S or oxygen at sulfur site (O_S) desorption [66, 217, 228].

The observation of CBM filling may appear at odds with the common assumption that SVs result in the formation of localized occupied gap states at ca. 0.3-0.5 eV below the CBM [45, 212, 229]. This apparent discrepancy can be resolved by a combination of factors facilitating the ionization of these defects. These are i) occupation of the bands according to Fermi-Dirac statistics at room temperature; ii) bandgap renormalization i.e., narrowing due to dielectric screening by the substrate [48, 219, 230]; iii) strain-induced bandgap renormalization [211]; iv) carrier-induced screening that can account for bandgap narrowing by 0.2-0.5 eV when the doping level lies within the 10^{13} cm^{-2} range [68, 224, 231, 232]. The combined effect of i)-iv) is schematically shown in **Figure 5.7**. If a small fraction of defects become ionized at room temperature initially, the increased screening by carriers reduces the bandgap, thus, more carriers will ionize in turn. This self-amplified mechanism would eventually result in the ionization of all defects. As a result, an electronic bandgap of ca. 2.1 eV was observed at the K-point, i.e., much narrower than the 2.5-2.7 eV predicted by *GW* calculations and determined from ETS and STS measurements on graphene-supported MoS_2 [209, 216, 233, 234], but in very good agreement with the 2.03-2.1 eV bandgap determined from time-resolved ARPES measurements [235].

ARPES spectra of the 2nd annealing (A2) are presented in **Figure 5.5** (d) and (e). The valence region strongly resembles that measured after the first annealing step. Notably, compared with ARPES spectra of 1st annealing, the E_F region displays stronger intensity from dispersing states near the K-point associated with the occurrence of new dispersive signals near ca. 0.65-0.7 $Å^{-1}$. The increased intensity at (and near) the K-point

demonstrates a progressive filling of the conduction band and the smaller electron pocket near ca. 0.65-0.7 $Å^{-1}$ can be readily attributed to the filling of the local CBM at the Q-point (in the middle of the Γ-K path).

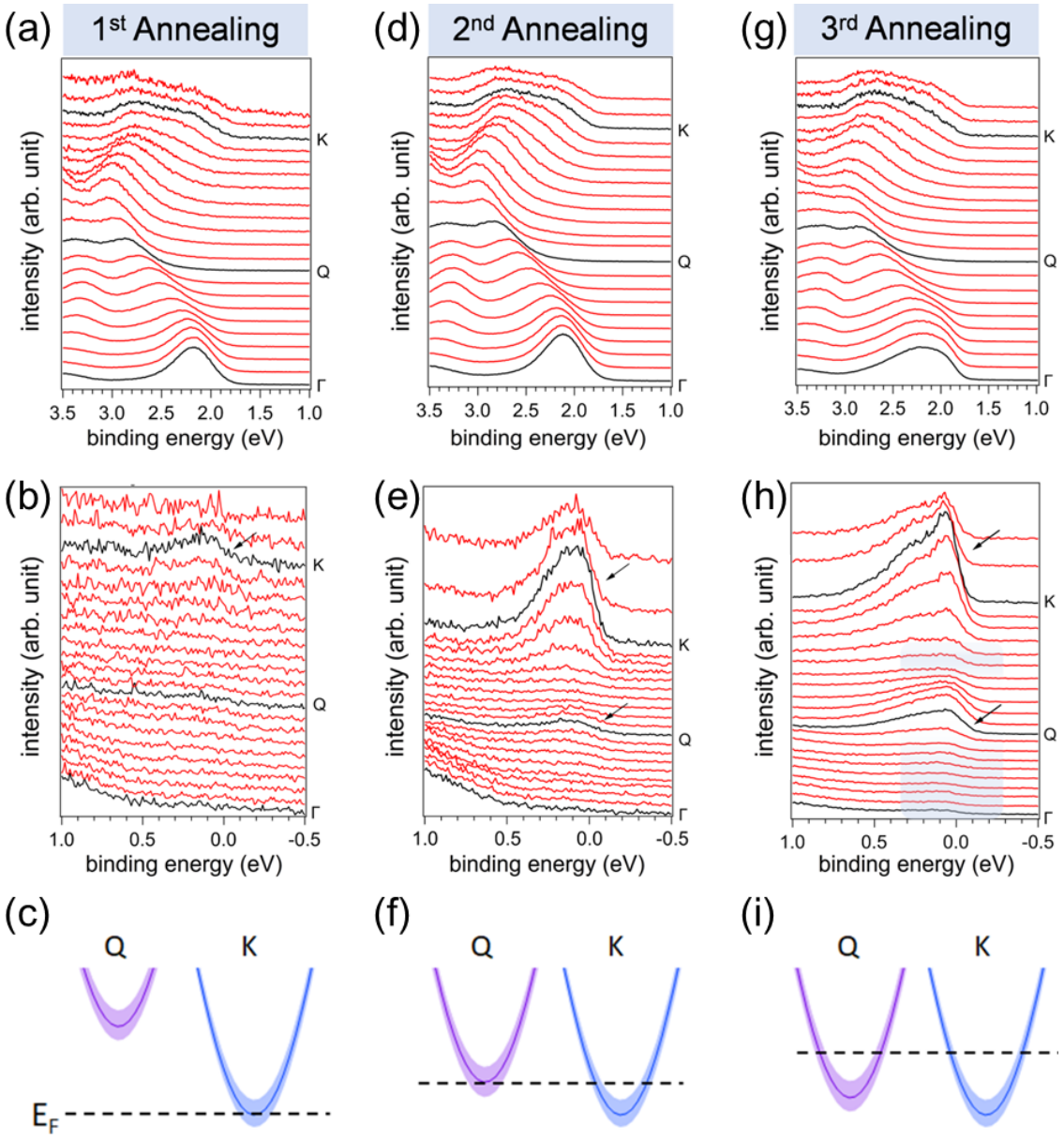

Figure 5.5 *ARPES spectra of ML-MoS_2/sapphire after in-situ vacuum annealing and corresponding band structure renormalization. The spectra at the 1st annealing step as described in the text are shown in the first column. The second and third columns show the ARPES spectra taken at the 2nd and 3rd annealing step, respectively. (a), (d), and (g) show the ARPES spectra of the valence band energy region. (b), (e), and (h), depict the narrow energy range in the vicinity of E_F. The EDCs were measured every two degrees. (c), (f) and (i) illustrate the position of the CBM at the Q-point (purple) and K-point (blue) with respect to E_F as deduced from the measurements. In the ARPES spectra, the black arrows show the electronic states due to conduction band filling at K- and Q-points of the BZ.*

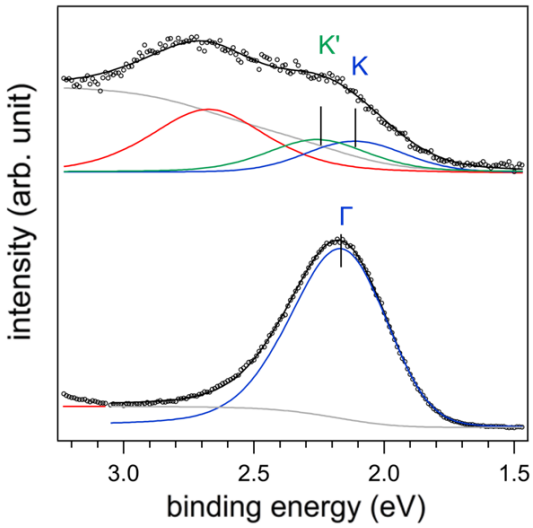

Figure 5.6 *Fit of the EDC at the Γ- (bottom) and K-point (top) for ML-MoS_2/sapphire of 1st annealing. Black circles and black lines show the recorded EDC and the fit results, respectively. For the EDC measured around K-point (top), the blue and green curves represent the contribution from the band at K and K′, respectively. The red curve approximates the contribution from the band in the Γ-M directions.*

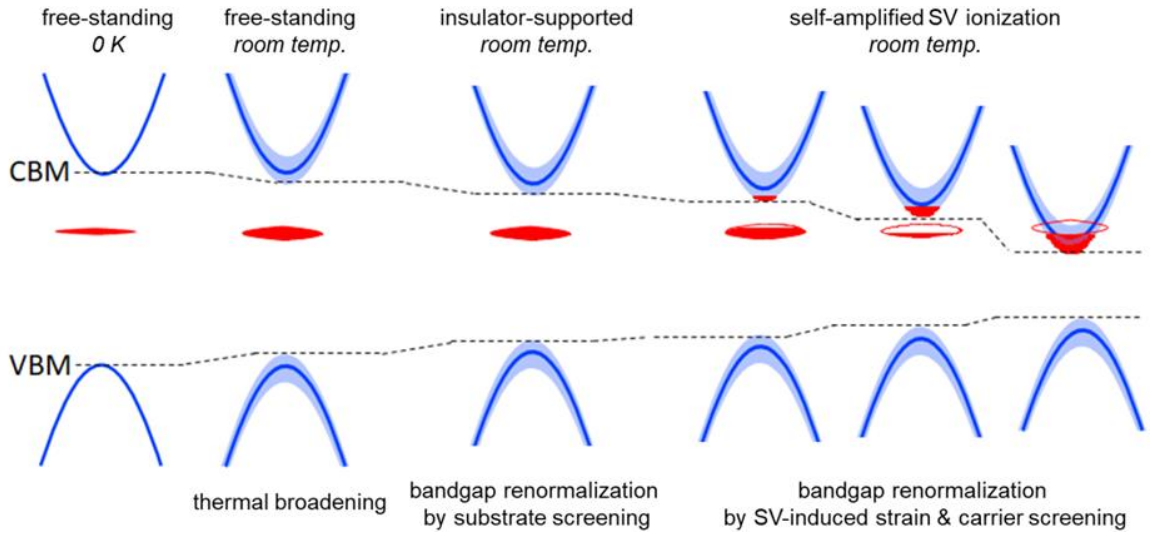

Figure 5.7 *Self-amplified SVs ionization mechanisms. Schematic energy level diagram of the valence and conduction bands (blue), as well as the SVs-induced defect states (red). The interplay of thermal broadening, screening by the substrate, bandgap renormalization by strain, and additional screening by the fraction of ionized electrons from SVs-induced defect states leads to essentially full ionization of these states, and occupation of the conduction band (also red).*

ARPES spectra of the 3rd annealing (A3) are shown in **Figure 5.5** (g) and (h). As presented in **Figure 5.5** (g), the valence features appear broadened compared to the two previous annealing steps, which could be attributed to increased structural inhomogeneity in the

monolayer due to annealing and is consistent with an increased density of SVs [217]. The E_F region around K-point is more structured with essentially one sharp quasi-particle peak close to E_F, followed by a broad feature peak with a binding energy of about 300 meV. As presented in **Figure 5.8** (a) and (b), the quasi-particle peak near E_F exhibits clear dispersion corresponding to an electron effective mass, $m_e^* \approx 0.85 \pm 0.1 m_0$ (m_0 refers to the electron mass at rest). This is comparable well with two recent studies, which approximated the electron effective mass of a MoS_2 monolayer larger than 0.5 m_0 by DFT [201, 235]. In addition, the binding energy of the peak at the K-point amounts to ca. 70 meV. According to related studies [201, 225], we can estimate the carrier density of ca. 5×10^{13} cm^{-2}, which is in good agreement with the TEM results adjusted with respect to annealing time and slightly lower temperature. This value is well beyond the onset of metallic regime, as the Mott metal-insulator transition occurs at carrier concentrations of ca. 10^{13} cm^{-2} owing to electron correlation [126].

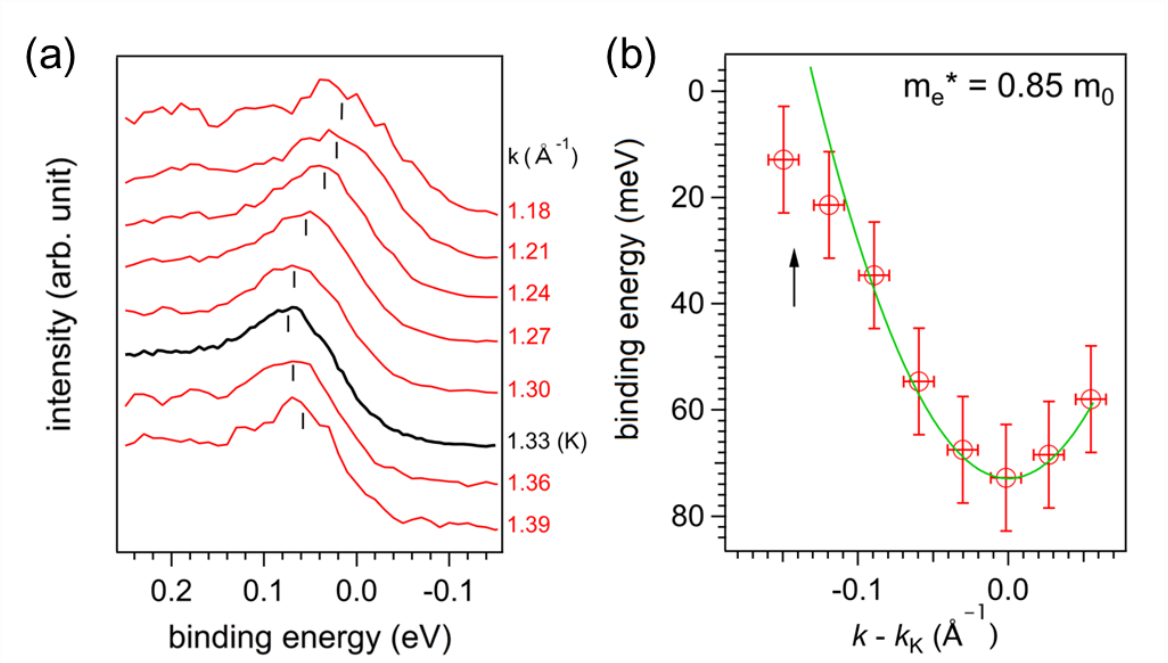

Figure 5.8 *Dispersion of the quasi-particle peak and electron effective mass at the 3rd annealing step. (a) ARPES spectra of CBM around K-point for ML-MoS_2/sapphire at the 3rd annealing step. The vertical ticks show the dispersion of the peak maximum. (b) Dispersion of the CBM and parabolic fit using an effective mass, $m_e^* = 0.85\ m_0$.*

In order to approximate the increase of carrier concentration from A2 to A3, the photoemission signal over the first Brillouin zone is integrated, as shown in **Figure 5.9** (a), to obtain the (***k*** integrated) DOS spectra. The spectral weight in the energy range

corresponding to the valence band, integrated from 1.5 eV to 4 eV (binding energy), is normalized for both samples. Then, the focus is put on the spectral weight in the near E_F energy region, corresponding to the filled conduction bands for the two annealing conditions, as shown in **Figure 5.9** (b). The spectral weight increases by a factor of approximately 3 when comparing A3 to A2.

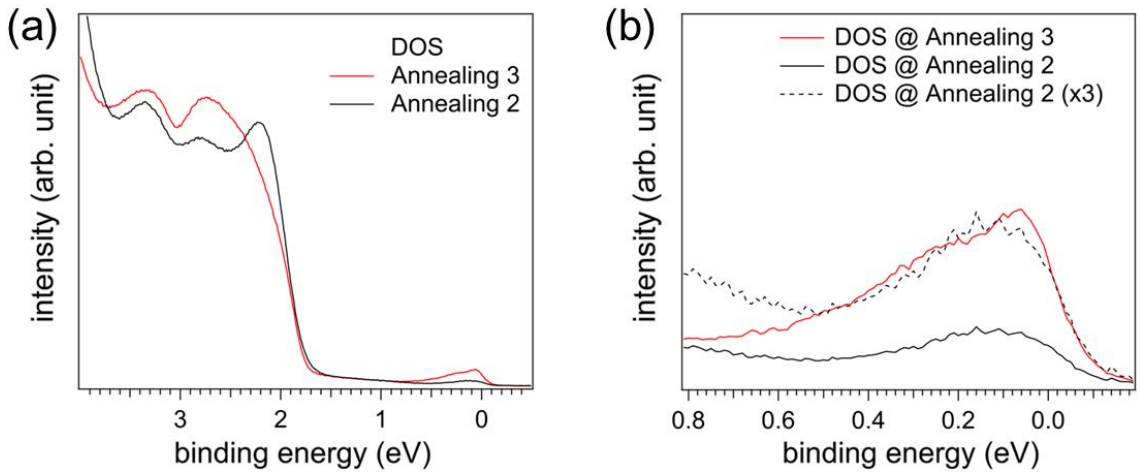

Figure 5.9 *(a) Normalized valence band EDC spectra of the ML-MoS_2 for A2 (black curve) and A3 (red curve). The DOS spectra were obtained by summing the ARPES spectra from Γ-K (corrected for intensity decrease due to change in geometry) and the resulting spectral weight for the energy range from 1 to 4 eV BE was normalized. (b) Zoom in the E_F energy region from (a). The spectral weight for A3 is found to be roughly three-fold that of A2.*

It is noted that, in the near E_F energy region, the spectral weight at Q-point appears to be significantly enhanced with respect to that at K-point after the 3rd annealing. $R_{K/Q}$ refers to the spectral weight ratio, describing the ratio of the total number of electrons in the CB electron pocket at K- and Q-point. After calculating the spectral weight ratio at K- and Q-point from the plots below (**Figure 5.10**), the $R_{K/Q}$ is changed significantly from ca. 5.5±0.5 (A2) to ca. 2.3±0.3 (A3). This change cannot be explained by the shift of E_F alone but results from that the local CBM at Q-point moves closer to the global CBM at K-point, as depicted in **Figure 5.5** (c), (f), and (i). This decrease of the spectral weight ratio can be likely due to either SVs-induced compressive strain within the layer [51], or increased electron density by self-doping [52], or a result of both. The speculation is further verified by the simulation results (section 5.2.3) and the results of ML-WS_2/sapphire (section 5.2.4).

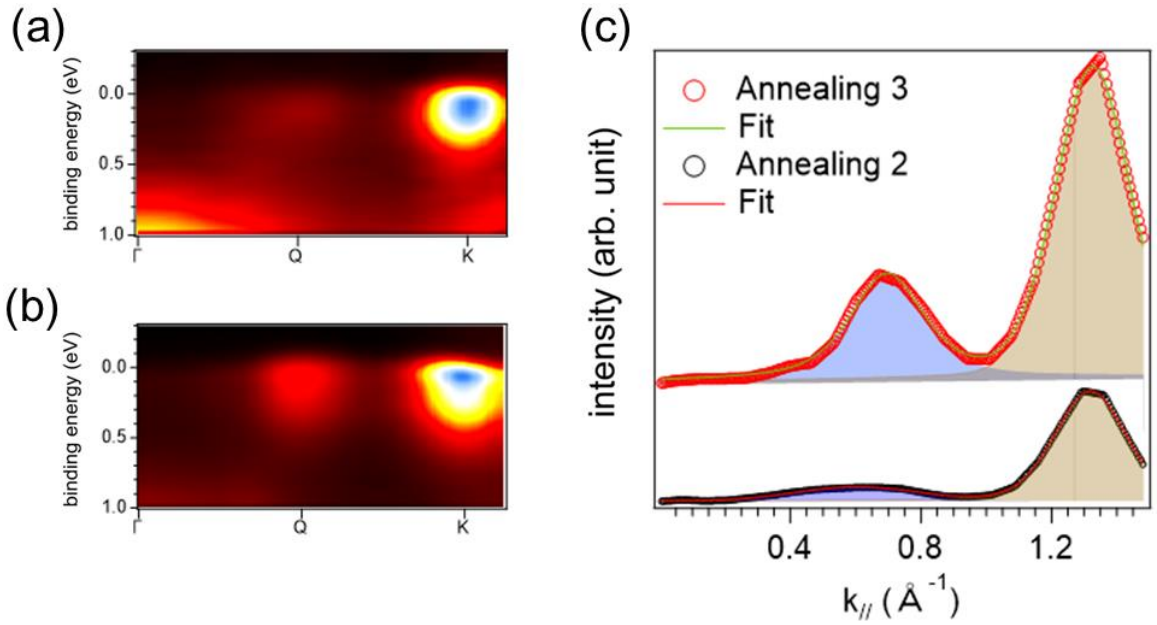

Figure 5.10 *(a, b) ARPES plot representation of the spectra based on the data from* ***Figure 5.5*** *(e) and* ***Figure 5.5*** *(h). These plots are obtained after image interpolation and smoothing treatment for annealing 2 and annealing 3. (c) Corresponding Momentum Distribution Curves (MDC) integrated with the 0.2-0.5 eV energy window.*

5.2.3 Simulations of the spectral function based on DFT calculations

Band structures of pristine ML-MoS_2 and ML-MoS_2 with compressive strain are obtained by density-functional theory (DFT) calculations. It is noted that the DFT calculations in this section were performed by Fabio Caruso and Areej Aljarb. These calculations are conducted based on the plane-wave pseudo-potential method as implemented in Quantum Espresso [236], with the Brillouin zone sampled on a 20x20x1 Monkhorst-Pack grid. The exchange-correlation functions are obtained by using a 120 Ry kinetic energy cutoff, fully-relativistic norm-conserving pseudo-potentials, and the Perdew-Burke-Ernzerhof (PBE) parametrization of the generalized-gradient approximation [237]. Spin-orbit coupling is explicitly accounted for in our calculations. Biaxial strain was applied through a renormalization of the crystal lattice vectors.

The lowest-energy conduction band spectra of MoS_2 and WS_2 monolayer films for the unstrained geometry and a compressive biaxial strain of 3% are presented in **Figure 5.11** (energies are with respect to the CBM of ML-TMDCs). Spin-orbit coupling breaks the degeneracy of the spin-up and spin-down components at the Q-point. The CBM at Q-point is much closer to the global CBM at K-point for ML-WS_2 (77 meV above CBM at K-point) compared to that of ML-MoS_2 (185 meV above CBM at K-point) in the unstrained case.

The compressive strain significantly lowers the CBM at the Q-point, which is in comparison with the experimental results in section 5.2.2.

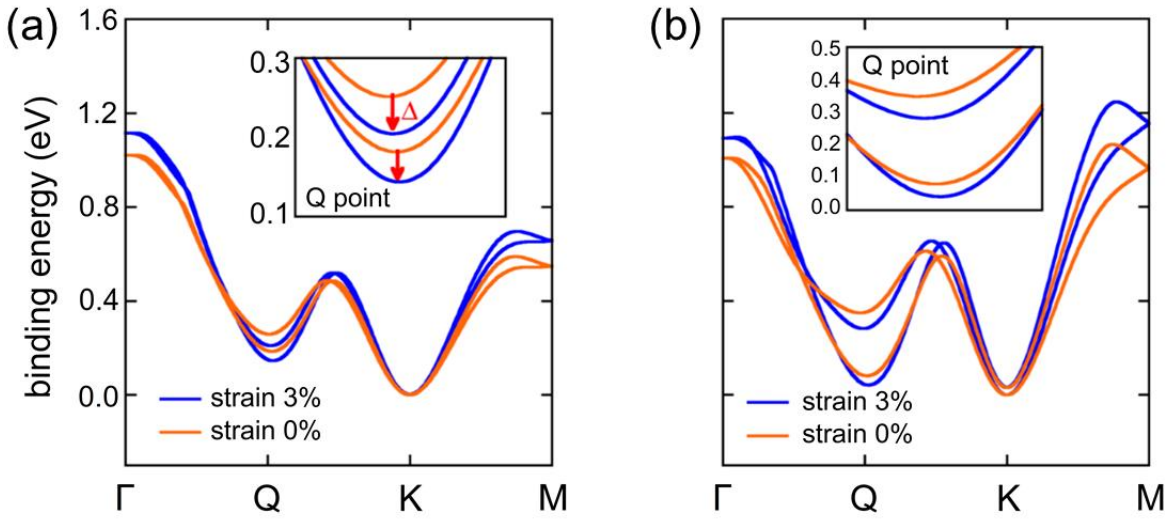

Figure 5.11 *Energy dispersion of the lowest conduction band of ML-MoS_2 (left) and ML-WS_2 (right) as obtained from DFT-PBE for the unstrained (PBE-relaxed) geometry and in presence of a compressive bi-axial strain of 3%. Inset: close-up of the Q-pocket.*

Using the DFT band structure, the relative ratio of electron occupation in the Q and K pockets can be estimated based on Fermi-Dirac statistics. The spectral function is computed by assuming Fermi-Dirac occupations ($f_{n\boldsymbol{k}\sigma}(T) = [e^{(E^{\sigma}_{n\boldsymbol{k}}-E_F)/k_BT} - 1]^{-1}$), where $E^{\sigma}_{n\boldsymbol{k}}$ is the energy of the σ spin-component of conduction band. The resulting spectral functions are illustrated in **Figure 5.12**. E_F refers to the binding energy of Fermi level with respect to CBM. E_F is determined by the binding energy of first sharp quasi-particle peak at K-point, as 8 and 70 meV for A2 and A3, respectively. The obtained spectral functions cannot reproduce the loss features in the 0.2-0.5 eV binding energy region, as many-body effects are neglected in the calculation. Then the calculated $R_{K/Q}$ can be obtained by the ratio integrated spectral intensities in the K- and Q-pockets from DFT spectra.

The calculated $R_{K/Q}$ for a series of Fermi level with respect to CBM and the amount of biaxial strain are presented in **Figure 5.13**. This calculation provides reasonable $R_{K/Q}$ values following the trend indicated by the tentative fitting procedure and strongly suggests that compressive strain can be one of the reasons to explain the observed change in $R_{K/Q}$.

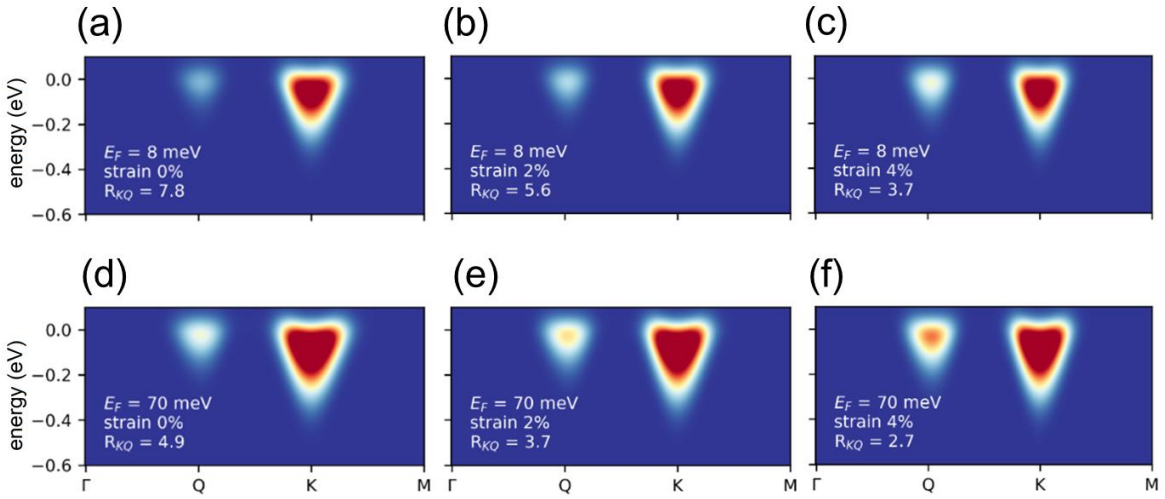

Figure 5.12 *Exemplary Fermi-Dirac occupation of the conduction band at room temperature for unstrained lattice, 2% and 4% compressive biaxial strain with and E_F of 8 (a-c) and 70 meV (d-f). E_F refers to the binding energy of the Fermi level with respect to CBM. The corresponding values of E_F as well as the $R_{K/Q}$ are provided in each graph.*

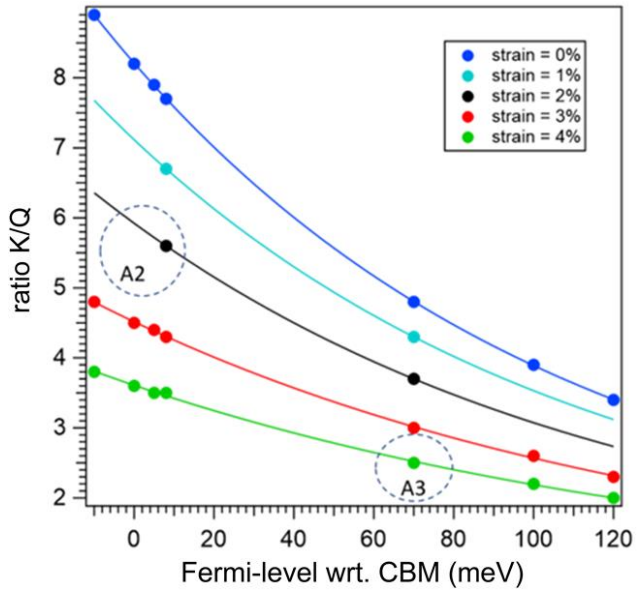

Figure 5.13 *Calculated $R_{K/Q}$ ratio (dots) as a function of the amount of biaxial strain and Fermi level with respect to CBM (dots). Solid lines show a fit of the calculated points to highlight the trend in the $R_{K/Q}$ evolution. The dotted circles are consistent with the calculated result of A2 and A3 in* ***Figure*** *5.12.*

In addition, the band structures of ML-WS_2 upon doping concentrations are obtained from DFT calculations (**Figure 5.14**). The CBM at Q-point approaches the CBM at K-point upon doping, resulting in the decrease of $R_{K/Q}$. Therefore, both compressive strain within the layer or increased electron density by self-doping can induce the decrease of $R_{K/Q}$.

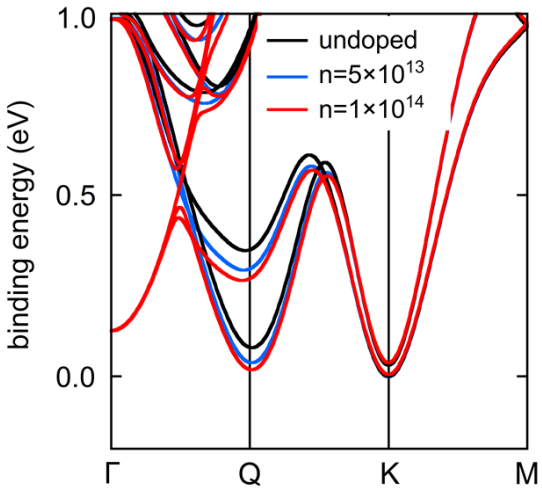

Figure 5.14 *Calculated conduction band structure of undoped ML-WS_2, doped with 5×10^{13} cm^{-2} and 1×10^{14} cm^{-2} electrons.*

5.2.4 Impact of the substrate on WS_2 monolayer doping: sapphire *versus* HOPG

As shown in **Figure 5.15** (a) and (b), ARPES spectra of ML-WS_2/sapphire are obtained after annealing at 900 K for 12 hours. The wide-range spectrum exhibits dispersive electronic states, which, for the same reasons as ML-MoS_2 mentioned above, correspond to a superposition of $E(\boldsymbol{k})$ along the high symmetry directions. The EDCs also reveal the global VBM to be at K-point at ca. 2.0 eV binding energy, indicating the presence of ML-WS_2 films [227]. Furthermore, the presence of dispersive states is observed close to the E_F, in contrast to ML-MoS_2/sapphire, which is more intense at Q-point than that at K-point. Pursuing the reasoning developed above, this observation is attributed to the filling of the CBM at Q-point due to the ionization of electrons from SVs-induced defect states. Although ML-WS_2 is a direct bandgap semiconductor, a notable difference between ML-MoS_2 and ML-WS_2 is that for the latter the CBMs at K- and Q-point are almost degenerate [51, 238]. Our observation of the dominant CBM at Q-point implies a fundamental change of the band structure. This can be consistently assigned to compressive strain and/or to doping, which have been predicted by theory to induce a change from a direct to an indirect bandgap semiconductor [51, 52, 239]. In addition, the bandgap here amounts to ca. 2 eV, which is 0.7 eV narrower than that determined by other electron spectroscopic methods for the corresponding TMDC/graphene samples, for which carrier screening upon CBM filling is not at play due to charge redistribution with the sapphire substrate [209, 216].

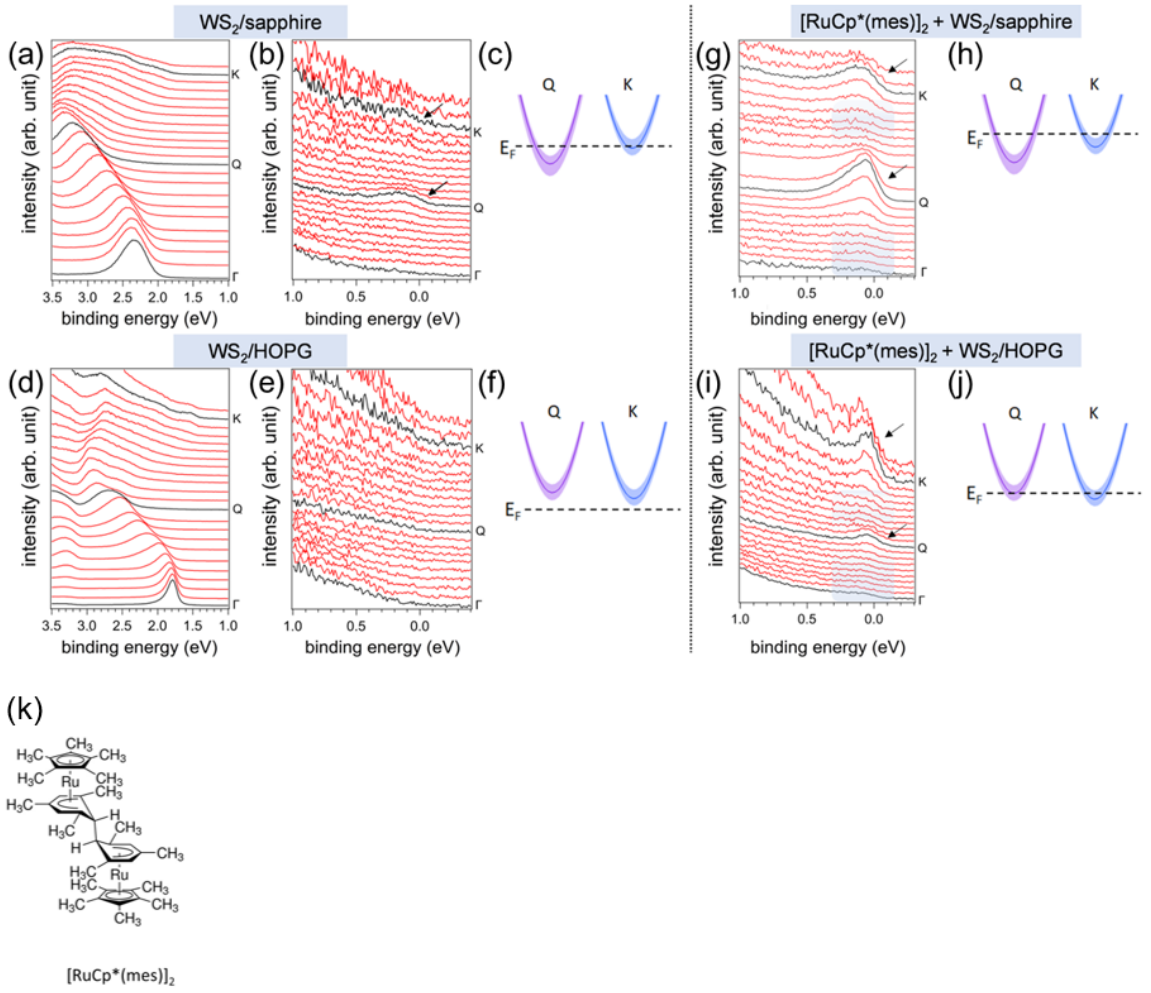

Figure 5.15 *ARPES spectra of ML-WS_2 on sapphire and HOPG and upon molecular n-doping. ARPES spectra of ML-WS_2 on (a, b) sapphire and (d, e) HOPG, together with the respective energy level diagram (c, f) including the CB at Q- and K-point. ARPES spectra of [RuCp*(mes)]$_2$ deposited on ML-WS_2 on (g) sapphire and (i) HOPG together with the respective energy level diagram (h, j) including the CB at Q and K. The EDCs were measured every two degrees. The black arrows show the electronic states due to conduction band filling at Q- and K-point. (k) Molecular structure of [RuCp*(mes)]$_2$*

ARPES spectra of ML-WS_2 transferred onto HOPG are shown in **Figure 5.15** (d) and (e). This sample is subjected to the same annealing process in UHV as ML-WS_2 on sapphire. The VB features are sharper than those observed for both ML-WS_2 and ML-MoS_2 on sapphire. It is noted that the transfer procedure itself does not contribute to the sharper features, since the width of the VB features are mostly conserved upon transfer from a sapphire used as the growth substrate to another sapphire substrate. Therefore, the weak van der Waals interaction and flat potential landscape of the underlying HOPG substrate as compared to the polar c-plane of sapphire is likely the cause for the sharper VB features of

ML-WS_2 on HOPG. The global VBM of ML-WS_2/HOPG at K-point shifts to lower binding energy by 0.5 eV as compared to that of ML-WS_2/sapphire. This can be explained by the energy level alignment at the ML-WS_2/HOPG interface, which deviates only slightly from the Schottky-Mott limit possibly because of weak Fermi level pinning at SVs-induced defect states, as the sample work function with monolayer is about ca. 200 meV lower than that of bare HOPG, as shown in **Figure 5.16** (d). Furthermore, inspection in the near E_F region shows the absence of states associated with CBM filling, which is in contrast to that on the sapphire substrate. This is due to the electrons from SVs-induced defect states transferring to the HOPG substrate instead of to the CBM of ML-WS_2. This scenario is fully consistent with recent ETS/STS studies, in which the signature of SVs-induced defect states appeared as resonances in the unoccupied part of the DOS spectrum, i.e., they are fully ionized [47]. Therefore, the use of a conductive substrate apparently inhibits the observation of SVs-induced defect states in PES.

To examine whether band structure renormalization, observed from ML- WS_2/sapphire, i.e., the shift of the global CBM from K to Q that promotes an indirect bandgap is indeed substrate-dependent and results from strain or doping, it is necessary to change the doping level by means other than SVs, and monitor the location of the global CBM for ML-WS_2 both on sapphire and HOPG. It was reported that the organometallic mesitylene pentamethylcyclopentadienyl ruthenium dimer [RuCp*(mes)]$_2$ could serve as the n-dopant for few-layered WSe_2 and other inorganic bulk semiconductors [240, 241]. Thus, [RuCp*(mes)]$_2$ is employed to dope the vacuum-annealed ML-WS_2. As displayed in **Figure 5.15** (g), upon [RuCp*(mes)]$_2$ deposition onto ML-WS_2/sapphire, a strong photoemission intensity is observed at both CBM around Q- and K-point, demonstrating efficient n-doping by the molecule. This finding demonstrates that molecular doping does not result in only localized carriers in ML-WS_2, as might be expected from the strong Coulombic attraction between the electron in the semiconductor and the positively charged RuCp*(mes)$^+$ cations, but also a significant fraction of electrons transferred to CBM of ML-WS_2. Importantly, the spectral weight at the Q-pocket is much larger than that at the K-pocket, supporting the above conclusion regarding the indirect bandgap observed for n-doped ML-WS_2/sapphire due to SVs alone. The ARPES spectra for [RuCp*(mes)]$_2$/ML-WS_2/HOPG previously anneal to feature SVs, shown in **Figure 5.15** (i), also confirm that electrons transfer to the TMDC by the clear emergence of filled states at Q- and K-point. However, the key difference compared to the sapphire substrate case is that the intensity of the K-pocket is higher than that of the Q-pocket. This indicates that the bandgap is still

direct on HOPG, implying no band structure renormalization occurring on HOPG even with high charge carrier concentration. The results indicate that neither doping nor the presence of SVs alone is sufficient to induce the band structure renormalization (i.e., the change in K/Q pockets photoemission intensity). In addition, as seen from the photoemission intensity stemming from the partially filled CB of ML-WS_2 on different substrates, we remark that a similar sample work function change upon molecular adsorption and doping of ML-WS_2 is less effective when HOPG serves as substrate compared to sapphire (see **Figure 5.16**). Electrons from the dopant molecules are mostly transferred to the HOPG substrate, resulting in a doping mechanism for WS_2 that is largely electrostatic in nature. The electric field between the molecular cations and the electrons in HOPG shifts the ML-WS_2 levels, resulting in CBM of ML-WS_2 being partially filled [218]. This is different from "direct" doping where electrons are transferred from the molecule to the CB of the ML-TMDC supported on an insulator substrate [218]. These results support the proposition discussed above that different charge rearrangement takes place upon conductive and insulating substrates.

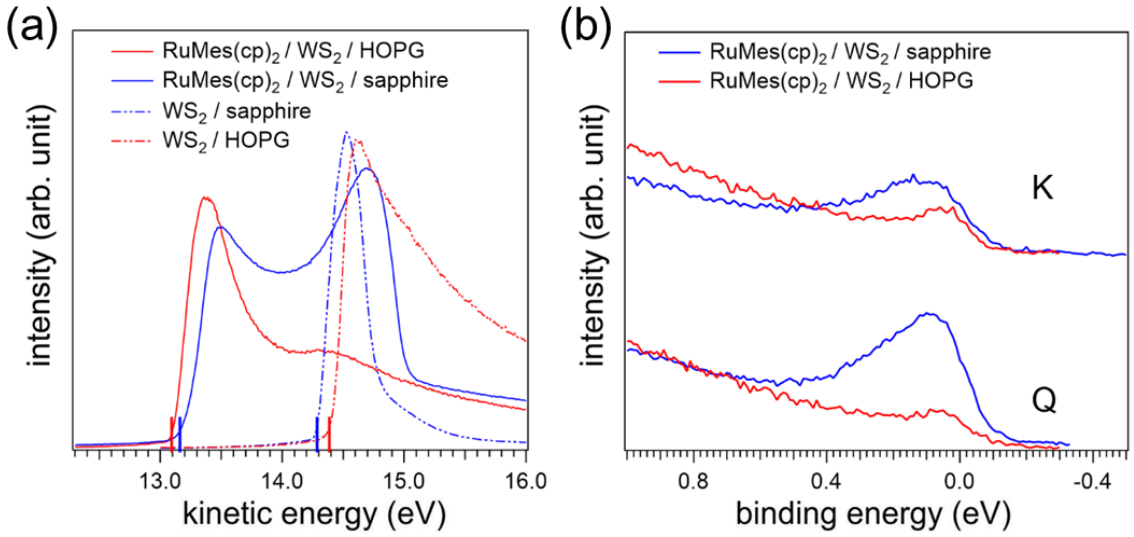

Figure 5.16 *(a) SECO spectra of ML-WS_2/sapphire and ML-WS_2/HOPG (blue and red dotted lines, respectively) and SECO spectra of [RuCp*(mes)]$_2$ on ML-WS_2/sapphire and ML-WS_2/HOPG (blue and red solid lines, respectively). (b) Zoom in the E_F region at the Q- and K-points for [RuCp*(mes)]$_2$ on ML-WS_2/sapphire and ML-WS_2/HOPG. The intensity of the respective valence band EDCs in the higher energy region for both BZ regions were normalized to provide a meaningful comparison of the intensities in the presented spectra.*

5.2.5 Oxygen exposure and healing of sulfur vacancies

Finally, the impact of O_2-exposure on the density of SVs of a defective ML-MoS_2/sapphire sample, which was formerly thermally treated for 7 hours at 1000 K to feature the comparable density of SVs of A3, is investigated. As presented in **Figure 5.5** (e), O_2 with pressure in the range of 10^{-6}-10^{-5} mbar was exposed to the ML-MoS_2 film for typical periods of time going from 1h to 12h, with the sample heating at 700 K in the UHV chamber. The total O_2 dose, to which the sample was exposed during these experiments, amounts to ca. 6.325×10^5 Langmuir (L). Finally, an additional annealing step of 1 hour at 1000 K was performed to assess the reversibility of the observed changes. ARPES measurements at the K-point with an integration angle corresponding to a momentum range of $\pm$ 0.2 $Å^{-1}$ (i.e. encompassing the full signal from the CBM) were carried out after each exposure, resulting in the EDCs corresponding to the energy region of the VB and CB as presented in **Figure 5.17** (a) and (b). Furthermore, **Figure 5.17** (c) shows an overlay of the EDCs corresponding to the CBM region after Shirley background subtraction in order to better appreciate the intensity evolution upon exposure, and the corresponding evolution of the CBM spectral weight is represented in **Figure 5.17** (d). The main findings from these experiments can be summarized as follow: i) A sharp decrease of the spectral weight of about 45% from the CBM is observed for exposures up to about 3.25×10^4 L followed by an additional decrease of ca. 10% when exposed to a further O_2 dose of 6×10^5 L; ii) concomitantly to the attenuation of the CBM, the VBM shifts towards E_F by up to 70 meV, indicating the de-doping of the MoS_2 monolayer and iii) following the last annealing step, DOS recovery of nearly 100% (ca. 97%) is observed from the CBM. The temperature, at which the sample was held during O_2-exposure, is well beyond the expected desorption temperature of physisorbed molecular adsorbates [242-244]. As the electron transfer of about 1 electron is calculated to be transferred to a molecular/atomic oxygen chemically

adsorbed at a SV site, it is here likely that the de-doping effect results from the chemical adsorption of molecular oxygen (or atomic oxygen, if dissociative adsorption eventually takes place) on the SVs [221], facilitated by sufficient thermal energy to overcome an estimated adsorption energy barrier of ca. 1 eV [221, 243]. These results constitute further evidence of the involvement of the ionization of electrons from SVs-induced defect states in the CBM filling of the ML-MoS_2 on sapphire and demonstrate that partial control of the doping level induced by SVs can be achieved via exposure to oxygen molecules at the elevated temperature.

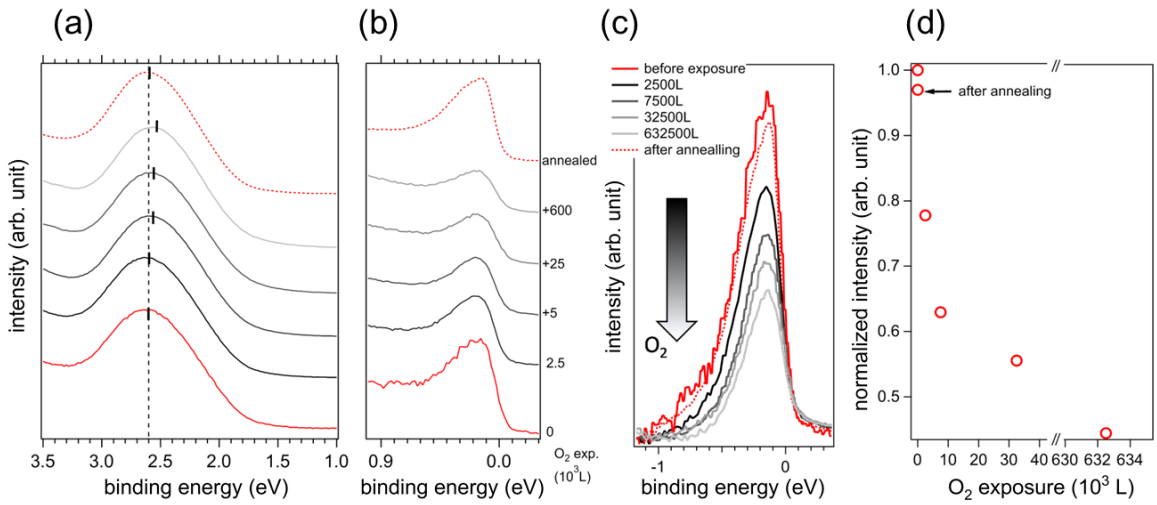

Figure 5.17 *Effect of oxygen exposure on the electronic properties of ML-MoS_2/sapphire. (a, b) EDC of the valence band and E_F energy region at the K-point as a function of O_2 dose (in Langmuir) to which the sample was exposed while kept at 700 K. (c) CBM graph after subtraction of a Shirley background from (b) to better visualize the evolution of the DOS at E_F with O_2 dosage. (d) Evolution of the spectral weight at E_F energy region as a function of oxygen exposure. The red dotted curve corresponds to the sample annealed after the last O_2-exposure.*

5.2.6 Discussion and conclusion

We demonstrated a series of PES measurements that annealing of MoS_2 and WS_2 monolayers supported by an insulating substrate induce a large density of sulfur vacancies, which act as n-dopants. This is unambiguously identified via the observation of dispersive bands around the E_F, which corresponds to the filling of the two minima of the conduction

band at K- and Q-point with carrier concentration in the 10^{13} cm^{-2} range, making the ML-TMDC films conductive enough to be measured by ARPES despite on the insulating substrate. This evidences that the electrons from SVs-induced defect states, which are normally expected to be relatively deep (several 100 meV below the CBM) and thereby limiting transport properties, are here fully ionized to the CBM of the ML-TMDCs. These apparent discrepancies can be reconciled by considering that the bandgap increasingly shrinks with increasing carrier density within the CBM, which acts as a positive feedback loop for the ionization of the electrons from the defect states, thus, the E_F eventually reaching the CBM edge. In contrast, when using a conductive substrate, the electrons from SVs-induced defect states are primarily ionized towards the substrate charge reservoir, as depicted from ML-WS_2/HOPG in **Figure 5.18**. These results can therefore explain the difference in bandgap found here on sapphire (ca. 2.1 eV and 2.0 eV for ML-MoS_2 and WS_2, respectively) and in other studies by STS/ETS on graphene (> 2.5 eV for both MoS_2 and WS_2) [209, 216]. Furthermore, these findings provide a rationale in terms of band structure that help understand the improved transport characteristics of ML-MoS_2 field-effect transistors at high defect concentration, as this yields sufficiently high carrier density to approach or reach the metal-insulator transition [124, 215].

Other than by SVs, $[RuCp^*(mes)]_2$ was employed to obtain strongly n-doped TMDC monolayers both on sapphire and HOPG. The doping mechanisms are markedly different depending on the conducting properties of the substrate, that is, we identified a direct doping mechanism on sapphire, while on HOPG, TMDC doping is electrostatic in nature and results in charge transfer from $[RuCp^*(mes)]_2$ to HOPG.

For both ML-TMDCs on sapphire, we observed strong band structure renormalization as the local CBM at the Q-point of the BZ moves in energy towards the global CBM at the K-point, and for ML-WS_2/sapphire, the Q-point even becomes the new global CBM.

Presented examples on HOPG suggest that the combination of SVs and doping of the ML-TMDC films does not result in such band structure renormalization, which is likely caused by the interaction between the SV-rich, n-doped TMDC monolayer films and the sapphire substrate. Such band structure renormalization is further consistent with compressive strain, which was reported for the MoS_2 and WS_2 monolayers grown on sapphire [239] and with determined contraction of bond length around SVs [245, 246]. In contrast, for ML-WS_2 supported by HOPG, the lack of band structure renormalization implies that stress can be better released on this substrate as compared to sapphire, which is consistent with the lubricant properties of both materials.

Finally, we explored the effect of O_2 chemisorption by exposing the sample to low-pressure O_2 at the high temperature. Our measurements reveal the occurrence of the de-doping process for ML-TMDCs/sapphire, with a decrease by ca. 50% of the carrier concentration in the K-pocket, as molecular or atomic oxygen (following potential dissociative adsorption) binds to SV sites and eliminates the associated defective states, therefore demonstrating a way to potentially heal the post-growth materials.

In summary, the results contribute to a comprehensive understanding of the electronic properties of TMDCs in the presence of high SVs density on vastly different substrates that are widely used in fundamental studies and in device fabrications. In this regard, these findings bring about new insights to comprehensively understand the optoelectronic and electrical properties of the corresponding systems. The observed substrate-dependent impact of the defects in the DOS spectrum will need to be adequately considered for advanced defect engineering in view of TMDC-based applications, such as catalysis, optoelectronics, plasmonics, and nanophotonics.

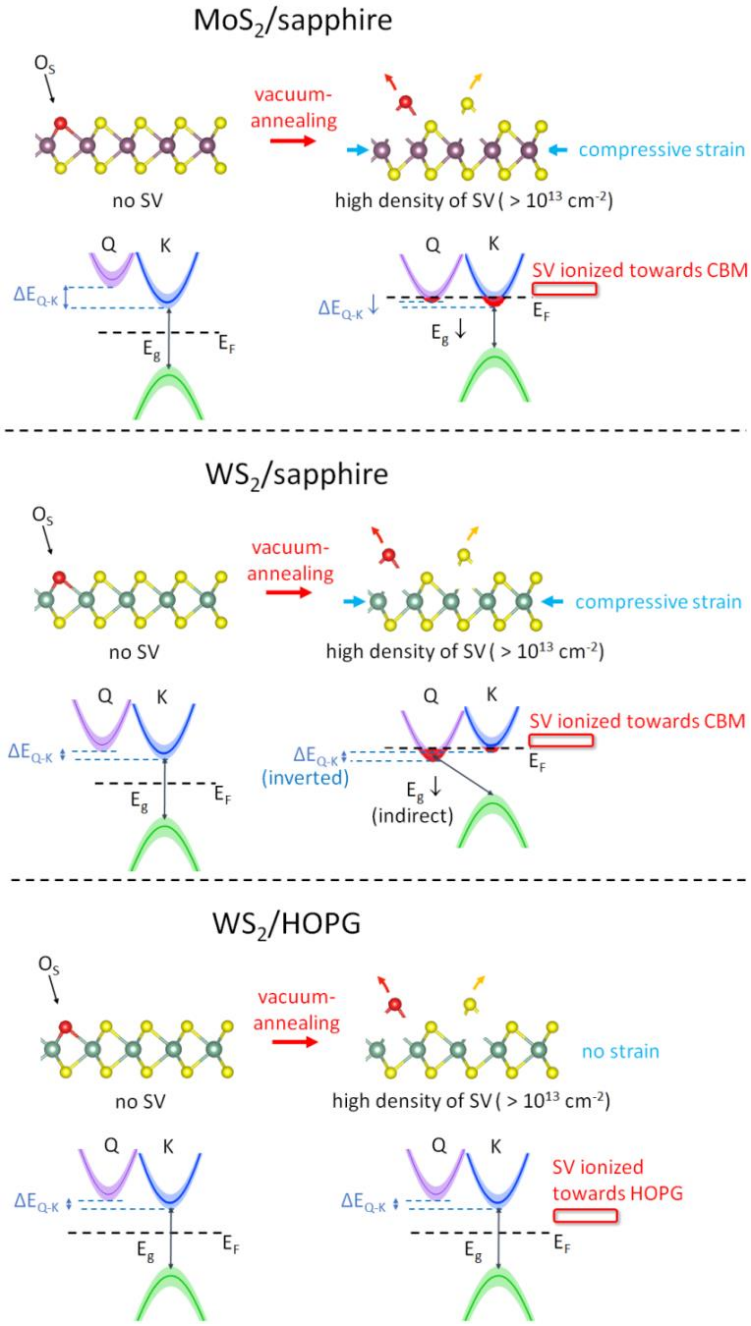

Figure 5.18 *Effect of oxygen exposure on the electronic properties of ML-MoS_2/sapphire. (a,b) EDC of the valence band and E_F region at the K-point as a function of O_2 dose (in Langmuir) to which the sample was exposed while kept at 700 K. (c) CBM graph after subtraction of a Shirley background from (b) to better visualize the evolution of the DOS at E_F with O_2 dosage. (d) Evolution of the spectral weight at E_F as a function of oxygen exposure. The red dotted curve corresponds to the sample annealed after the last O_2-exposure.*

5.3 ELA at the C_{60}/ML-WS_2 interface on insulating and conductive substrates

TMDCs are comparably chemically inert and exhibit no dangling bonds, particularly in monolayer form [29, 30]. This provides the opportunity for the fabrication of van der Waals heterostructures with molecular and organic semiconductors, which could combine the advantages of the two individual material classes, e.g., the high charge carrier mobility of the ML-TMDC and strong light-matter coupling across a wide energy range of the molecular compound [29, 32, 247]. Such MSC/ML-TMDC heterostructures can feature advanced optoelectronic properties [34, 218], which naturally depend strongly on the electronic structures of the corresponding interfaces. It is, therefore, crucially important to understand how the energy levels at such interfaces align, and how they can eventually be controlled.

The electronic structure of ML-TMDCs depends on the dielectric environment, such as a supporting substrate [218], leading to bandgap and exciton energy renormalization [48-50]. Therefore, the dielectric constant (ε) of the substrate used for a molecule/ML-TMDC heterostructure is expected to impact its electronic properties and energy level alignment. Depending on the targeted functionality or device implementation of a molecule/ML-TMDC structure, very different substrates can be relevant, ranging from the often low ε of insulators to the highest possible one of metals. Knowledge of the molecule/ML-TMDC interface electronic properties is needed for guiding device design, but only very few systems have been studied to date, particularly on insulating substrates.

In this section, we investigate by XPS and ARUPS the electronic properties of ML-WS_2/C_{60} interfaces supported either on HOPG or c-sapphire. The two substrates were chosen because the electronic properties of HOPG resemble those of graphene [248], a promising electrode for nano-electronic devices [249, 250], and sapphire features transparency in the visible and near-infrared, thus often used in optical experiments. Both HOPG and sapphire have anisotropic but on-average similar dielectric constant values of about 10 [251, 252], suggesting a similar electronic properties of ML-WS_2 on both substrates, but experimental verification is not yet available. In contrast, the two substrates differ significantly in their electrical properties, and the influence of native SVs in WS_2, and their possible interplay with a supporting substrate (discussed in section 5.2) [44, 253, 254], on the electronic properties of the monolayer and its energy level alignment with a

MSC remains elusive to date. Fullerenes and their derivatives are prominent molecular semiconductors, widely employed in molecular-based optoelectronic devices [161, 162]. Notably, bulk MoS_2-C_{60} layered crystals (alternating layers of MoS_2 and C_{60}), which have been reported more than fifteen years ago, have been suggested to have potential for use in photovoltaic cells [255]. Theoretical work proposed that the combination of WS_2 and C_{60} should be more efficient for exciton dissociation compared to the MoS_2-C_{60} pair [256]. Still, very few investigations, notably experimental, of the electronic properties of C_{60} (and its derivatives)/TMDC have been reported so far [255, 257, 258]. A detail understanding of the impact of the substrate on the energy level alignment at C_{60}/TMDCs interfaces is still lacking. To contribute towards improved understanding of such hybrid systems, the electronic band line-up at the C_{60}/ML-WS_2 interface depending on the substrate is carefully evaluated.

5.3.1 Pristine WS_2 monolayer on sapphire and HOPG

SECO and ARUPS spectra of monolayer WS_2 on sapphire and HOPG are shown in **Figure 5.19**. From the SECO spectra shown in **Figure 5.19** (b) and (e), the work function (Φ) of pristine WS_2 on sapphire and HOPG is determined to 4.28 eV and 4.45 eV, respectively. The energy distribution curves (EDCs) measured at different take-off angles indicate that the valence band exhibits the energy versus momentum $E(\boldsymbol{k})$ dispersion expected for azimuthally disordered films, i.e. due to angular averaging the photoemission spectra consist of a linear superposition of the $\boldsymbol{k}$-DOS along the Γ-K and Γ-M directions [218, 226]. One local Valence band maximum (VBM) is observed at Γ-point and the global VBM is found at the K-point of the Brillouin zone (BZ) with binding energy (determined from the valence band emission onset) of 1.75 eV on sapphire and 1.42 eV on HOPG, demonstrating a more pronounced n-type behavior of the WS_2 film on sapphire as compared to that on HOPG. The WS_2 ionization energy (IE) with IE = Φ+VBM amount to 6.03 eV on sapphire and to 5.87 eV on HOPG. The latter value has a larger error margin because the surface patches not covered by ML-WS_2 (i.e., bare HOPG, typically < 10%) contribute to the area-average Φ [184]. It is also apparent that the ML-WS_2 on HOPG exhibits a narrower peak at Γ-point, indicating higher homogeneity on HOPG than on sapphire, which possibly relates to strain removal during the wet-transfer process [259]. Furthermore, the VBM being observed at the K-point confirms that the WS_2 sample actually consists of a monolayer [260], as for multilayers the VBM is located at Γ. As

discussed in section 5.2, for ML-WS_2/sapphire, the presence of dispersive states close to E_F indicates the filling of the CB at Q-point due to the ionization of electrons from SVs-induced defect states.

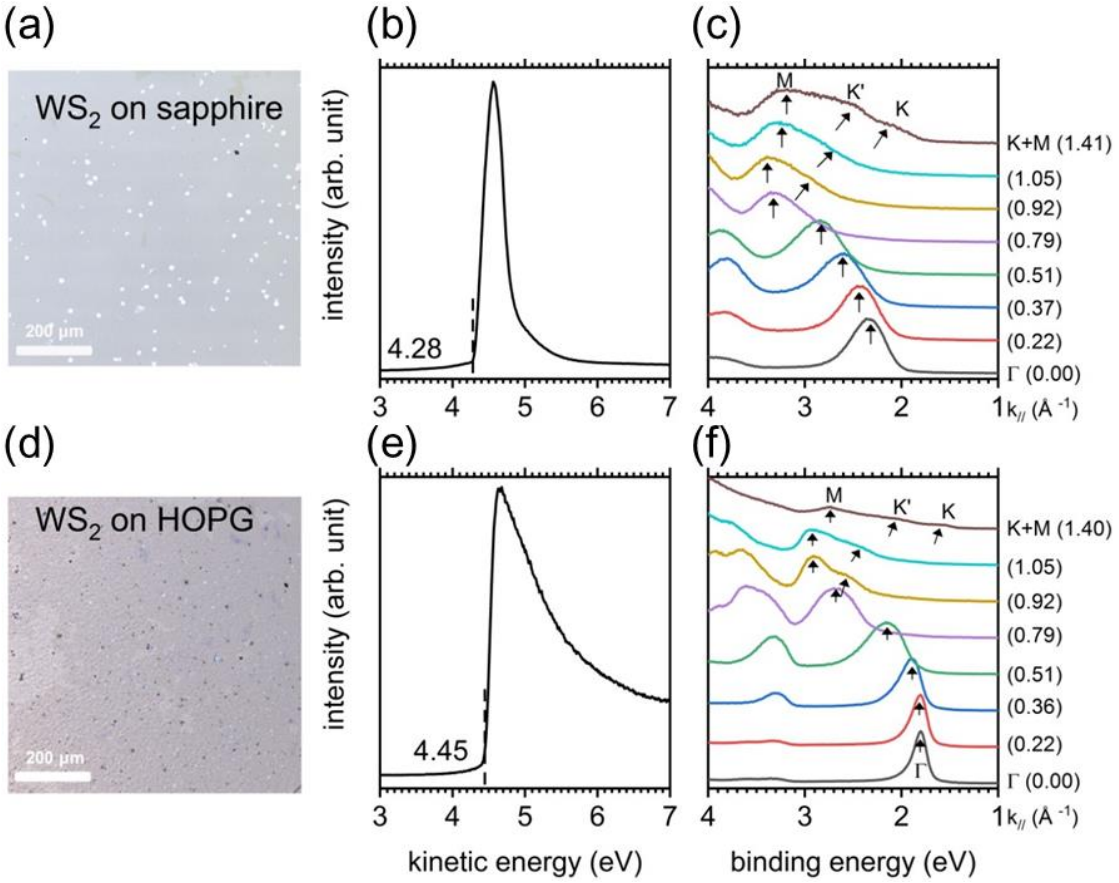

Figure 5.19 *(a,d) Optical microscope images of high-coverage ML-WS_2 on sapphire and HOPG. (b,c) SECO and ARUPS spectra of ML-WS_2 on sapphire. (e,f) SECO and ARUPS spectra of ML-WS_2 on HOPG. The arrows are guides for the band dispersion. Figures are taken from [200]*

5.3.2 C_{60}/ML-WS_2 on sapphire and HOPG

The morphology of a nominally 1 nm thick C_{60} film, deemed as ML, deposited on ML-WS_2/sapphire and on ML-WS_2/HOPG is presented in **Figure 5.20**. The atomic force microscopy (AFM) images exhibit a rather smooth C_{60} morphology in both cases, with root-mean-square (RMS) roughness values of ca. 1 nm on the shown areas. The images, particularly those with higher magnification, reveal that the C_{60} ML is not fully closed. On ML-WS_2/sapphire, C_{60} features rather small islands with local corrugation between them of ca. 1 nm, corresponding to the C_{60} molecular diameter [**Figure 5.20** (b)]. On ML-WS_2/HOPG, the apparent individual C_{60} islands are larger [**Figure 5.20** (d)]. In both cases, C_{60} covers the WS_2 surfaces quite well, and the smaller island size with insulating sapphire

as supporting substrate may be due to a laterally more corrugated electrostatic potential landscape, compared to a smoother one on the conductive HOPG. The presence of high-quality C_{60} layers on ML-WS_2 is a prerequisite for reliable assessment of the interfacial electronic properties when supported by different substrates.

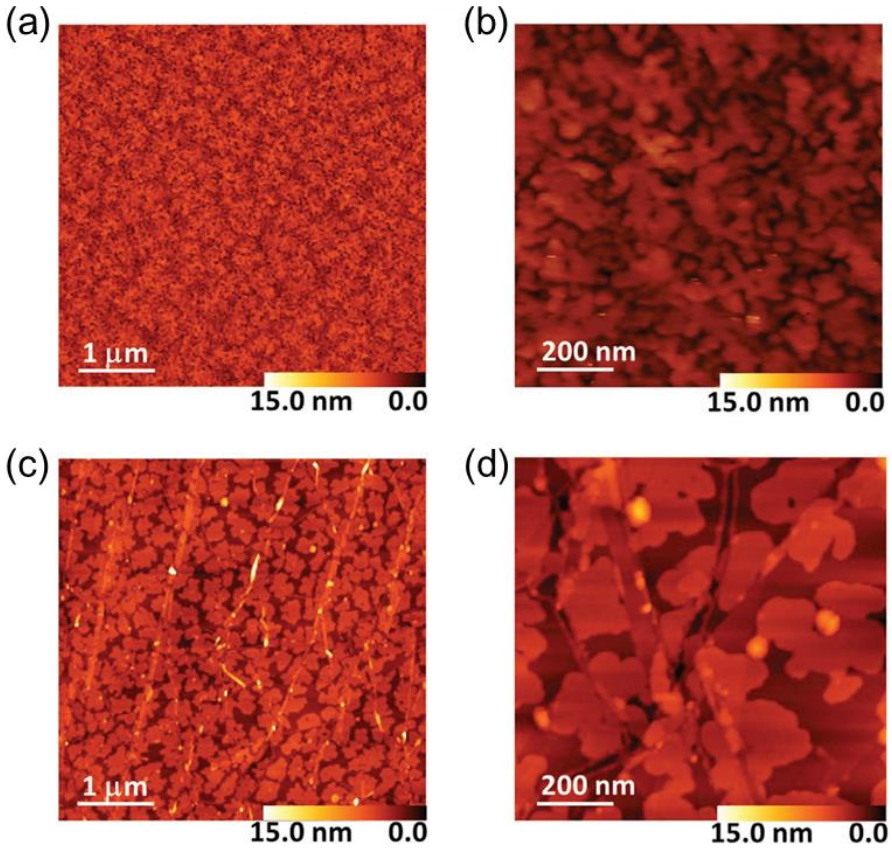

Figure 5.20 *AFM topography micrographs with different magnification of ca. ML-C_{60} (nominal thickness: 1 nm) deposited on (a, b) ML-WS_2/sapphire and (c, d) ML-WS_2/HOPG. The RMS roughness values of the shown areas are: (a) 1.0, (b) 1.0, (c) 1.1, and (d) 1.0 nm. Figures are taken from [200]*

C_{60} thin films were incrementally deposited in-situ onto ML-WS_2 on the different substrates and each deposition step was then characterized by ARUPS and XPS. The UPS spectra are shown in **Figure 5.21** upon stepwise deposition of C_{60} collected at Γ- and K-point. At Γ-point, despite not corresponding to the global VBM of WS_2, the WS_2 features show the strongest signal, helping track more precisely any energy shift of the WS_2 valence band upon C_{60} deposition. At K-point, one can determine precisely the energy offset between the frontier energy levels of the two materials forming the heterojunction. From **Figure 5.21** (a) and (d), the SECO spectra provide constant Φ values of 4.28 and 4.45 eV for ML-WS_2/sapphire and ML-WS_2/HOPG with increasing C_{60} thickness,

demonstrating that the energy level alignment essentially follows the Schottky-Mott rule, i.e., vacuum level alignment takes place upon interface formation. We stress that the lack of dipole formation at the very interface indicates the absence of any significant electron transfer towards the C_{60} molecules in both cases. This is in contrast to what was observed at the fluorinated fullerene $C_{60}F_{48}$/ML-WS_2 interface on HOPG [258], and is in line with the significantly larger electron affinity of $C_{60}F_{48}$ of ca. 5.0 eV [261] compared to that of C_{60} of only ca. 4.0 eV [262].

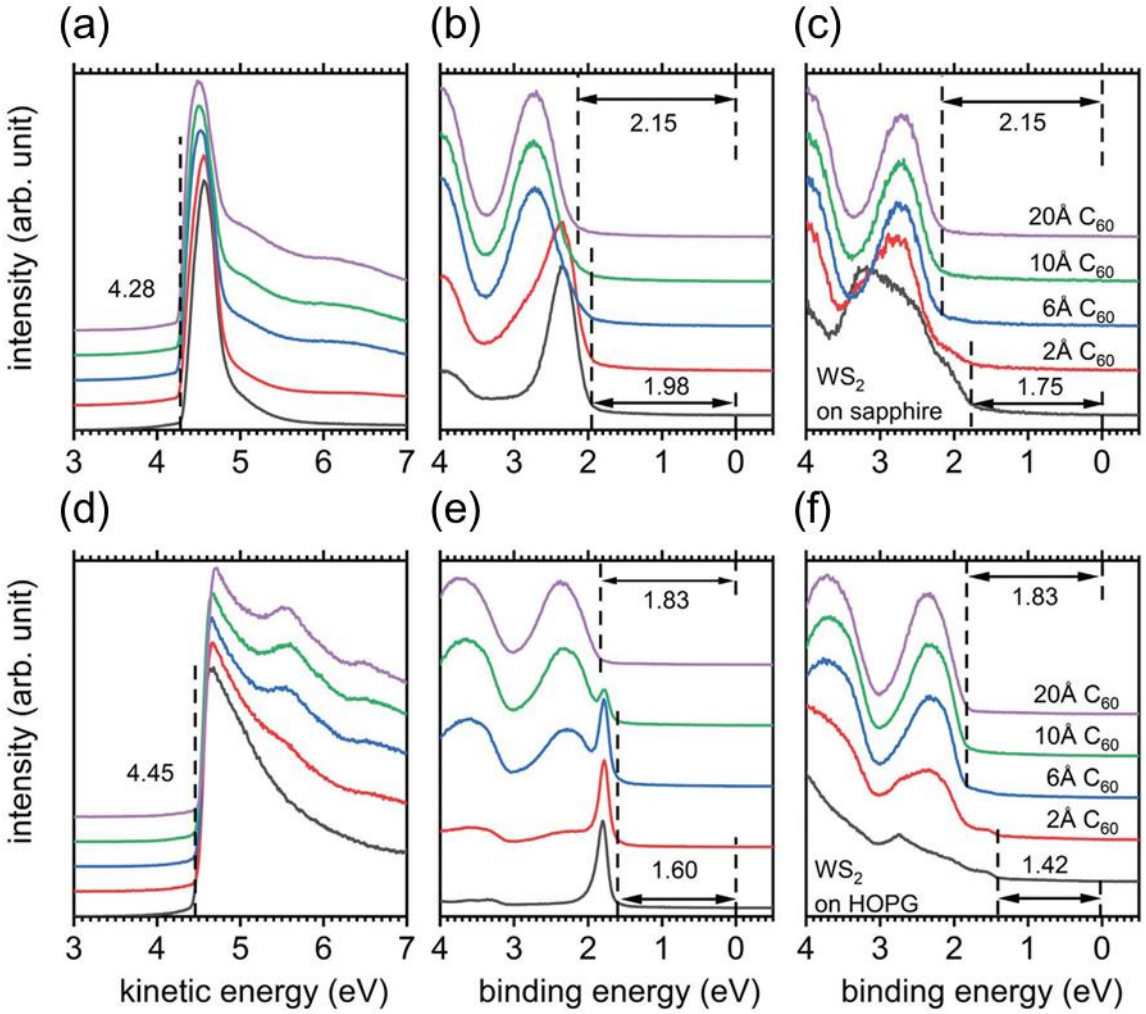

Figure 5.21 *ARUPS spectra of ML-WS_2/substrate (sapphire: top row; HOPG: bottom row) with increasing C_{60} coverage, as indicated. a,d) SECO region. (b,e) Valence region at the Γ point and (c,f) at the K/M points of the BZ. The intensity is normalized for better clarity. Figures are taken from [200]*

As displayed in **Figure 5.21** (b) and (e), upon C_{60} deposition the UPS spectra taken at Γ-point for both samples show an increasing intensity on the high binding energy side of the sharp WS_2 peak. This emission can readily be attributed to the C_{60} HOMO. Alongside with

increasing C_{60} deposition, the spectral intensity from WS_2 becomes weaker and completely vanishes for thicknesses between 1 and 2 nm, which, considering the small photoelectron mean free path (< 1 nm) at the energies involved, suggest layered growth of C_{60} on WS_2 beyond the ML. The sharp WS_2 peak at Γ-point remains constant in energy upon C_{60} adsorption. This strongly suggests that the local VBM energy position is also constant for both studied systems.Constant C_{60} HOMO onset are further determined at 2.15 and 1.80 eV binding energy on ML-WS_2/sapphire and ML-WS_2/HOPG, respectively. However, a clear signal from ML-WS_2 is observed only up to 0.6 nm C_{60} coverage. Additional support for unchanged ML-WS_2 energy levels also for thicker C_{60} layers comes from inspection of spectra where the (intensity-scaled) contribution of bare ML-WS_2 was subtracted from the measured spectra, shown in **Figure 5.22**, The residuals are clear replicas of the C_{60} valence features, without any apparent energy shift or shape-change. With this, we can directly assess the energy difference between VBM of ML-WS_2 and C_{60} HOMO onset, which amounts to 0.40-0.41 eV for both substrates.

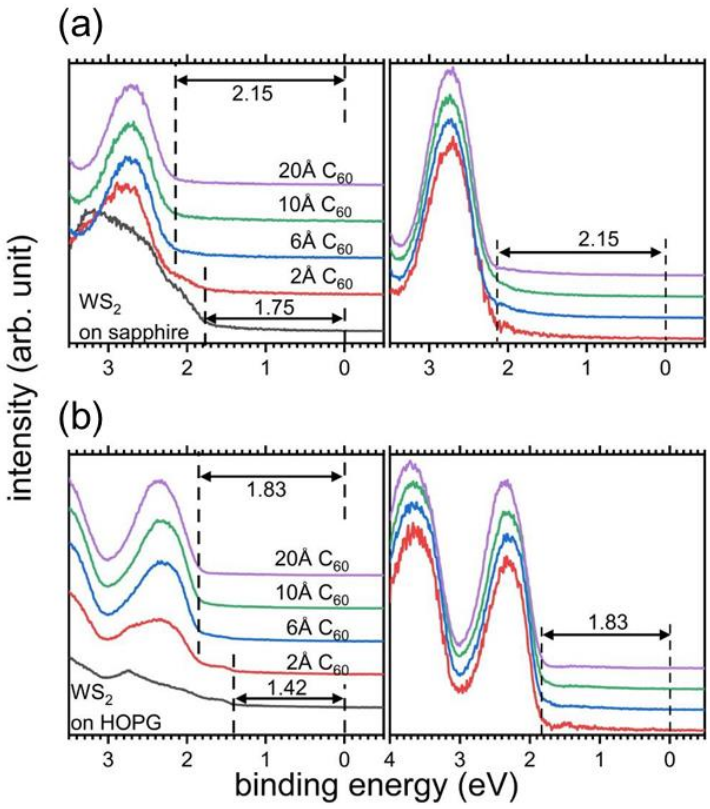

Figure 5.22 *UPS spectra of C_{60} with different thickness. Thickness-dependent UPS spectra of C_{60}/ML-WS_2 measured at K-point of ML-WS_2 (left panels) and of C_{60} contribution after subtracting the WS_2 background (right panel) (a) on sapphire and (b) on HOPG. The intensity of the spectra is normalized for better clarity. Figures are taken from [200]*

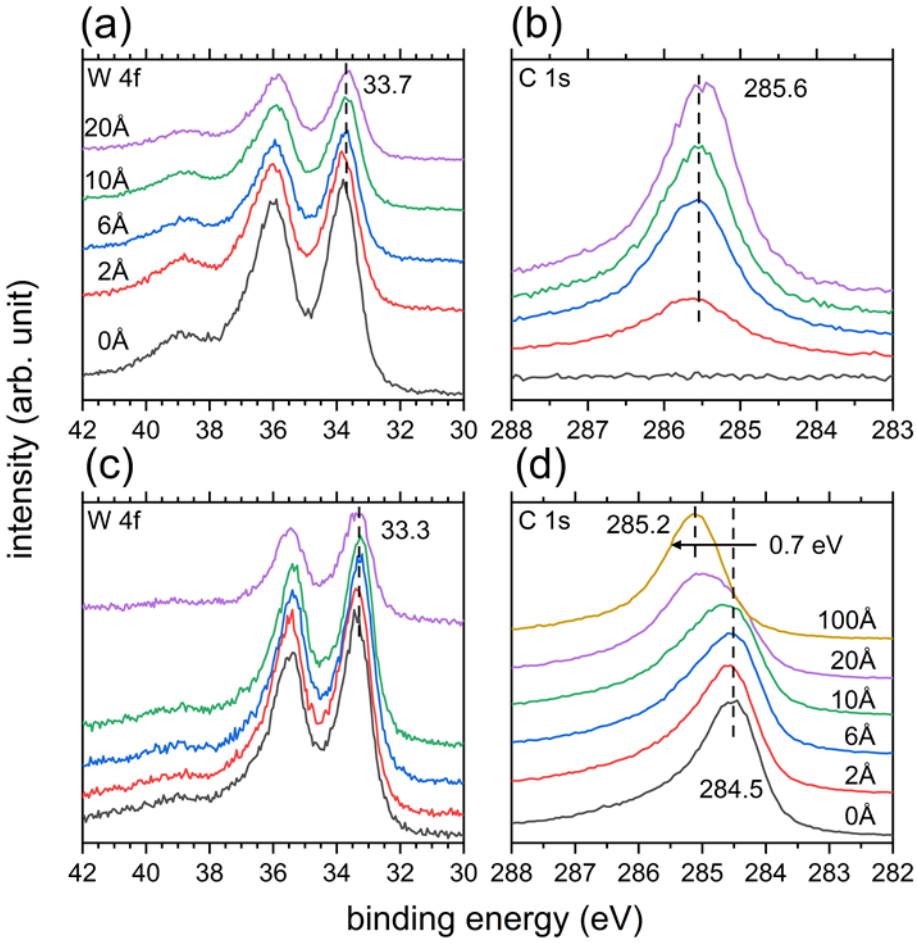

Figure 5.23 *Fit of the C 1s core level spectra for C_{60}/ML-WS_2/HOPG with sequential deposition of C_{60} from 2 Å to 100 Å. Constant binding energy is found for the C 1s from HOPG (284.5 eV) and that of C_{60} (ca. 285.2 eV). Figures are taken from [200]*

We finally attend to the W 4f and C 1s core level spectra from XPS for C_{60}/ML-WS_2 (shown in **Figure 5.23**), to further evaluate interfacial interactions on the different supporting substrates. For the heterostructure on sapphire, no apparent changes are obseved in the shape and position of the W 4f and C 1s levels upon deposition of C_{60}, fully consist with our conclusions above from the ARUPS results. With HOPG as substrate, the W 4f core levels also show no change upon C_{60} deposition. However, they are shifted ca. 0.4 eV towards lower binding energy compared to those on the sapphire substrate. Since the valence levels of ML-WS_2 on both substrates are also shifted by the caparable amount (0.33 eV), this supports the notion of an electrostatic origin of the shift, most likely indeed rooted in the transfer of ML-WS_2 CB towards HOPG and the apparent reduced n-type character. In contrast, the C 1s peak in **Figure 5.23** (d) seems to gradually shift upon C_{60} deposition. But here we already start with the carbon signal from the HOPG substrate, at ca.

283.9 eV binding energy. As shown in **Figure 5.24**, the addition of a second C 1s component fixed at 0.7 eV higher binding energy is sufficient to adequately fit all spectra with intermediate C_{60} coverage. Thus, this second C 1s component can be assigned to stem from C_{60}, and we conclude on constant shape and binding energy, again in full consistency with the ARUPS results.

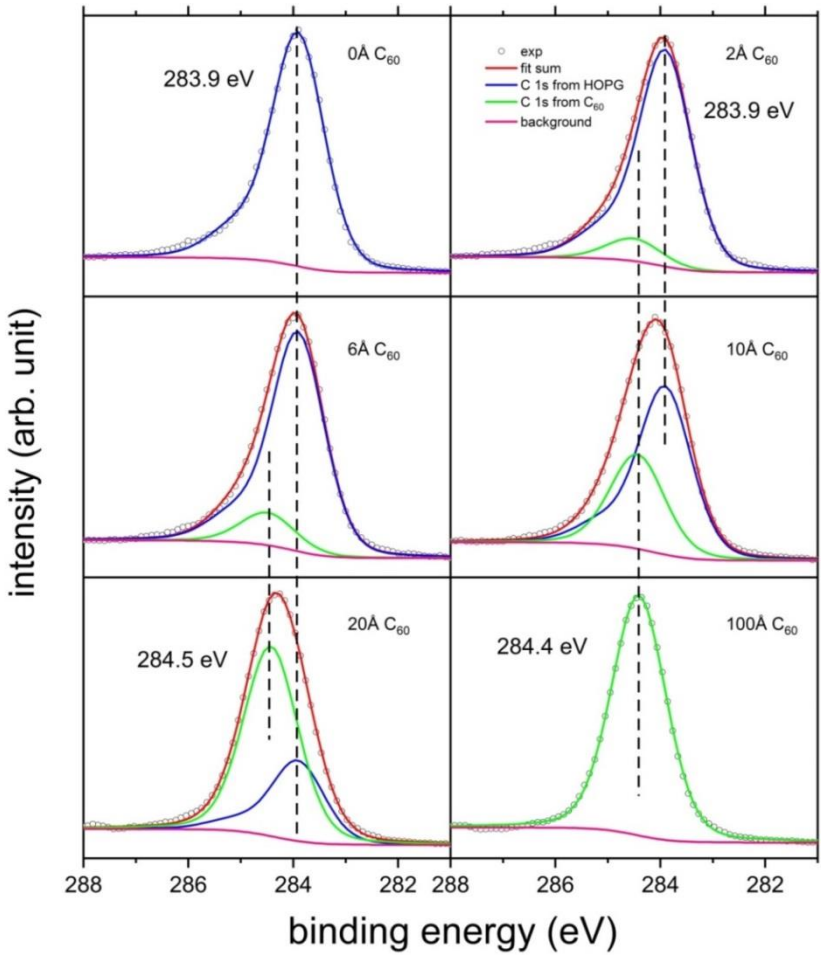

Figure 5.24 *Fit of the C 1s core level spectra for C_{60}/ML-WS_2/HOPG with sequential deposition of C_{60} from 2 Å to 100 Å. Constant binding energy is found for the C 1s from HOPG (284.5 eV) and that of C_{60} (ca. 285.2 eV). Figures are taken from [200]*

5.3.3 Interfacial energy level diagrams

Having accessed the alignment of the occupied energy levels of C_{60}/ML-WS_2 on both substrates above, we now turn towards describing the full interfacial energy level diagrams. It is noted that our ML-WS_2/sapphire sample undergoes the annealing process to acquire reliable PES data. As discussed in section 5.2, the annealing process gives rise to the SVs-induced band structure renormalization on sapphire substrate, that is, the dominant CBM is located few meV below the E_F at Q-point with EA of ca. 4.2 eV. The IE of ML-WS_2 is

determined by adding the global VBM binding energy to the sample Φ, yielding 6.03 eV. The IE of C_{60} absorbed on ML-WS_2 is obtained by adding the binding energy of the HOMO level onset to Φ, resulting in 6.43 eV. The corresponding electron affinity (EA) values are estimated by subtracting the bandgap of C_{60} from the IE, yielding 4.03. All energy levels and the measured position of E_F are summarized in **Figure 5.25** for C_{60}/defective ML-WS_2/sapphire. Constant Φ and VB onset values of 4.28 and 2.15 eV for C_{60} up to 2 nm coverage imply that vacuum level alignment prevails. The formation of a type I heterojunction is observed, which indicates the accumulation of excitons on the ML-WS_2 side for this metastable situation under photoexcitation.

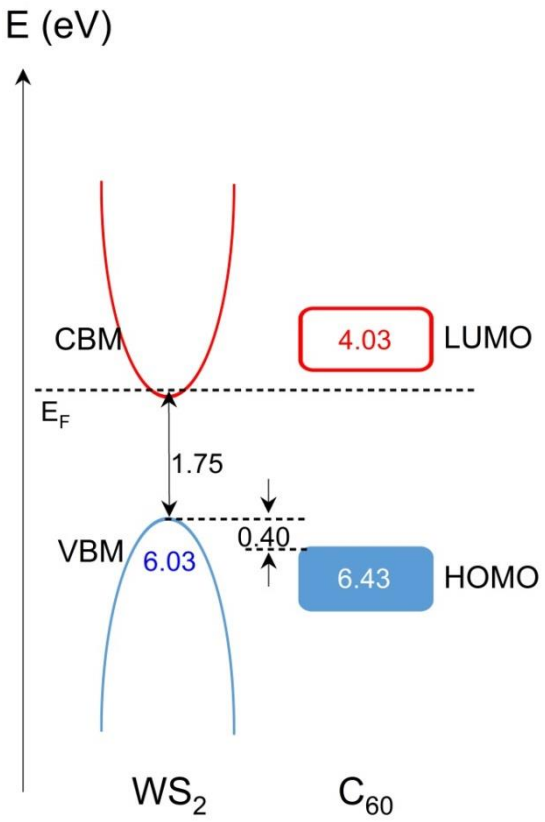

Figure 5.25 *Schematic energy level diagram for C_{60}/defective ML-WS_2/sapphire. The blue and red lines depict the occupied and unoccupied levels, respectively. All values are given in eV, the EA and IE values with respect to the vacuum level, set to zero.*

As concluded in section 5.2.5, molecular or atomic oxygen (following potential dissociative adsorption) binds to SVs sites and eliminates the associated donor states, which results in the removal of band renormalization of ML-WS_2 on sapphire. Therefore, the interfacial energy level diagram of C_{60}/defective ML-WS_2/sapphire discussed here is a metastable case, which holds only in the high vacuum conditions. In addition, for the actual fabrication of devices, it is unnecessary to anneal the ML-WS_2/sapphire in high

vacuum. Thus, we propose the estimated interfacial energy diagram of C_{60}/ "perfect" ML-WS_2/sapphire for guiding the device fabrications as in **Figure 5.27** (a), while of C_{60}/ML-WS_2/HOPG, since no band renormalization was observed as detailed in section 5.2, one can obtain the interfacial energy level diagram of C_{60}/ML-WS_2/HOPG. These two schematic energy level diagrams can provide a reference for further device design and fabrication.

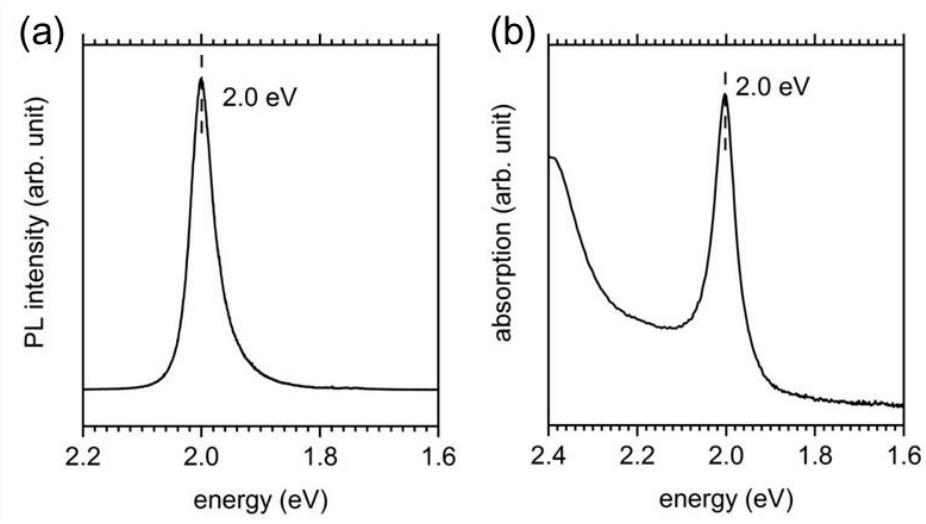

Figure 5.26 *(a) PL and (b) absorption spectra of as-grown ML-WS_2 on sapphire. The emission of sapphire (peak at ca. 1.8 eV) was subtracted for better clarity. Figures are taken from [200]*

In the case of discussing ELA regarding C_{60}/ "perfect" ML-WS_2, the IE of ML-WS_2 was determined by adding the global VBM onset binding energy to the sample Φ, resulting in 6.03 eV (on sapphire) and 5.87 eV (on HOPG). As shown in **Figure 5.26**, an optical gap (lowest exciton energy) of 2.0 eV as expected for the ML-WS_2. To estimate the conduction band minimum (CBM) energy above E_F at the K-point, one can add the exciton binding energy to the optical gap yielding the electronic (single particle) bandgap. The exciton binding energy reported for ML-WS_2 ranges from 0.71 eV to 0.28 eV [19, 263-265]. The higher values were determined with silicon oxide substrates and the lower one on sapphire, but all employing optical spectroscopy methods only. For the related TMDCs MoS_2 and WSe_2, the exciton binding energy was obtained by direct measurements of the optical and single particle gaps with sapphire as substrate, amounting to 0.24 eV [219].Since sapphire and HOPG have similar dielectric constant of ca. 10, value of the bandgap of ML-WS_2 was estimated at ca. 2.24 eV. Thus, the corresponding electron affinity (EA) values are estimated by subtracting the bandgap from the IE, yielding 3.79 eV (sapphire) and 3.63 eV (HOPG). In analogy, the IE of the C_{60} layers atop ML-WS_2 is obtained by adding the

binding energy of the HOMO level onset to Φ, giving 6.43 eV (on sapphire) and 6.28 eV (on HOPG). The C_{60} electronic gap was reported to be 2.3 eV, and more recently reassessed to be 2.4 eV, so that we obtain EA values of 4.03 eV (sapphire) and 3.88 eV (HOPG). The small difference in the measured IE (and estimated EA) of C_{60} on the two substrates might be due to variations of film morphology, as already ca. ML C_{60} exhibits different morphology (see **Figure 5.20**). The observations in a previous study could suggest that smoother C_{60} morphology results in lower IE [266]. All energy levels are summarized in **Figure 5.27** for both substrates. For both studied structures, the formation of a type-II heterojunction with C_{60} acting as the electron acceptor component is observed, in qualitative agreement with recently reported theoretical modeling data [256]. Notably, the energy offset between the two components' frontier energy levels is nearly identical on both supporting substrates, with 0.4 eV for holes and 0.24 eV for electrons. This is due to the fact that both interfaces exhibited vacuum level alignment, that is, negligible charge density reorganization upon contact. At first glance, the C_{60}/ML-WS_2 interface is expected to enable efficient charge separation after optical excitation of either component, which could be used in photodetectors or photovoltaic applications. However, we recall that ML-WS_2 is an excitonic semiconductor, with the energy of the first optical transition-forming the exciton-being at least 0.24 eV lower in energy than the bandgap. Looking at **Figure 5.27**, we realize that the energy offset between the single-particle unoccupied levels (global CBM and LUMO) has the same magnitude as the WS_2 exciton binding energy, so that interfacial charge transfer might actually require excitation with an energy larger than the first exciton of the inorganic semiconductor ML.

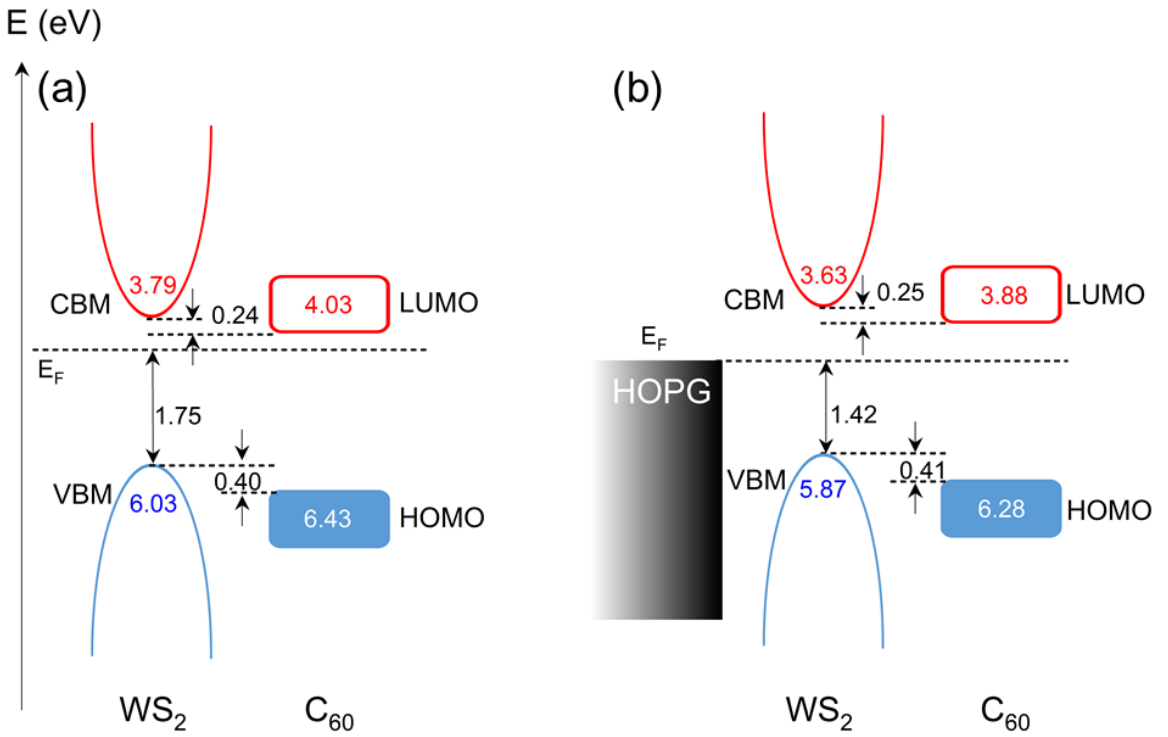

Figure 5.27 *Schematic energy level diagrams for (a) C_{60}/"perfect"ML-WS_2/sapphire and (b) C_{60}/ML-WS_2/HOPG. The blue and red lines depict the occupied and unoccupied levels, respectively. All values are given in eV, the EA and IE values with respect to the vacuum level, set to zero. Figures are adapted from [200]*

5.3.4 Conclusion

We studied the electronic properties of a prototypical heterostructure formed by a MSC (C_{60}) and a 2D inorganic semiconductor (ML-WS_2), on two different supporting substrates. Independent of whether the substrate is insulating (sapphire) or conductive (HOPG), no indication of ground-state charge transfer upon interface formation was found, that is, vacuum level alignment prevailed. Although SVs-induced band structure renormalization was observed from the defective ML-WS_2/sapphire sample, SVs sites can be filled by molecular or atomic oxygen, resulting in band renormalization removal. Thus, we ignore the effect of SVs-induced band renormalization and propose the interfacial energy diagram of C_{60}/"perfect" ML-WS_2 on both substrates, which is more applicable to the devices in air. In terms of "perfect" ML-WS_2, the energy offsets between the occupied and unoccupied frontier electronic levels of C_{60} and ML-WS_2 were estimated to be almost identical for both substrates. Overall, the C_{60}/"perfect" ML-WS_2 interface is characterized by a type-II level alignment, with C_{60} acting as an electron acceptor, which makes this heterostructure interesting for further investigations in photo-responsive device structures. However, the

energy level offset between the global CBM of ML-WS_2 and the C_{60} LUMO is virtually equal to the exciton binding energy of the inorganic ML, thus efficient electron transfer after optical excitation may only occur for excitation energies higher than the ML-WS_2 fundamental exciton.

5.4 Optoelectronic properties at the F_6TCNNQ/ML-WS_2 interface

Recent studies have demonstrated that interfacial optical transitions can occur at MSC/ML-TMDC interfaces [31, 205, 267, 268]. For example, charge transfer (CT) excitons were observed at tetracene/WS_2 [269] or ZnPc/MoS_2 heterostructures [270] and were attributed to the CT process occurring at the MSC/TMDC interfaces under photoexcitation. TMDCs normally exhibit a range of structural defects such as sulfur vacancies (SVs). Meanwhile, CT process was verified at a MSC/defective ML-TMDC interface on the ground states and then give rise to new ionized states in the bandgap [218]. Here, we aim at understanding how defects can impact both the ground and excited states at a MSC/ML-TMDC interface. Indeed, it is reasonable to assume that the presence of SVs in the TMDC can influence the ground state of the interface, which may therefore favor the emergence of new optical transitions at the MSC/ML-TMDC interface. Relating the ground states electronic properties and excited states of such systems by assessing their density of states and the corresponding electronic transitions should therefore provide fundamental insights into the microscopic electronic processes taking place at these interfaces.

In this section, we investigate and compare the optical and electronic properties of an interface combining a strong p-dopant molecule, F_6TCNNQ adsorbed on the pristine (as-grown sample with low density of SVs) and defective ML-WS_2 (with a high density of SVs) supported on sapphire using ARPES and UV-Vis absorption. A series of new absorption peaks arise from F_6TCNNQ/defective ML-WS_2, which are absent from F_6TCNNQ/pristine ML-WS_2. These new optical transitions at the corresponding interfaces are interpreted to the ionic F_6TCNNQ and a hybrid molecule-to-TMDC electronic transition via ARPES measurements. These results demonstrate that defect engineering of ML-TMDC can not only modify the optoelectronic properties of the monolayers but also their related interfaces with for instance strong p-type organic semiconductors.

5.4.1 Optical properties of $F_6TCNNQ/ML\text{-}WS_2$

Firstly, the absorption spectrum of our homemade ML-WS_2 on sapphire is shown as the black curve in **Figure 5.28.** The sharp peak with high intensity around 2 eV corresponds to the typical excitation transition of pristine ML-WS_2. Then, the absorption spectrum of 10 nm F_6TCNNQ deposited on the pristine ML-WS_2 is observed as the red curve in **Figure 5.28.** After subtracting pristine WS_2 contribution from the red curve, the substrated spectrum is clear replicas of neutral F_6TCNNQ on quartz [271] as shown in **Figure 5.29**, indicating that the red curve is consist of a superposition of the ML-WS_2 and neutral F_6TCNNQ contributions. This strongly suggests that no obvious ground-state charge transfer process is found at the F_6TCNNQ/pristine ML-WS_2 interface. After that, this sample (10 nm F_6TCNNQ deposited on pristine ML-WS_2) underwent an annealing process, that is, annealing at 1000 K for 24 h in the UHV chamber, in order to i) remove the F_6TCNNQ on the surface and ii) provide the defective ML-WS_2 sample with a high density of SVs. Moreover, we deposited again 10 nm F_6TCNNQ on this defective ML-WS_2 and obtained the corresponding absorption spectrum as the blue curve in **Figure 5.28**. Several new peaks appear, which are absent on the pristine ML-WS_2 film. As discussed in section 5.2, such annealing-induced SVs, acting as n-type dopants, result in the filling of the conduction band of ML-WS_2 [31]. Since F_6TCNNQ is a strong electron acceptor molecule with an electron affinity of 5.6 eV [271, 272], electrons on the CBM of ML-WS_2 can easily transfer to F_6TCNNQ LUMO, leading to the formation of F_6TCNNQ anion, resulting in new optical transitions at the F_6TCNNQ/defective ML-WS_2 interface.

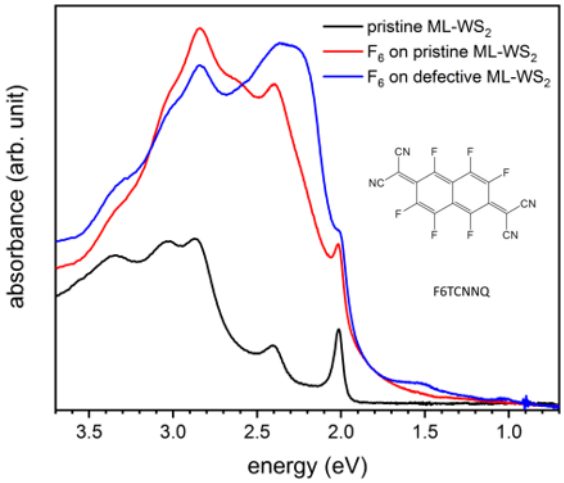

Figure 5.28 *Absorption spectra of pristine ML-WS_2/sapphire (black), F_6TCNNQ/pristine ML-WS_2/sapphire (red), and F_6TCNNQ/defective ML-WS_2/sapphire (blue). Insert: Molecular structure of F_6TCNNQ*

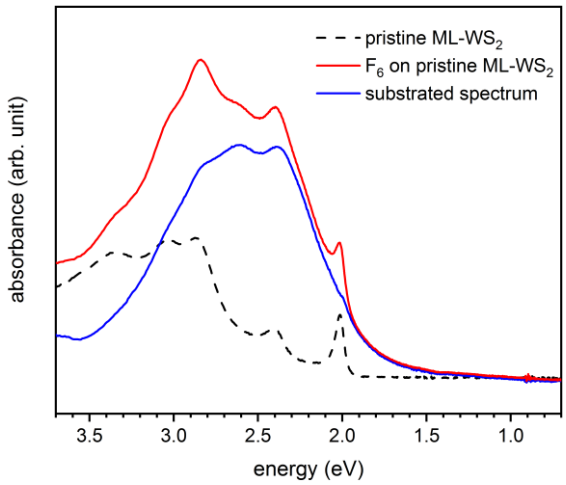

Figure 5.29 *Absorption spectra of pristine ML-WS_2/sapphire (black dash line), F_6TCNNQ/pristine ML-WS_2/sapphire (red), and F_6TCNNQ contribution (blue) after subtracting the pristine ML-WS_2 background.*

Figure 5.30 (a) shows the zoomed spectra at a low energy range (1.8-1.0 eV) after subtracting the Rayleigh scattering background. The board peaks in the range of 1.4 to 1 eV from F_6TCNNQ/pristine ML-WS_2, as red curve, are most likely due to the impurity in F_6TCNNQ powders by comparing with the absorption spectrum in the same energy range of F_6TCNNQ in dichloromethane (DCM) solvent, as shown in **Figure 5.31** (a). Apparent peaks appear in the range of 1.7 to 0.9 eV from the F_6TCNNQ/defective ML-WS_2 spectrum as the blue curve in **Figure 5.30** (a). The fitted spectra shown in **Figure 5.30** (b) demonstrate that the board peak can be preliminarily divided into 4 peaks at 1.02, 1.22, 1.40, and 1.53 eV, respectively (marked as peak A, B, C, and D). By comparing the fitted peaks with the absorption spectrum of anionic F_6TCNNQ in acetonitrile in **Figure 5.31** (b), the peak at 1.02, 1.22, and 1.40 eV can be attributed to the vibronic structure of F_6TCNNQ anion [271, 272]. The peak at 1.53 eV from the F_6TCNNQ/defective ML-WS_2 system is further estimated by using ARUPS measurements.

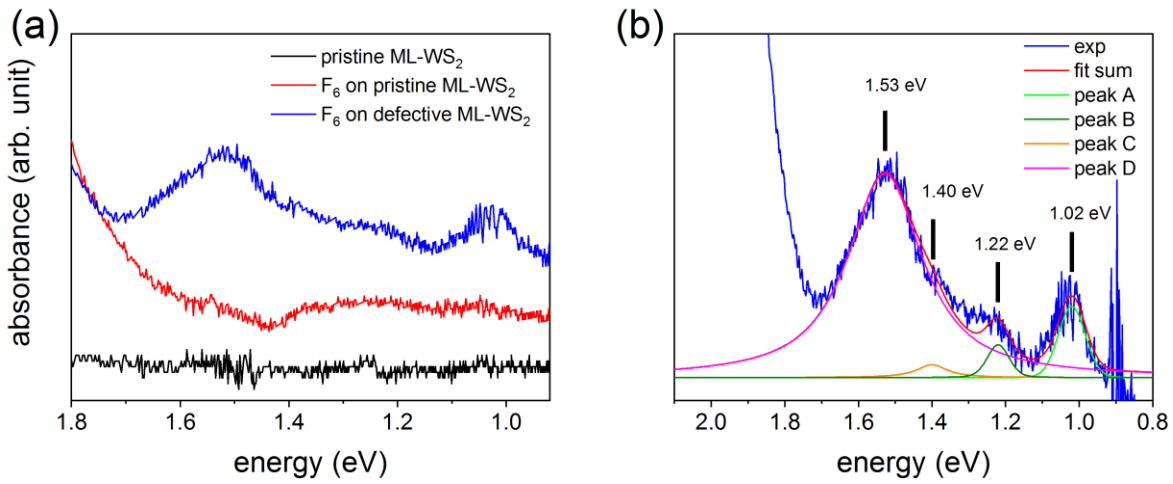

Figure 5.30 *(a) Zoom-in absorption spectra of pristine ML-WS_2/sapphire (black), F_6TCNNQ/pristine ML-WS_2/sapphire (red), and F_6TCNNQ/defective ML-WS_2/sapphire (blue) after subtracting the Rayleigh scattering background. (b) Fit spectra of F_6TCNNQ/defective ML-WS_2/sapphire. Peak A (1.02 eV), B (1.22 eV), and C (1.40 eV) refer to the vibronic structure of F_6TCNNQ anion.*

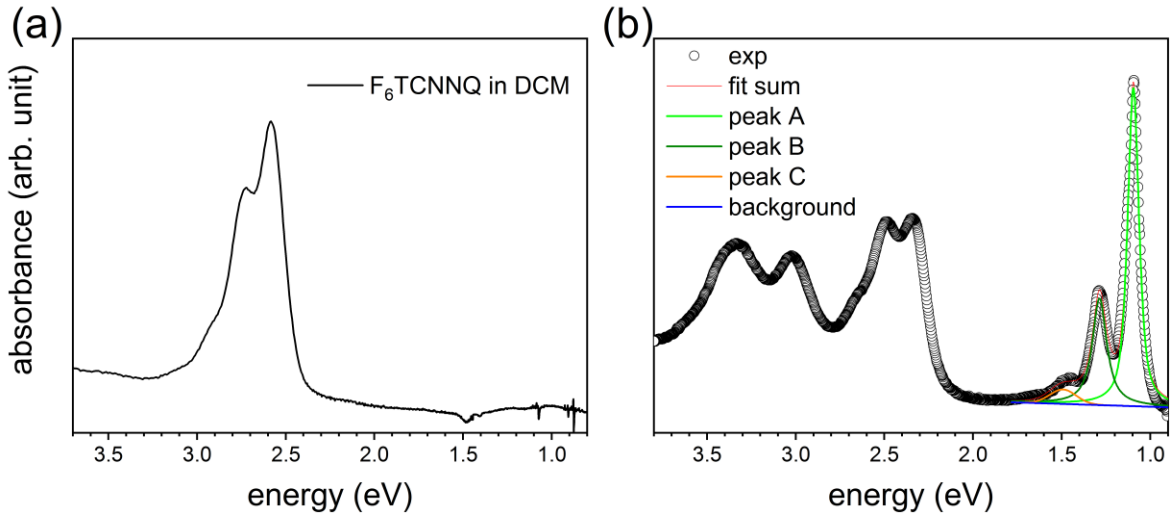

Figure 5.31 *(a) Absorption spectrum for neutral F_6TCNNQ measured in dichloromethane (DCM). The concentration is 0.5mg/ml. (b) Absorption spectrum of F_6TCNNQ anion measured in acetonitrile (CH_3CN) upon admixing the LiI served as donor dopant. The concentration of F_6TCNNQ is 0.5 mg/ml dissolved in saturated LiI/acetonitrile solution. The F_6TCNNQ anion features vibrionic optical transitions (peak A, B, and C) in the range of 1-1.5 eV.*

5.4.2 Electronic structure of F_6TCNNQ/defective ML-WS_2

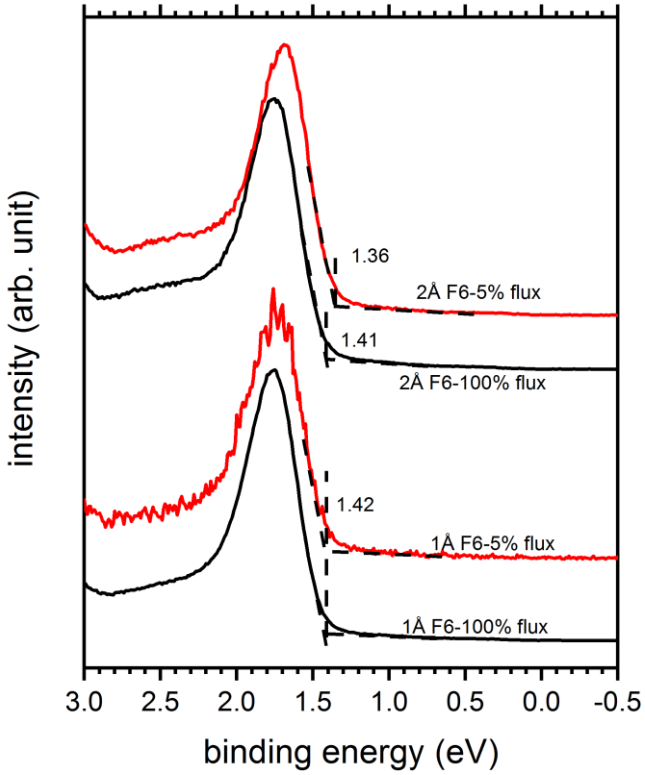

Figure 5.32 *UPS spectra of (bottom) 1 Å and (top) 2 Å F_6TCNNQ deposited on defective ML-WS_2/sapphire measured under different UV flux.*

To investigate the optical transition around 1.53 eV from F_6TCNNQ/defective ML-WS_2, ARPES measurements were performed for ML-WS_2 on sapphire after 24h annealing at 1000K and with step depositions of F_6TCNNQ afterward. After such annealing process, the sample provides sufficient conductivity for ARUPS measurement without charging (enabled via electrical contacts through the metal clamps mechanically fixing the sample) and contributes to a reliable ARPES result. However, as mentioned above, the F_6TCNNQ can withdraw the electron from the defective ML-WS_2, thus, decreasing the electron density of the sample, and induce the charging during the ARPES measurements. As shown in **Figure 5.32**, we observed almost no shift of VB onset for 1 Å F_6TCNNQ/defective ML-WS_2, and a slight shift (less than 0.1 eV) to higher BE by charging at the thickness of 2 Å F_6TCNNQ depositing on defective ML-WS_2 under different UV flux. This indicates the measured sample starts to charging with the thickness of F_6TCNNQ around 2 Å. Thereforethe ARUPS data becomes unreliable when the thickness is over 2 Å. It is noted that the electronic structure of F_6TCNNQ/defective ML-

WS_2 and the energy level diagram discussed in this section are determined on the ARUPS data of 1 and 2 Å F_6TCNNQ deposited on defective ML-WS_2 on sapphire.

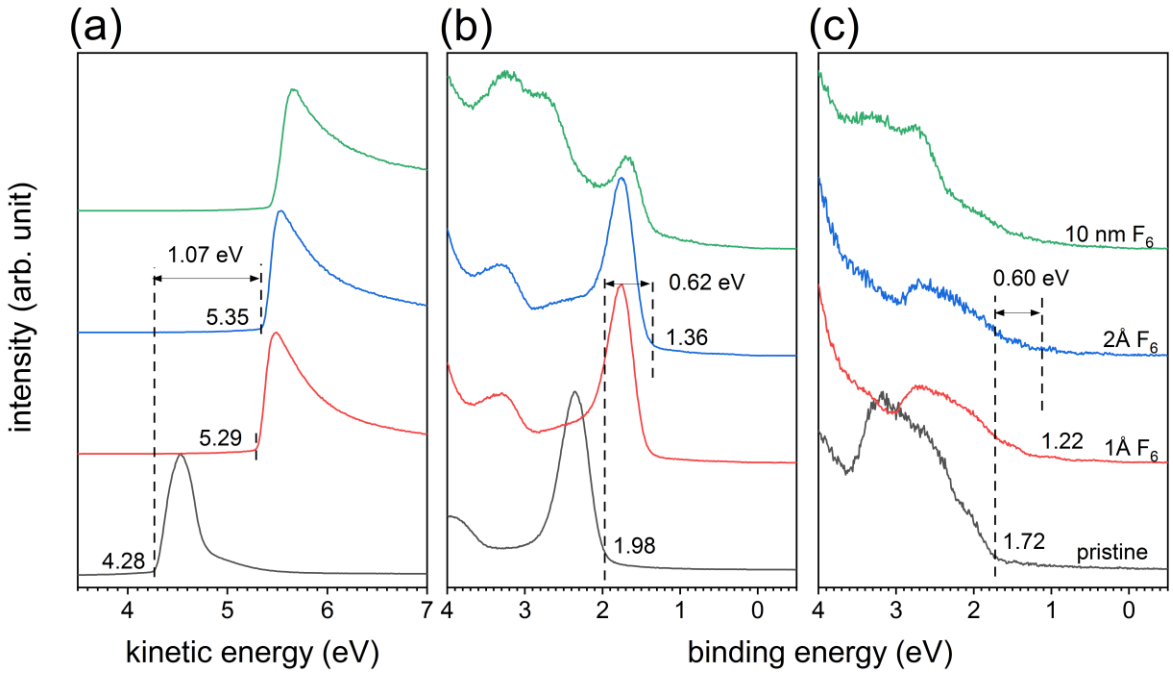

Figure 5.33 *ARUPS spectra of F_6TCNNQ/defective ML-WS_2/sapphire. (a) Secondary electron cutoff and valence band spectra at (b) Γ-point and (c) K-point with increasing F_6TCNNQ coverage.*

The secondary electron cutoff and the valence spectra of pristine WS_2 are shown as the black curve in **Figure 5.33**. We determine the work function (Φ) of defective ML-WS_2/sapphire of 4.28 eV. The SECO are determined at 5.29 and 5.35 eV at a nominal thickness of 1and 2 Å, respectively. An approximate saturated Φ increase of approximately +1.07 eV is observed at a nominal thickness of 2 Å with incremental coverage of F_6TCNNQ onto ML-WS_2.

Figure 5.33 (b) and (c) show the corresponding VB spectra at the Γ- and K-point of the Brillouin zone. The VB spectra at Γ-point exhibited a strong sharp peak which helps us to precisely track the energy shift of the WS_2 valence band by stepwise depositing F_6TCNNQ. For clarity, the energy onset at Γ-point does not stand for the global valence band maximum but at K-point, which intuitional determines the relevant energy between the frontier energy levels of the two materials. Thus, the valence band onset is 1.72 eV below the E_F on sapphire as shown in **Figure 5.33** (c). The defective ML-WS_2 pronouncedly exhibits n-type behavior which is attributed to the native SVs induced by annealing process. Therefore, after depositing strong p-type material F_6TCNNQ onto defective ML-WS_2, electron transfer can take place at the F_6TCNNQ/defective ML-WS_2 interface and

contribute an approximately 0.6 eV VBM shifting to the lower binding energy. SECO exhibits a larger shift compared to the shift of VBM, which is most likely due to the orbital polarization [218].

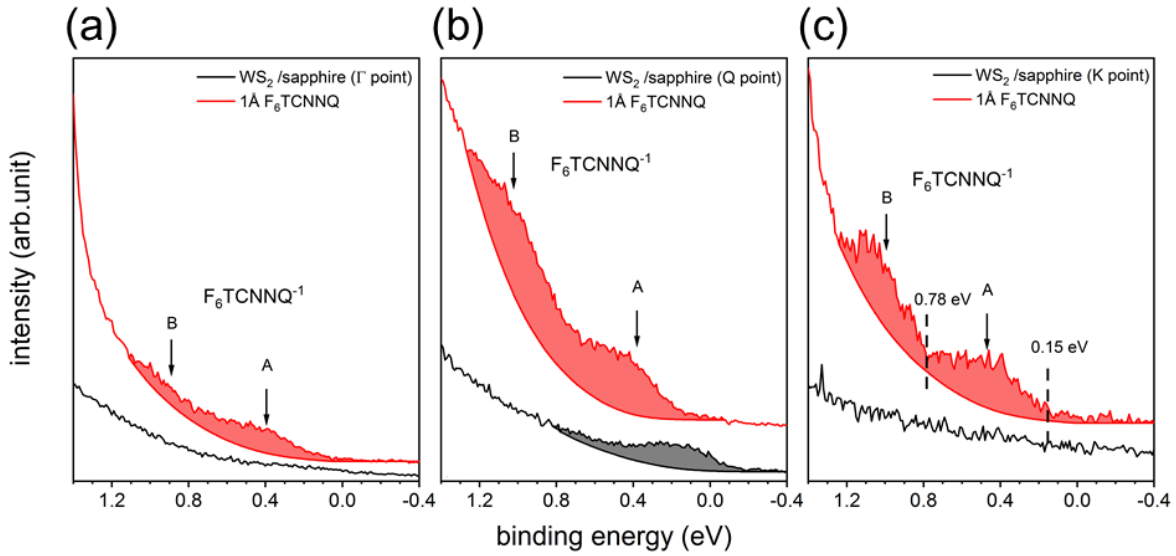

Figure 5.34 *Zoom-in ARUPS spectra of defective ML-WS_2/sapphire and F_6TCNNQ/defective ML-WS_2/sapphire in the near E_F energy range at (a) Γ-point, (b) Q-point, and (c) K-point.*

For further studying the charge transfer mechanism and new derived energy levels at the interface, high-resolution VB spectra of F_6TCNNQ/defective ML-WS_2 nearby the E_F are obtained before and after depositing 1 Å F_6TCNNQ at the Γ-, Q-, and K- point as shown in **Figure 5.34**. A weak feature is clearly observed only at the Q-point of defective ML-WS_2 closed to the E_F, which is due to the partially filled of CBM at the Q-point. As discussed in section 5.2, SVs induced by annealing lead to n-type doping and compressive strain within monolayers on sapphire and further renormalize the band structure. These include the emergence of E_F above the CBM at Q- instead of K-point for defective ML-WS_2/sapphire. Therefore, the electron from the defective ML-WS_2 CBM with BE of ca. 4.3 eV can easily transfer to natural F_6TCNNQ with a LUMO of ca. 5.6 eV. As shown in the red curves of 1 Å F_6TCNNQ/defective ML-WS_2/sapphire in **Figure 5.34**, two features (marked "A" with BE of 0.16 eV and "B" with BE of 0.78 eV) are observed. According to the previous report [218], these electronic states can be assigned to anionic F_6TCNNQ (F_6TCNNQ^-), resulting from the CT process between defective ML-WS_2 and the neutral molecules. This assignment is further confirmed by density functional theory calculations (DFT) and two new molecular states consisting in a combination of (i) the former HOMO level and the singly filled former LUMO level (peak A) and (ii) the former HOMO and HOMO-1 levels

(peak B) are verified. These two anionic molecular states are named as LUMO* and HOMO* [218].

5.4.3 Interfacial energy level diagrams

With a series of ARUPS measurements of F_6TCNNQ/defective ML-WS_2/sapphire, we now turn towards understand the electronic/optical transition of two systems regarding the energy level diagrams. For pristine ML-WS_2 on sapphire, EA and IE were reported at 3.79 and 6.03 eV with E_F located in the bandgap [200]. Considering the large energy offset between the reported LUMO of F_6TCNNQ (5.6 eV) [271] and IE of pristine ML-WS_2 (6.03 eV), we can rule out the possibility of CT from pristine ML-WS_2 VBM to F_6TCNNQ LUMO, and vacuum level alignment prevails for the system of F_6TCNNQ/pristine ML-WS_2/sapphire, which is consistent with the absorption spectrum of F_6TCNNQ/ML-WS_2/sapphire discussed above.

For defective ML-WS_2 on sapphire, the IE is determined by adding the global VBM onset binding energy to the system Φ ($\mathrm{IE} = \Phi + \mathrm{VBM}$), resulting in 6.00 eV. As mentioned above, we observe a filling of conduction band minimum at Q-point just below the E_F (4.28 eV), thus, the corresponding EA is estimated at ca 4.3 eV. After depositing F_6TCNNQ on defective ML-WS_2, electrons from defective ML-WS_2 CBM (ca. 4.3 eV) can easily transfer to the LUMO of F_6TCNNQ (ca. 5.6 eV). After the charge transfer, the IE of ML-WS_2 is determined by adding the VBM onset binding energy to the sample Φ, yielding 6.47 eV. The electron density on the ML-WS_2 surface is greatly reduced due to the CT process, thus, the band structure renormalization is healed in a certain range. Estimated EA is obtained by subtracting the reported bandgap of 2.24 eV [219], resulting in ca. 4.23 eV. Two new electronic states assigned to the anionic F_6TCNNQ are located ca. 0.16 and 0.78 eV below the E_F according to the onset of peak A and B in **Figure 5.35**. We can herein determine the "IE" of these two gap states at ca. 5.51 (anionic F_6TCNNQ LUMO*), and 6.13 eV (anionic F_6TCNNQ HOMO*) respectively. The electronic transition from LUMO* of anionic F_6TCNNQ to CBM of WS_2 is ca. 1.3 eV, which is even much lower than the optical transition of 1.53 eV assigned to peak D in **Figure 5.30** (b), indicating peak D is not related to such transition since the electronic bandgap is at higher energy than the optical bandgap [electronic bandgap (E_g)=optical bandgap (E_{opt}) +exciton binding energy]. While the electronic bandgap between F_6TCNNQ HOMO* and ML-WS_2 CBM is ca 1.9 eV, the corresponding E_{opt} is estimated by subtracting the exciton binding

energy, normally around 500 meV for the hybrid inorganic/organic semiconductor system, yield 1.4-1.5 eV which is close to the peak D. Hence, Peak D could be likely attributed to the transition from anionic F_6TCNNQ $HOMO^*$ state to WS_2 CBM after the charge transfer.

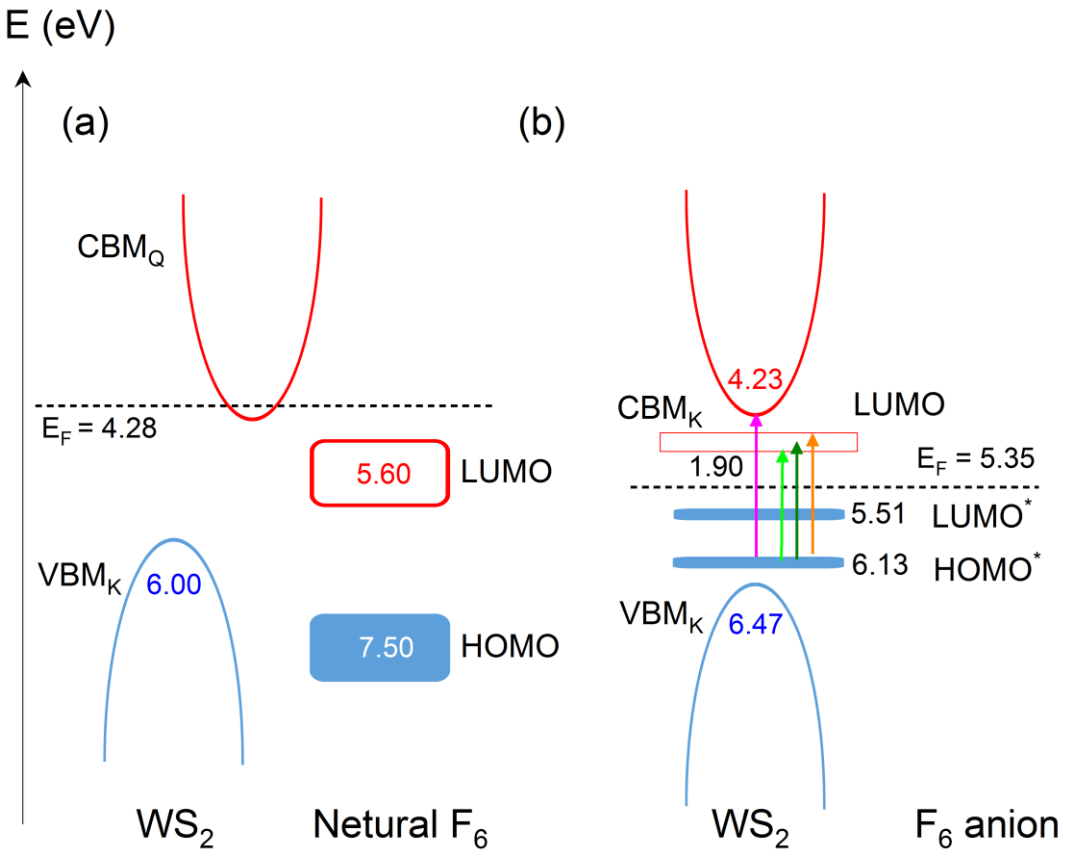

Figure 5.35 *Schematic energy level diagrams for (a) defective ML-WS_2/sapphire and neutral F_6TCNNQ (b) F_6TCNNQ/defective ML-WS_2/sapphire. The blue and red depict the occupied and unoccupied levels, respectively. All values are in unit of eV, and states are with respect to the vacuum level, set to zero. The arrows in (b) refer to the optical interfacial transitions, and the colors of the arrows are consistent with the fitted peaks in* ***Figure 5.30.***

5.4.4 Conclusion

We investigated the electronic and optical properties of the interface combining a strong p-dopant molecule, F_6TCNNQ adsorbed on ML-WS_2 supported on the sapphire substrate using ARPES and UV-Vis absorption. The absorption spectrum of F_6TCNNQ adsorbed on the defective ML-WS_2 shows a series of peaks that are absent when F_6TCNNQ is deposited on the pristine ML-WS_2 film. The first set of peaks is attributed to the vibronic optoelectronic transition of F_6TCNNQ anions, which indicates the occurrence of ground state interface charge transfer. An additional strong absorption peak was observed at ca. 1.5 eV, which is absent both for F_6TCNNQ adsorbed on the pristine ML-WS_2 and for the

F_6TCNNQ anion alone. By the approximated EBE of ca. 500 meV, this interface absorption peak could be further attributed to a hybrid molecule-to-TMDC electronic transition from anionic F_6TCNNQ HOMO* state to defective ML-WS_2 CBM by ARPES measurements.

6 Summary and outlook

This thesis explored the electronic and optical properties of ML-TMDCs (ML-MoS_2 and ML-WS_2 in this paper) and their interface with molecular semiconductors. We employed ARPES as the core technique to study the band dispersion and SVs-induced band structure renormalization of ML-TMDCs, providing a solid foundation for a deep insight into the optoelectronic properties of the molecule/ML-TMDCs interfaces. The electronic properties of C_{60}/ML-WS_2 interface supported on different substrates were investigated by ARUPS and XPS. The electronic and optical properties of an interface combining a strong p-dopant molecule, F_6TCNNQ adsorbed on a ML-WS_2 supported on a sapphire substrate were investigated using ARPES and UV-Vis absorption. In addition, information on optical, structural, and morphological properties of ML-TMDCs systems were obtained by combining PL, Raman shift, UV-vis absorption, TEM, and AFM measurements.

With a set of experiments, we characterized the surface morphology and optical properties of measured TMDCs samples, demonstrating them as monolayers with high quality and homogeneity. The energy distribution curves (EDCs) of ML-TMDCs measured at different take-off angles indicate that the valence band exhibits the energy versus momentum $E(\boldsymbol{k})$ dispersion expected for ML-TMDC films consisting of azimuthally randomly orientated flakes, that is, due to angular averaging the photoelectron spectra consist of a linear superposition of the electronic bands along the Γ-K and Γ-M directions [218, 226]. The VBM observed at K-point instead of Γ-point indicates the measured ML samples consisting of a monolayer on a macroscopic scale [227], which is consistent with the results obtained with the other characterization techniques.

With a combination of PES and STEM measurements, a high density of SVs (ca. 10^{13} cm^{-2} range), which served as n-dopants, could be generated by annealing ML-TMDCs in UHV. The observation of dispersive bands close to the E_F for ML-TMDCs on the insulating substrate (sapphire) demonstrates the filling of CBM at K- and Q-point, which is attributed to the ionization of electrons from SVs-induced defect states. SVs-induced defect states, which are normally expected to be donor states (several hundred meV below the CBM) limiting thereby transport properties, and the electrons from the states are fully ionized to the CBM. These apparent discrepancies can be reconciled by considering the bandgap increasingly shrunk with increasing carrier density within the CBM, which acts as a positive feedback loop for the ionization of the defect levels, the E_F eventually reaching

the CBM edge. In contrast, no comparable filling of CB was observed on a conductive substrate (HOPG) since the electrons from SVs-induced defect states are primarily ionized towards the substrate charge reservoir instead. Other than SVs, $[RuCp^*(mes)]_2$ was employed to obtain strongly n-dope TMDC monolayers both on sapphire and HOPG. The doping mechanisms are markedly different depending on the conducting properties of the substrate, that is, we identified a direct doping mechanism on sapphire, while on HOPG, TMDC doping is electrostatic in nature and results from charge transfer from $[RuCp^*(mes)]_2$ to HOPG.

Strong band structure renormalization is observed on ML-TMDCs on sapphire, that is, the local CBM at the Q-point moves in energy towards the global CBM at the K-point, and for WS_2 the Q-point even becomes the new global CBM. In contrast, no unambiguous observation of band structure renormalization was found on HOPG. Such band structure renormalization could be attributed to SVs-induced compressive strains [239, 245, 246] and electron density increased following the ionization of electrons from SVs-induced defect states [52], in agreement with DFT calculations. In contrast, for TMDCs supported by HOPG, the absence of band structure renormalization possibly implies the release of stress on HOPG compared to sapphire and an indirect doping mechanism as discussed above. In addition, we demonstrated that passivation/healing of the SVs can be achieved by O_2-exposure at the elevated temperature in vacuum, providing thereby an alternative route to help recover the pristine optoelectronic properties of defective TMDC films.

The results presented in this thesis help contribute to a better understanding of the optoelectronic properties of TMDCs in the presence of high SVs density on vastly different substrates that are widely used in fundamental studies and in device fabrications. The observed substrate-dependent impact of the defects in the DOS spectrum will need to be adequately considered for advanced defect engineering in the view of TMDC-based applications, such as catalysis, optoelectronics, plasmonics, and nanophotonics. Further in-situ optical studies can obtain a detailed understanding of the SVs-induced band structure renormalization process, for instance, in-situ PL measurements will be employed to verify the direct-to-indirect bandgap transition when going from pristine to defective ML-WS_2. Also, the in-situ PL of O_2-exposure to defective ML-WS_2 could help us track the evolution of the band structure, from strongly renormalized for defective ML-TMDCs to possibly weakly renormalized upon defect passivation, which could help clarify the observation of direct bandgap for both pristine and defective ML-TMDCs in air.

Furthermore, the electronic properties of a prototypical heterostructure formed by C_{60} and ML-WS_2, on two different supporting substrates were investigated. No indication of ground-state charge transfer upon interface formation is found on both substrates, that is, vacuum level alignment prevails. Since a large amount of SVs needed to be induced for the purpose of ARPES measurements but do not necessarily need to be present (at least in such proportion) in actual devices, we ignored the effect of SVs-induced band renormalization and proposed the interfacial energy diagram of C_{60}/"perfect" ML-WS_2 on both substrates. The energy offsets between the occupied and unoccupied frontier electronic levels of C_{60} and ML-WS_2 were estimated to be almost identical for both substrates. Overall, the C_{60}/"perfect" ML-WS_2 interface is characterized by a type-II level alignment, with C_{60} acting as an electron acceptor, which makes this heterostructure interesting for further investigations in photo-responsive device structures. However, the energy level offset between the global CBM of ML-WS_2 and the C_{60} LUMO is virtually equal to the exciton binding energy of the inorganic ML, thus efficient electron transfer after optical excitation may only occur for excitation energies higher than the ML-WS_2 fundamental exciton.

Finally, we investigated the optoelectronic properties of an interface combining a strong p-dopant molecule, F_6TCNNQ, adsorbed on a ML-WS_2 supported on the sapphire substrate using ARPES and UV-Vis absorption. The absorption spectrum of F_6TCNNQ adsorbed on the defective ML-WS_2 shows a series of absorption peaks that are absent when F_6TCNNQ is deposited on the pristine ML-WS_2 film. The first set of peaks is attributed to the optical transition of the F_6TCNNQ anions and the associated vibrionic transitions, which indicates the occurrence of ground state interface charge transfer, further verified by ARPES. CT resulted in the occurrence of two characteristic anionic molecular states (named as anionic F_6TCNNQ LUMO* and HOMO*) in the bandgap with BE of ca. 0.16 and 0.78 eV with respect to the E_F, respectively. The additional strong absorption peak at ca. 1.53 eV is observed between that of ML-WS_2 and the F_6TCNNQ anions, which is absent both for F_6TCNNQ adsorbed on the pristine ML-WS_2 and for the F_6TCNNQ anion alone. This interface absorption peak could be attributed to a hybrid molecule-to-TMDC electronic transition from the anionic F_6TCNNQ HOMO* to ML-WS_2 CBM. These results demonstrate that defects impact not only the optoelectronic properties of the monolayers but also their related interfaces with organic semiconductors. Further optical studies on ML-TMDCs combined with other molecules are still needed to achieve a better understanding of the interfacial optoelectronic properties on the organic TMDCs interfaces,

for instance, designed type-II band alignment of C_{60}/ML-TMDCs and strongly n-dopant/ML-TMDCs.

The results of this work help contribute to a better understanding of the electronic properties of ML-TMDCs and their interfaces with molecular semiconductors. It stresses the importance of SVs impact both on the optoelectronic properties of the ML-TMDCs and their interface with other molecular semiconductors. The effect of the supporting substrate is taken into consideration for SVs study and energy level alignment of molecule/ML-WS_2 as well. However, to the best of our best knowledge, it is the first time that a band renormalization process is proposed in defective ML-TMDC, that is, electrons from SVs-induced defect states are ionized to CBM of ML-TMDCs instead of the occurrence of localized defect states within the bandgap. Although it is in great agreement with the PES results, theoretical calculations and other experimental characterization still remain to be performed to verify the occurrence of band structure renormalization in defective ML-TMDCs and help to better understand the optoelectronic properties of the MSC/ML-TMDC interface.

7 Bibliography

[1] K. F. Mak, J. Shan, *Photonics and optoelectronics of 2D semiconductor transition metal dichalcogenides*. Nat. Photonics **2016**, *10*, 216.

[2] Z. Sun, A. Martinez, F. Wang, *Optical modulators with 2D layered materials*. Nat. Photonics **2016**, *10*, 227.

[3] M. Osada, T. Sasaki, *Two-dimensional dielectric nanosheets: novel nanoelectronics from nanocrystal building blocks*. Adv. Mater. **2012**, *24*, 210.

[4] M. S. Choi, G. H. Lee, Y. J. Yu, D. Y. Lee, S. H. Lee, P. Kim, J. Hone, W. J. Yoo, *Controlled charge trapping by molybdenum disulphide and graphene in ultrathin heterostructured memory devices*. Nat. Commun. **2013**, *4*, 1624.

[5] B. Radisavljevic, A. Radenovic, J. Brivio, V. Giacometti, A. Kis, *Single-layer MoS_2 transistors*. Nat. Nanotechnol. **2011**, *6*, 147.

[6] D. J. Late, Y. K. Huang, B. Liu, J. Acharya, S. N. Shirodkar, J. Luo, A. Yan, D. Charles, U. V. Waghmare, V. P. Dravid, *Sensing behavior of atomically thin-layered MoS_2 transistors*. ACS Nano **2013**, *7*, 4879.

[7] Z. Yin, H. Li, H. Li, L. Jiang, Y. Shi, Y. Sun, G. Lu, Q. Zhang, X. Chen, H. Zhang, *Single-layer MoS_2 phototransistors*. ACS Nano **2012**, *6*, 74.

[8] M. Bernardi, M. Palummo, J. C. Grossman, *Extraordinary sunlight absorption and one nanometer thick photovoltaics using two-dimensional monolayer materials*. Nano Lett. **2013**, *13*, 3664.

[9] A. K. Geim, *Graphene: status and prospects*. Science **2009**, *324*, 1530.

[10] S. J. McDonnell, R. M. Wallace, *Atomically-thin layered films for device applications based upon 2D TMDC materials*. Thin Solid Films **2016**, *616*, 482.

[11] Q. H. Wang, K. Kalantar-Zadeh, A. Kis, J. N. Coleman, M. S. Strano, *Electronics and optoelectronics of two-dimensional transition metal dichalcogenides*. Nat. Nanotechnol. **2012**, *7*, 699.

[12] G. Fiori, F. Bonaccorso, G. Iannaccone, T. Palacios, D. Neumaier, A. Seabaugh, S. K. Banerjee, L. Colombo, *Electronics based on two-dimensional materials*. Nat. Nanotechnol. **2014**, *9*, 768.

[13] F. Koppens, T. Mueller, P. Avouris, A. Ferrari, M. Vitiello, M. Polini, *Photodetectors based on graphene, other two-dimensional materials and hybrid systems*. Nat. Nanotechnol. **2014**, *9*, 780.

[14] Y. Ma, Y. Dai, M. Guo, C. Niu, J. Lu, B. Huang, *Electronic and magnetic properties of perfect, vacancy-doped, and nonmetal adsorbed $MoSe_2$, $MoTe_2$ and WS_2 monolayers*. Phys. Chem. Chem. Phys. **2011**, *13*, 15546.

[15] H. Zhang, L. M. Liu, W. M. Lau, *Dimension-dependent phase transition and magnetic properties of VS_2*. J. Mater. Chem. A **2013**, *1*, 10821.

[16] Y. Ye, J. Xiao, H. Wang, Z. Ye, H. Zhu, M. Zhao, Y. Wang, J. Zhao, X. Yin, X. Zhang, *Electrical generation and control of the valley carriers in a monolayer transition metal dichalcogenide*. Nat. Nanotechnol. **2016**, *11*, 598.

[17] K. F. Mak, C. Lee, J. Hone, J. Shan, T. F. Heinz, *Atomically thin MoS_2: a new direct-gap semiconductor*. Phys. Rev. Lett. **2010**, *105*, 136805.

[18] W. S. Yun, S. Han, S. C. Hong, I. G. Kim, J. Lee, *Thickness and strain effects on electronic structures of transition metal dichalcogenides: 2H-MX_2 semiconductors (M= Mo, W; X= S, Se, Te)*. Phys. Rev. B **2012**, *85*, 033305.

[19] B. Zhu, X. Chen, X. Cui, *Exciton binding energy of monolayer WS_2*. Sci. Rep. **2015**, *5*, 9218.

[20] H. Tian, M. L. Chin, S. Najmaei, Q. S. Guo, F. N. Xia, H. Wang, M. Dubey, *Optoelectronic devices based on two-dimensional transition metal dichalcogenides*. Nano Res. **2016**, 9, 1543.

[21] S. Mukherjee, R. Maiti, A. K. Katiyar, S. Das, S. K. Ray, *Novel colloidal MoS_2 quantum dot heterojunctions on silicon platforms for multifunctional optoelectronic devices*. Sci. Rep. **2016**, *6*, 29016.

[22] D. J. Late, B. Liu, H. R. Matte, V. P. Dravid, C. N. R. Rao, *Hysteresis in single-layer MoS_2 field effect transistors*. ACS Nano **2012**, *6*, 5635.

[23] Y. J. Kwack, T. T. T. Can, W.-S. Choi, *Bottom-up water-based solution synthesis for a large MoS_2 atomic layer for thin-film transistor applications*. Npj 2D Mater. Appl. **2021**, *5*, 84.

[24] G. W. Baek, S. G. Seo, D. Hahm, W. K. Bae, J. Kwak, S. H. Jin, *Highly efficient, surface ligand modified quantum dot light-emitting diodes driven by type-controllable $MoTe_2$ thin film transistors via electron charge enhancer*. Adv. Electron. Mater. **2021**, *7*, 2100535.

[25] T. A. Shastry, I. Balla, H. Bergeron, S. H. Amsterdam, T. J. Marks, M. C. Hersam, *Mutual photoluminescence quenching and photovoltaic effect in large-area single-layer MoS_2-polymer heterojunctions*. ACS Nano **2016**, *10*, 10573.

[26] S. Roy, Z. Hu, S. Kais, P. Bermel, *Enhancement of phtovoltaic current through dark states in donor-acceptor pairs of tungsten-based transition metal di-chalcogenides*. Adv. Funct. Mater. **2021**, *31*, 2100387.

[27] S. K. Zhang, X. D. Wang, Y. Chen, G. J. Wu, Y. C. Tang, L. Q. Zhu, H. L. Wang, W. Jiang, L. X. Sun, T. Lin, H. Shen, W. D. Hu, J. Ge, J. L. Wang, X. J. Meng, J. H. Chu, *Ultrasensitive hybrid MoS_2-ZnCdSe quantum dot photodetectors with high gain*. ACS Appl. Mater. Interfaces **2019**, *11*, 23667.

[28] J. F. G. Marin, D. Unuchek, K. Watanabe, T. Taniguchi, A. Kis, *MoS_2 photodetectors integrated with photonic circuits*. Npj 2D Mater. Appl. **2019**, *3*, 14.

[29] D. Jariwala, T. J. Marks, M. C. Hersam, *Mixed-dimensional van der Waals heterostructures*. Nat. Mater. **2017**, *16*, 170.

[30] D. Jariwala, S. L. Howell, K. S. Chen, J. M. Kang, V. K. Sangwan, S. A. Filippone, R. Turrisi, T. J. Marks, L. J. Lauhon, M. C. Hersam, *Hybrid, gate-tunable, van der Waals p–n heterojunctions from pentacene and MoS_2.* Nano Lett. **2016**, *16*, 497.

[31] N. Mutz, S. Park, T. Schultz, S. Sadofev, S. Dalgleish, L. Reissig, N. Koch, E. J. List-Kratochvil, S. Blumstengel, *Excited-state charge transfer enabling MoS_2/phthalocyanine photodetectors with extended spectral sensitivity*. J. Phys. Chem. C **2020**, *124*, 2837.

[32] F. C. Liu, W. L. Chow, X. X. He, P. Hu, S. J. Zheng, X. L. Wang, J. D. Zhou, Q. D. Fu, W. Fu, P. Yu, Q. S. Zeng, H. J. Fan, B. K. Tay, C. Kloc, Z. Liu, *Van der Waals p–n junction based on an organic–inorganic heterostructure*. Adv. Funct. Mater. **2015**, *25*, 5865.

[33] M. Gobbi, E. Orgiu, P. Samorì, *When 2D materials meet molecules: opportunities and challenges of hybrid organic/inorganic van der Waals heterostructures*. Adv. Mater. **2018**, *30*, 1706103.

[34] J. K. Kim, K. Cho, T. Y. Kim, J. Pak, J. Jang, Y. Song, Y. Kim, B. Y. Choi, S. Chung, W. K. Hong, T. Lee, *Trap-mediated electronic transport properties of gate-tunable pentacene/MoS_2 pn heterojunction diodes*. Sci. Rep. **2016**, *6*, 36775.

[35] X. Li, F. Zhang, Q. Niu, *Unconventional quantum Hall effect and tunable spin Hall effect in Dirac materials: application to an isolated MoS_2 trilayer*. Phys. Rev. Lett. **2013**, *110*, 066803.

[36] F. Parhizgar, H. Rostami, R. Asgari, *Indirect exchange interaction between magnetic adatoms in monolayer MoS_2.* Phys. Rev. B **2013**, *87*, 125401.

[37] T. Björkman, A. Gulans, A. V. Krasheninnikov, R. M. Nieminen, *van der Waals bonding in layered compounds from advanced density-functional first-principles calculations*. Phys. Rev. Lett. **2012**, *108*, 235502.

[38] G. B. Liu, W. Y. Shan, Y. G. Yao, W. Yao, D. Xiao, *Three-band tight-binding model for monolayers of group-VIB transition metal dichalcogenides*. Phys. Rev. B **2013**, *88*, 085433.

[39] A. Splendiani, L. Sun, Y. B. Zhang, T. S. Li, J. Kim, C. Y. Chim, G. Galli, F. Wang, *Emerging photoluminescence in monolayer MoS_2.* Nano Lett. **2010**, *10*, 1271.

[40] A. Kuc, N. Zibouche, T. Heine, *Influence of quantum confinement on the electronic structure of the transition metal sulfide TS_2*. Phys. Rev. B **2011**, *83*, 245213.

[41] H. S. S. R. Matte, A. Gomathi, A. K. Manna, D. J. Late, R. Datta, S. K. Pati, C. N. R. Rao, *MoS_2 and WS_2 analogues of graphene*. Angew. Chem. Int. Ed. **2010**, *49*, 4059.

[42] S. Lebegue, O. Eriksson, *Electronic structure of two-dimensional crystals from ab initio theory*. Phys. Rev. B **2009**, *79*, 115409.

[43] T. S. Li, G. Galli, *Electronic properties of MoS_2 nanoparticles*. J. Phys. Chem. C **2007**, *111*, 16192.

[44] S. Haldar, H. Vovusha, M. K. Yadav, O. Eriksson, B. Sanyal, *Systematic study of structural, electronic, and optical properties of atomic-scale defects in the two-dimensional transition metal dichalcogenides MX_2 (M=Mo, W; X=S, Se, Te)*. Phys. Rev. B **2015**, *92*, 235408.

[45] J. Y. Noh, H. Kim, Y. S. Kim, *Stability and electronic structures of native defects in single-layer MoS_2.* Phys. Rev. B **2014**, *89*, 205417.

[46] Z. Lin, B. R. Carvalho, E. Kahn, R. T. Lv, R. Rao, H. Terrones, M. A. Pimenta, M. Terrones, *Defect engineering of two-dimensional transition metal dichalcogenides*. 2D Mater. **2016**, *3*, 022002.

[47] J. H. Hong, C. H. Jin, J. Yuan, Z. Zhang, *Atomic defects in two-dimensional materials: From single-atom spectroscopy to functionalities in opto-/electronics, nanomagnetism, and catalysis*. Adv. Mater. **2017**, *29*, 1606434.

[48] A. Raja, A. Chaves, J. Yu, G. Arefe, H. M. Hill, A. F. Rigosi, T. C. Berkelbach, P. Nagler, C. Schüller, T. Korn, C. Nuckolls, J. Hone, L. E. Brus, T. F. Heinz, D. R. Reichman, A. Chernikov, *Coulomb engineering of the bandgap and excitons in two-dimensional materials*. Nat. Commun. **2017**, *8*, 15251.

[49] M. Florian, M. Hartmann, A. Steinhoff, J. Klein, A. W. Holleitner, J. J. Finley, T. O. Wehling, M. Kaniber, C. Gies, *The dielectric impact of layer distances on exciton and trion binding energies in van der Waals heterostructures*. Nano Lett. **2018**, *18*, 2725.

[50] M. Drüppel, T. Deilmann, P. Krüger, M. Rohlfing, *Diversity of trion states and substrate effects in the optical properties of an MoS_2 monolayer*. Nat. Commun. **2017**, *8*, 2117.

[51] B. Amin, T. P. Kaloni, U. Schwingenschlögl, *Strain engineering of WS_2, WSe_2, and WTe_2*. RSC Adv. **2014**, *4*, 34561.

[52] D. Erben, A. Steinhoff, C. Gies, G. Schönhoff, T. Wehling, F. Jahnke, *Excitation-induced transition to indirect band gaps in atomically thin transition-metal dichalcogenide semiconductors*. *Phys. Rev. B* **2018**, *98*, 035434.

[53] P. Hofmann, *Solid state physics: an introduction*. Wiley-VCH, **2015**.

[54] J. M. Ziman, *Principles of the theory of solids*. Cambridge university press, **1972**.

[55] C. Kittel, P. McEuen, *Kittel's introduction to solid state physics*. Wiley-VCH, **2018**.

[56] H. Ibach, H. Lüth, *Solid-state physics: an introduction to principles of materials science*. Springer Berlin Heidelberg, **200**9.

[57] N. W. Ashcroft, N. D. Mermin, *Solid state physics*. Cengage Learning, **2011**.

[58] D. W. Snoke, *Solid state physics: essential concepts*. Addison-Wesley, **2009**.

[59] M. Oehzelt, K. Akaike, N. Koch, G. Heimel, *Energy-level alignment at organic heterointerfaces*. Sci. Adv. **2015**, *1*, e1501127.

[60] M. Oehzelt, N. Koch, G. Heimel, *Organic semiconductor density of states controls the energy level alignment at electrode interfaces*. Nat. Commun. **2014**, *5*, 4174.

[61] W. Mönch, *Semiconductor surfaces and interfaces*. Springer Science & Business Media, **2013**.

[62] P. P. Altermatt, A. Schenk, F. Geelhaar, G. Heiser, *Reassessment of the intrinsic carrier density in crystalline silicon in view of band-gap narrowing*. J. Appl. Phys. **2003**, *93*, 1598.

[63] M. Grundmann, *The physics of semiconductors: an introduction including devices and nanophysics and applications*. Springer Berlin Heidelberg, **2016**.

[64] P. Erhart, A. Klein, K. Albe, *First-principles study of the structure and stability of oxygen defects in zinc oxide*. Phys. Rev. B **2005**, *72*, 085213.

[65] H. B. Fan, S. Y. Yang, P. F. Zhang, H. Y. Wei, X. L. Liu, C. M. Jiao, Q. S. Zhu, Y. H. Chen, Z. G. Wang, *Investigation of oxygen vacancy and interstitial oxygen defects in*

ZnO films by photoluminescence and X-ray photoelectron spectroscopy. Chin. Phys. Lett. **2007**, *24*, 2108.

[66] M. X. Liu, J. P. Shi, Y. C. Li, X. B. Zhou, D. L. Ma, Y. Qi, Y. F. Zhang, Z. F. Liu, *Temperature-triggered sulfur vacancy evolution in monolayer MoS_2/graphene heterostructures*. Small **2017**, *13*, 1602967.

[67] S. Lee, G. Kim, H. Kim, B. Y. Choi, J. Lee, B. W. Jeong, J. Ihm, Y. Kuk, S. J. Kahng, *Paired gap states in a semiconducting carbon nanotube: deep and shallow levels*. Phys. Rev. Lett. **2005**, *95*, 166402.

[68] Y. F. Liang, L. Yang, *Carrier plasmon induced nonlinear band gap renormalization in two-dimensional semiconductors*. Phys. Rev. Lett. **2015**, *114*, 063001.

[69] H. Haug, S. Schmitt-Rink, *Basic mechanisms of the optical nonlinearities of semiconductors near the band edge*. J. Opt. Soc. Am. B **1985**, *2*, 1135.

[70] Z. Zhang, J. T. Yates, *Band bending in semiconductors: chemical and physical consequences at surfaces and interfaces*. Chem. Rev. **2012**, *112*, 5520.

[71] K. Seeger, *Semiconductor physics*. Springer Science & Business Media, **2013**.

[72] R. Heinhold, G. Williams, S. Cooil, D. Evans, M. Allen, *Influence of polarity and hydroxyl termination on the band bending at ZnO surfaces*. Phys. Rev. B **2013**, *88*, 235315.

[73] T. Schultz, R. Schlesinger, J. Niederhausen, F. Henneberger, S. Sadofev, S. Blumstengel, A. Vollmer, F. Bussolotti, J. P. Yang, S. Kera, K. Parvez, N. Ueno, K. Müllen, N. Koch, *Tuning the work function of GaN with organic molecular acceptors*. Phys. Rev. B **2016**, *93*, 125309.

[74] M. Valtiner, M. Todorova, J. Neugebauer, *Hydrogen adsorption on polar ZnO (0001)-Zn: extending equilibrium surface phase diagrams to kinetically stabilized structures*. Phys. Rev. B **2010**, *82*, 165418.

[75] N. Koch, N. Ueno, A. T. S. Wee, *The molecule-metal interface*. John Wiley & Sons, **2013**.

[76] P. Amsalem, G. Heimel, N. Koch, *Experimental investigation on charge transfer between organic adsorbates and solid surfaces*. Encycl.Interfacial.Chem. **2018,** pp. 50-67.

[77] Y. Liu, J. Guo, E. B. Zhu, L. Liao, S. J. Lee, M. N. Ding, I. Shakir, V. Gambin, Y. Huang, X. F. Duan, *Approaching the Schottky–Mott limit in van der Waals metal–semiconductor junctions*. Nature **2018**, *557*, 696.

[78] S. Park, T. Schultz, D. Shin, N. Mutz, A. Aljarb, H. S. Kang, C. H. Lee, L. J. Li, X. Xu, V. Tung, E. J. List-Kratochvil, S. Blumstengel, P. Amsalem, N. Koch, *The Schottky–*

Mott rule expanded for two-dimensional semiconductors: influence of substrate dielectric screening. ACS Nano **2021**, *15*, 14794.

[79] S. Braun, W. R. Salaneck, M. Fahlman, *Energy-level alignment at organic/metal and organic/organic interfaces*. Adv. Mater. **2009**, *21*, 1450.

[80] I. G. Hill, A. Rajagopal, A. Kahn, Y. Hu, *Molecular level alignment at organic semiconductor-metal interfaces*. Appl. Phys. Lett. **1998**, *73*, 662.

[81] A. Kahn, N. Koch, W. Y. Gao, *Electronic structure and electrical properties of interfaces between metals and π-conjugated molecular films*. J. Polym. Sci. B: Polym. Phys. **2003**, *41*, 2529.

[82] N. Koch, *Organic electronic devices and their functional interfaces*. ChemPhysChem **2007**, *8*, 1438.

[83] S. Winkler, J. Frisch, P. Amsalem, S. Krause, M. Timpel, M. Stolte, F. Würthner, N. Koch, *Impact of molecular dipole moments on fermi level pinning in thin films*. J. Phys. Chem. C **2014**, *118*, 11731.

[84] H. Peisert, A. Petr, L. Dunsch, T. Chassé, M. Knupfer, *Interface fermi level pinning at contacts between PEDOT: PSS and molecular organic semiconductors*. ChemPhysChem **2007**, *8*, 386.

[85] J. Hwang, E. G. Kim, J. Liu, J. L. Bredas, A. Duggal, A. Kahn, *Photoelectron spectroscopic study of the electronic band structure of polyfluorene and fluorene-arylamine copolymers at interfaces*. J. Phys. Chem. C **2007**, *111*, 1378.

[86] S. Braun, W. R. Salaneck, *Fermi level pinning at interfaces with tetrafluorotetracyanoquinodimethane (F4-TCNQ): the role of integer charge transfer states*. Chem. Phys. Lett. **2007**, *438*, 259.

[87] S. Braun, M. P. de Jong, W. Osikowicz, W. R. Salaneck, *Influence of the electrode work function on the energy level alignment at organic-organic interfaces*. Appl. Phys. Lett. **2007**, *91*, 202108

[88] K. S. Novoselov, A. K. Geim, S. V. Morozov, D. Jiang, Y. Zhang, S. V. Dubonos, I. V. Grigorieva, A. A. Firsov, *Electric field effect in atomically thin carbon films*. Science **2004**, *306*, 666.

[89] A. A. Balandin, S. Ghosh, W. Z. Bao, I. Calizo, D. Teweldebrhan, F. Miao, C. N. Lau, *Superior thermal conductivity of single-layer graphene*. Nano Lett. **2008**, *8*, 902.

[90] M. Orlita, C. Faugeras, P. Plochocka, P. Neugebauer, G. Martinez, D. K. Maude, A. L. Barra, M. Sprinkle, C. Berger, W. A. de Heer, M. Potemski, *Approaching the Dirac point in high-mobility multilayer epitaxial graphene*. Phys. Rev. Lett. **2008**, *101*, 267601.

[91] D. Akinwande, N. Petrone, J. Hone, *Two-dimensional flexible nanoelectronics*. Nat. Commun. **2014**, *5*, 5678.

[92] X. Huang, C. L. Tan, Z. Y. Yin, H. Zhang, *25th anniversary article: hybrid nanostructures based on two-dimensional nanomaterials*. Adv. Mater. **2014**, *26*, 2185.

[93] H. Wang, H. B. Feng, J. H. Li, *Graphene and graphene-like layered transition metal dichalcogenides in energy conversion and storage*. Small **2014**, *10*, 2165.

[94] S. J. Kim, K. Choi, B. Lee, Y. Kim, B. H. Hong, *Materials for flexible, stretchable electronics: graphene and 2D materials*. Annu. Rev. Mater. Res. **2015**, *45*, 63.

[95] L. Liu, Y. P. Feng, Z. X. Shen, *Structural and electronic properties of h-BN*. Phys. Rev. B **2003**, *68*, 104102.

[96] J. Eichler, C. Lesniak, *Boron nitride (BN) and BN composites for high-temperature applications*. J. Eur. Ceram. Soc. **2008**, *28*, 1105.

[97] W. Choi, I. Lahiri, R. Seelaboyina, Y. S. Kang, *Synthesis of graphene and its applications: a review*. Crit. Rev. Solid State Mater. Sci. **2010**, *35*, 52.

[98] A. Olabi, M. A. Abdelkareem, T. Wilberforce, E. T. Sayed, *Application of graphene in energy storage device-A review*. Renew. Sust. Energ. Rev. **2021**, *135*, 110026.

[99] K. L. Zhang, Y. Feng, F. Wang, Z. Yang, J. Wang, *Two dimensional hexagonal boron nitride (2D-hBN): synthesis, properties and applications*. J. Mater. Chem. C **2017**, *5*, 11992.

[100] H. N. Li, Y. M. Shi, M. H. Chiu, L. J. Li, *Emerging energy applications of two-dimensional layered transition metal dichalcogenides*. Nano Energy **2015**, *18*, 293.

[101] M. Chhowalla, H. S. Shin, G. Eda, L. J. Li, K. P. Loh, H. Zhang, *The chemistry of two-dimensional layered transition metal dichalcogenide nanosheets*. Nat. Chem. **2013**, *5*, 263.

[102] J. Brivio, D. T. Alexander, A. Kis, *Ripples and layers in ultrathin MoS_2 membranes*. Nano Lett. **2011**, *11*, 5148.

[103] A. V. Kolobov, J. Tominaga, *Two-dimensional transition-metal dichalcogenides*. Springer, **2016**.

[104] D. Çakır, F. M. Peeters, C. Sevik, *Mechanical and thermal properties of h-MX_2 (M=Cr, Mo, W; X=O, S, Se, Te) monolayers: a comparative study*. Appl. Phys. Lett. **2014**, *104*, 203110.

[105] J. Wilson, A. Yoffe, *The transition metal dichalcogenides discussion and interpretation of the observed optical, electrical and structural properties.* Adv. Phys. **1969**, *18*, 193.

[106] H. Katzke, P. Tolédano, W. Depmeier, *Phase transitions between polytypes and intralayer superstructures in transition metal dichalcogenides.* Phys. Rev. B **2004**, *69*, 134111.

[107] H. L. Zeng, G. B. Liu, J. F. Dai, Y. J. Yan, B. R. Zhu, R. C. He, L. Xie, S. J. Xu, X. H. Chen, W. Yao, X. D. Cui, *Optical signature of symmetry variations and spin-valley coupling in atomically thin tungsten dichalcogenides*. Sci. Rep. **2013**, *3*, 1608.

[108] J. A. Wilson, A. Yoffe, *The transition metal dichalcogenides discussion and interpretation of the observed optical, electrical and structural properties*. Adv. Phys. **1969**, *18*, 193.

[109] A. Ramasubramaniam, *Large excitonic effects in monolayers of molybdenum and tungsten dichalcogenides*. Phys. Rev. B **2012**, *86*, 115409.

[110] R. Roldán, J. A. Silva-Guillén, M. P. López-Sancho, F. Guinea, E. Cappelluti, P. Ordejón, *Electronic properties of single-layer and multilayer transition metal dichalcogenides MX_2 (M= Mo, W and X= S, Se)*. Ann. Phys. **2014**, *526*, 347.

[111] C. Ruppert, O. B. Aslan, T. F. Heinz, *Optical properties and band gap of single- and few-layer $MoTe_2$ crystals*. Nano Lett. **2014**, *14*, 6231.

[112] Y. You, X. X. Zhang, T. C. Berkelbach, M. S. Hybertsen, D. R. Reichman, T. F. Heinz, *Observation of biexcitons in monolayer WSe_2*. Nat. Phys. **2015**, *11*, 477.

[113] Y. Li, A. Chernikov, X. Zhang, A. Rigosi, H. M. Hill, A. M. Van Der Zande, D. A. Chenet, E. M. Shih, J. Hone, T. F. Heinz, *Measurement of the optical dielectric function of monolayer transition-metal dichalcogenides: MoS_2, $MoSe_2$, WS_2, and WSe_2.* Phys. Rev. B **2014**, *90*, 205422.

[114] C. Lee, H. Yan, L. E. Brus, T. F. Heinz, J. Hone, S. Ryu, *Anomalous lattice vibrations of single-and few-layer MoS_2.* ACS Nano **2010**, *4*, 2695.

[115] H. R. Gutiérrez, N. Perea-López, A. L. Elías, A. Berkdemir, B. Wang, R. Lv, F. López-Urías, V. H. Crespi, H. Terrones, M. Terrones, *Extraordinary room-temperature photoluminescence in triangular WS_2 monolayers*. Nano Lett. **2013**, *13*, 3447.

[116] S. Tongay, J. Zhou, C. Ataca, K. Lo, T. S. Matthews, J. Li, J. C. Grossman, J. Wu, *Thermally driven crossover from indirect toward direct bandgap in 2D semiconductors: $MoSe_2$ versus MoS_2.* Nano Lett. **2012**, *12*, 5576.

[117] W. Zhao, Z. Ghorannevis, K. K. Amara, J. R. Pang, M. Toh, X. Zhang, C. Kloc, P. H. Tan, G. Eda, *Lattice dynamics in mono-and few-layer sheets of WS_2 and WSe_2*. Nanoscale **2013**, *5*, 9677.

[118] G. Lucovsky, R. White, J. Benda, J. Revelli, *Infrared-reflectance spectra of layered group-IV and group-VI transition-metal dichalcogenides*. Phys. Rev. B **1973**, *7*, 3859.

[119] P. Bertrand, *Surface-phonon dispersion of MoS_2.* Phys. Rev. B **1991**, *44*, 5745.

[120] A. Molina-Sanchez, L. Wirtz, *Phonons in single-layer and few-layer MoS_2 and WS_2*. Phys. Rev. B **2011**, *84*, 155413.

[121] P. Tonndorf, R. Schmidt, P. Böttger, X. Zhang, J. Börner, A. Liebig, M. Albrecht, C. Kloc, O. Gordan, D. R. Zahn, S. Michaelis de Vasconcellos, R. Bratschitsch, *Photoluminescence emission and Raman response of monolayer MoS_2, $MoSe_2$, and WSe_2*. Opt. Express **2013**, *21*, 4908.

[122] H. Li, G. Lu, Y. Wang, Z. Yin, C. Cong, Q. He, L. Wang, F. Ding, T. Yu, H. Zhang, *Mechanical exfoliation and characterization of single-and few-layer nanosheets of WSe_2, TaS_2, and $TaSe_2$*. Small **2013**, *9*, 1974.

[123] R. Ganatra, Q. Zhang, *Few-layer MoS_2: a promising layered semiconductor*. ACS Nano **2014**, *8*, 4074.

[124] B. W. Baugher, H. O. Churchill, Y. Yang, P. Jarillo-Herrero, *Intrinsic electronic transport properties of high-quality monolayer and bilayer MoS_2*. Nano Lett. **2013**, *13*, 4212.

[125] M. W. Iqbal, M. Z. Iqbal, M. F. Khan, M. A. Shehzad, Y. Seo, J. H. Park, C. Hwang, J. Eom, *High-mobility and air-stable single-layer WS_2 field-effect transistors sandwiched between chemical vapor deposition-grown hexagonal BN films*. Sci. Rep. **2015**, *5*, 10699.

[126] B. Radisavljevic, A. Kis, *Mobility engineering and a metal-insulator transition in monolayer MoS_2*. Nat. Mater. **2013**, *12*, 815.

[127] S. Kim, A. Konar, W. S. Hwang, J. H. Lee, J. Lee, J. Yang, C. Jung, H. Kim, J. B. Yoo, J. Y. Choi, *High-mobility and low-power thin-film transistors based on multilayer MoS_2 crystals*. Nat. Commun. **2012**, *3*, 1011.

[128] J. Rouxel, R. Brec, *Low-dimensional chalcogenides as secondary cathodic materials: some geometric and electronic aspects*. Annu. Rev. Mater. Sci. **1986**, *16*, 137.

[129] R. Bhandavat, L. David, G. Singh, *Synthesis of surface-functionalized WS_2 nanosheets and performance as Li-ion battery anodes*. J. Phys. Chem. Lett. **2012**, *3*, 1523.

[130] M. A. Ibrahem, T. W. Lan, J. K. Huang, Y. Y. Chen, K. H. Wei, L. J. Li, C. W. Chu, *High quantity and quality few-layers transition metal disulfide nanosheets from wet-milling exfoliation*. RSC Adv. **2013**, *3*, 13193.

[131] M. Shanmugam, C. A. Durcan, B. Yu, *Layered semiconductor molybdenum disulfide nanomembrane based Schottky-barrier solarcells*. Nanoscale **2012**, *4*, 7399.

[132] M. L. Tsai, S. H. Su, J. K. Chang, D. S. Tsai, C. H. Chen, C. I. Wu, L. J. Li, L. J. Chen, J. H. He, *Monolayer MoS_2 heterojunction solar cells*. ACS Nano **2014**, *8*, 8317.

[133] C. C. Wu, D. Jariwala, V. K. Sangwan, T. J. Marks, M. C. Hersam, L. J. Lauhon, *Elucidating the photoresponse of ultrathin MoS_2 field-effect transistors by scanning photocurrent microscopy*. J. Phys. Chem. Lett. **2013**, *4*, 2508.

[134] M. Fontana, T. Deppe, A. K. Boyd, M. Rinzan, A. Y. Liu, M. Paranjape, P. Barbara, *Electron-hole transport and photovoltaic effect in gated MoS_2 Schottky junctions*. Sci. Rep. **2013**, *3*, 1634.

[135] D. Kufer, G. Konstantatos, *Highly sensitive, encapsulated MoS_2 photodetector with gate controllable gain and speed*. Nano Lett. **2015**, *15*, 7307.

[136] E. Rahmanian, R. Malekfar, M. Pumera, *Nanohybrids of two-dimensional transition-metal dichalcogenides and titanium dioxide for photocatalytic applications*. Chem. Eur. J. **2018**, *24*, 18.

[137] C. Sumesh, S. C. Peter, *Two-dimensional semiconductor transition metal based chalcogenide based heterostructures for water splitting applications*. Dalton Trans. **2019**, *48*, 12772.

[138] A. Carladous, R. Coratger, F. Ajustron, G. Seine, R. Péchou, J. Beauvillain, *Light emission from spectral analysis of Au/MoS_2 nanocontacts stimulated by scanning tunneling microscopy*. Phys. Rev. B **2002**, *66*, 045401.

[139] R. Sundaram, M. Engel, A. Lombardo, R. Krupke, A. Ferrari, P. Avouris, M. Steiner, *Electroluminescence in single layer MoS_2*. Nano Lett. **2013**, *13*, 1416.

[140] B. W. Baugher, H. O. Churchill, Y. Yang, P. Jarillo-Herrero, *Optoelectronic devices based on electrically tunable p–n diodes in a monolayer dichalcogenide*. Nat. Nanotechnol. **2014**, *9*, 262.

[141] V. Jankus, P. Data, D. Graves, C. McGuinness, J. Santos, M. R. Bryce, F. B. Dias, A. P. Monkman, *Highly efficient TADF OLEDs: how the emitter-host interaction controls both the excited state species and electrical properties of the devices to achieve near 100% triplet harvesting and high efficiency*. Adv. Funct. Mater. **2014**, *24*, 6178.

[142] Q. Zhang, D. Tsang, H. Kuwabara, Y. Hatae, B. Li, T. Takahashi, S. Y. Lee, T. Yasuda, C. Adachi, *Nearly 100% internal quantum efficiency in undoped electroluminescent devices employing pure organic emitters*. Adv. Mater. **2015**, *27*, 2096.

[143] F. Withers, D. Pozo-Zamudio, A. Mishchenko, A. Rooney, A. Gholinia, K. Watanabe, T. Taniguchi, S. J. Haigh, A. Geim, A. Tartakovskii, *Light-emitting diodes by band-structure engineering in van der Waals heterostructures*. Nat. Mater. **2015**, *14*, 301.

[144] K. S. Novoselov, *Graphene: materials in the flatland (Nobel Lecture)*. Angew. Chem. Int. Ed. **2011**, *50*, 6986.

[145] G. Z. Magda, J. Pető, G. Dobrik, C. Hwang, L. P. Biró, L. Tapasztó, *Exfoliation of large-area transition metal chalcogenide single layers*. Sci. Rep. **2015**, *5*, 14714.

[146] D. M. Tang, D. G. Kvashnin, S. Najmaei, Y. Bando, K. Kimoto, P. Koskinen, P. M. Ajayan, B. I. Yakobson, P. B. Sorokin, J. Lou, D. Golberg, *Nanomechanical cleavage of molybdenum disulphide atomic layers*. Nat. Commun. **2014**, *5*, 3631.

[147] V. Nicolosi, M. Chhowalla, M. G. Kanatzidis, M. S. Strano, J. N. Coleman, *Liquid exfoliation of layered materials*. Science **2013**, *340*, 1226419.

[148] N. Liu, P. Kim, J. H. Kim, J. H. Ye, S. Kim, C. J. Lee, *Large-area atomically thin MoS_2 nanosheets prepared using electrochemical exfoliation*. ACS Nano **2014**, *8*, 6902.

[149] S. G. Valeja, L. Xiu, Z. R. Gregorich, H. Guner, S. Jin, Y. Ge, *Three dimensional liquid chromatography coupling ion exchange chromatography/hydrophobic interaction chromatography/reverse phase chromatography for effective protein separation in top-down proteomics*. Anal. Chem. **2015**, *87*, 5363.

[150] J. N. Coleman, M. Lotya, A. O'Neill, S. D. Bergin, P. J. King, U. Khan, K. Young, A. Gaucher, S. De, R. J. Smith, *Two-dimensional nanosheets produced by liquid exfoliation of layered materials*. Science **2011**, *331*, 568.

[151] M. H. Jeon, C. Ahn, H. Kim, K. N. Kim, T. Z. LiN, H. Qin, Y. Kim, S. Lee, T. Kim, G. Y. Yeom, *Controlled MoS_2 layer etching using CF_4 plasma*. Nanotechnology **2015**, *26*, 355706.

[152] X. Li, W. Cai, J. An, S. Kim, J. Nah, D. Yang, R. Piner, A. Velamakanni, I. Jung, E. Tutuc, *Large-area synthesis of high-quality and uniform graphene films on copper foils*. Science **2009**, *324*, 1312.

[153] Q. Ji, Y. Zhang, Y. Zhang, Z. Liu, *Chemical vapour deposition of group-VIB metal dichalcogenide monolayers: engineered substrates from amorphous to single crystalline*. Chem. Soc. Rev. **2015**, *44*, 2587.

[154] Y. Shi, H. Li, L. J. Li, *Recent advances in controlled synthesis of two-dimensional transition metal dichalcogenides via vapour deposition techniques*. Chem. Soc. Rev. **2015**, *44*, 2744.

[155] M. Bosi, *Growth and synthesis of mono and few-layers transition metal dichalcogenides by vapour techniques: a review*. RSC Adv. **2015**, *5*, 75500.

[156] Y. Rong, Y. Fan, A. L. Koh, A. W. Robertson, K. He, S. Wang, H. Tan, R. Sinclair, J. H. Warner, *Controlling sulphur precursor addition for large single crystal domains of WS_2*. Nanoscale **2014**, *6*, 12096.

[157] S. H. Choi, S. Boandoh, Y. H. Lee, J. S. Lee, J. H. Park, S. M. Kim, W. Yang, K. K. Kim, *Synthesis of large-area tungsten disulfide films on pre-reduced tungsten suboxide substrates*. ACS Appl. Mater. Interfaces **2017**, *9*, 43021.

[158] J. Tao, J. Chai, X. Lu, L. M. Wong, T. I. Wong, J. Pan, Q. Xiong, D. Chi, S. Wang, *Growth of wafer-scale MoS_2 monolayer by magnetron sputtering*. Nanoscale **2015**, *7*, 2497.

[159] D. J. Late, P. A. Shaikh, R. Khare, R. V. Kashid, M. Chaudhary, M. A. More, S. B. Ogale, *Pulsed laser-deposited MoS_2 thin films on W and Si: field emission and photoresponse studies*. ACS Appl. Mater. Interfaces **2014**, *6*, 15881.

[160] J. Kang, D. Shin, S. Bae, B. H. Hong, *Graphene transfer: key for applications*. Nanoscale **2012**, *4*, 5527.

[161] D. M. Guldi, M. Prato, *Excited-state properties of C_{60} fullerene derivatives*. Acc. Chem. Res. **2000**, *33*, 695.

[162] P. W. Blom, V. D. Mihailetchi, L. J. A. Koster, D. E. Markov, *Device physics of polymer: fullerene bulk heterojunction solar cells*. Adv. Mater. **2007**, *19*, 1551.

[163] R. Lof, M. Van Veenendaal, B. Koopmans, H. Jonkman, G. Sawatzky, *Band gap, excitons, and Coulomb interaction in solid C_{60}*. Phys. Rev. Lett. **1992**, *68*, 3924.

[164] H. Yoshida, *Low-energy inverse photoemission study on the electron affinities of fullerene derivatives for organic photovoltaic cells*. J. Phys. Chem. C **2014**, *118*, 24377.

[165] G. Duva, L. Pithan, C. Zeiser, B. Reisz, J. Dieterle, B. Hofferberth, P. Beyer, L. Bogula, A. Opitz, S. Kowarik, *Thin-film texture and optical properties of donor/acceptor complexes. diindenoperylene/F_6TCNNQ vs alpha-sexithiophene/F_6TCNNQ*. J. Phys. Chem. C **2018**, *122*, 18705.

[166] P. K. Koech, A. B. Padmaperuma, L. Wang, J. S. Swensen, E. Polikarpov, J. T. Darsell, J. E. Rainbolt, D. J. Gaspar, *Synthesis and application of 1, 3, 4, 5, 7, 8-hexafluorotetracyanonaphthoquinodimethane (F6-TNAP): a conductivity dopant for organic light-emitting devices*. Chem. Mater. **2010**, *22*, 3926.

[167] S. K. Mohapatra, A. Fonari, C. Risko, K. Yesudas, K. Moudgil, J. H. Delcamp, T. V. Timofeeva, J. L. Brédas, S. R. Marder, S. Barlow, *Dimers of nineteen-electron*

sandwich compounds: crystal and electronic structures, and comparison of reducing strengths. Chem. Eur. J. **2014**, *20*, 15385.

[168] M. R. Deakin, D. A. Buttry, *Electrochemical applications of the quartz crystal microbalance*. Anal. Chem. **1989**, *61*, 1147A.

[169] D. A. Skoog, F. J. Holler, S. R. Crouch, *Principles of instrumental analysis*. Cengage learning, **2017**.

[170] W. Y. Liang, *Excitons*. Phys. Educ. **1970**, *5*, 226.

[171] G. Binnig, C. F. Quate, C. Gerber, *Atomic force microscope*. Phys. Rev. Lett. **1986**, *56*, 930.

[172] G. Haugstad, *Atomic force microscopy: understanding basic modes and advanced applications*. John Wiley & Sons, **2012**.

[173] Heath, J. *Atomic force microscopy for materials*. John Wiley & Sons Ltd, **2017**.

[174] S. Moriguchi, *Compendium of surface and interface analysis*. Springer, **2018**. pp. 331-335.

[175] T. Schultz, *Energy level alignment mechanisms at inorganic-organic semiconductor interfaces investigated with photoelectron spectroscopy*. Humboldt Universitaet zu Berlin (Germany), 2018.

[176] C. Meyer, N. Dellby, J. A. Hachtel, T. Lovejoy, A. Mittelberger, O. Krivanek, *Nion swift: open source image processing software for instrument control, data acquisition, organization, visualization, and analysis using python*. Microsc. Microanal. **2019**, *25(S2)*, 122.

[177] J. C. Crocker, D. G. Grier, *Methods of digital video microscopy for colloidal studies*. J. Colloid Interface Sci. **1996**, *179*, 298.

[178] G. Bradski, *The openCV library*. Dr. Dobb's Journal: Software Tools for the Professional Programmer **2000**, *25*, 120.

[179] C. Nordling, E. Sokolowski, K. Siegbahn, *Precision method for obtaining absolute values of atomic binding energies*. Phys. Rev. **1957**, *105*, 1676.

[180] J. Chastain, R. C. King Jr, *Handbook of X-ray photoelectron spectroscopy*. Perkin-Elmer Corporation **1992**, *40*, 221.

[181] A. Einstein, *Über einem die Erzeugung und Verwandlung des Lichtes betreffenden heuristischen Gesichtspunkt*. Ann. Phys. **1905**, *17*, 132.

[182] A. Kahn, *Fermi level, work function and vacuum level*. Mater. Horiz. **2016**, *3*, 7.

[183] R. Schlaf, *Tutorial on work function*. Tampa: USF Surface Science Laboratory, Dept of Electrical Engineering at University of South Florida **2007**.

[184] T. Schultz, T. Lenz, N. Kotadiya, G. Heimel, G. Glasser, R. Berger, P. W. Blom, P. Amsalem, D. M. de Leeuw, N. Koch, *Reliable work function determination of multicomponent surfaces and interfaces: the role of electrostatic potentials in ultraviolet photoelectron spectroscopy*. Adv. Mater. Interfaces **2017**, *4*, 1700324.

[185] J. Braun, *The theory of angle-resolved ultraviolet photoemission and its applications to ordered materials*. Rep. Prog. Phys. **1996**, *59*, 1267.

[186] A. Damascelli, *Probing the electronic structure of complex systems by ARPES*. Phys. Scr **2004**, *T109*, 61.

[187] S. Hüfner, *Photoelectron spectroscopy: principles and applications*. Springer Science & Business Media, **2013**.

[188] S. Suga, A. Sekiyama, *Photoelectron spectroscopy*. Springer, **2013**.

[189] M. Magnuson, *Electronic structure studies using resonant x-ray and photoemission spectroscopy*. Uppsala University, **1999**.

[190] R. Schlesinger, *Energy-level control at hybrid inorganic/organic semiconductor interfaces*. Springer, **2016**.

[191] R. Schlaf, *Calibration of photoemission spectra and work function determination*. http://rsl. eng. usf. edu/Documents/Tutorials/PEScalibration.pdf.

[192] N. Koch, A. Vollmer, I. Salzmann, B. Nickel, H. Weiss, J. Rabe, *Evidence for temperature-dependent electron band dispersion in pentacene*. Phys. Rev. Lett. **2006**, *96*, 156803.

[193] S. I. Machida, Y. Nakayama, S. Duhm, Q. Xin, A. Funakoshi, N. Ogawa, S. Kera, N. Ueno, H. Ishii, *Highest-occupied-molecular-orbital band dispersion of rubrene single crystals as observed by angle-resolved ultraviolet photoelectron spectroscopy*. Phys. Rev. Lett. **2010**, *104*, 156401.

[194] N. Ueno, S. Kera, *Electron spectroscopy of functional organic thin films: deep insights into valence electronic structure in relation to charge transport property*. Prog. Surf. Sci. **2008**, *83*, 490.

[195] U. Gelius, *Binding energies and chemical shifts in ESCA*. Phys. Scr. **1974**, *9*, 133.

[196] U. Gelius, E. Basilier, S. Svensson, T. Bergmark, K. Siegbahn, *A high resolution ESCA instrument with X-ray monochromator for gases and solids*. J. Electron. Spectrosc. Relat. Phenom. **1973**, *2*, 405.

[197] M. Guittet, J. Crocombette, M. Gautier-Soyer, *Bonding and XPS chemical shifts in $ZrSiO_4$ versus SiO_2 and ZrO_2: charge transfer and electrostatic effects*. Phys. Rev. B **2001**, *63*, 125117.

[198] C. Wagner, L. Davis, M. Zeller, J. Taylor, R. Raymond, L. Gale, *Empirical atomic sensitivity factors for quantitative analysis by electron spectroscopy for chemical analysis*. Surf. Interface Anal. **1981**, *3*, 211.

[199] M. Kazayawoko, J. Balatinecz, R. Sodhi, *X-ray photoelectron spectroscopy of maleated polypropylene treated wood fibers in a high-intensity thermokinetic mixer*. Wood Sci. Technol. **1999**, *33*, 359.

[200] J. Ma, P. Amsalem, T. Schultz, D. Shin, X. Xu, N. Koch, *Energy level alignment at the C_{60}/monolayer-WS_2 interface on insulating and conductive substrates*. Adv. Electron. Mater. **2021**, *7*, 2100425.

[201] F. Caruso, P. Amsalem, J. Ma, A. Aljarb, T. Schultz, M. Zacharias, V. Tung, N. Koch, C. Draxl, *Two-dimensional plasmonic polarons in n-doped monolayer MoS_2*. Phys. Rev. B **2021**, *103*, 205152.

[202] C. Schneider, M. M. Glazov, T. Korn, S. Höfling, B. Urbaszek, *Two-dimensional semiconductors in the regime of strong light-matter coupling*. Nat. Commun. **2018**, *9*, 2695.

[203] T. R. Kafle, B. Kattel, P. Yao, P. Zereshki, H. Zhao, W. L. Chan, *Effect of the interfacial energy landscape on photoinduced charge generation at the ZnPc/MoS_2 interface*. J. Am. Chem. Soc. **2019**, *141*, 11328.

[204] G. Plechinger, P. Nagler, J. Kraus, N. Paradiso, C. Strunk, C. Schüller, T. Korn, *Identification of excitons, trions and biexcitons in single-layer WS_2*. Phys. Status Solidi RRL **2015**, *9*, 457.

[205] S. Mouri, Y. Miyauchi, K. Matsuda, *Tunable photoluminescence of monolayer MoS_2 via chemical doping*. Nano Lett. **2013**, *13*, 5944.

[206] K. Kang, S. Xie, L. Huang, Y. Han, P. Y. Huang, K. F. Mak, C.-J. Kim, D. Muller, J. Park, *High-mobility three-atom-thick semiconducting films with wafer-scale homogeneity*. Nature **2015**, *520*, 656.

[207] H. Yu, M. Liao, W. Zhao, G. Liu, X. Zhou, Z. Wei, X. Xu, K. Liu, Z. Hu, K. Deng, *Wafer-scale growth and transfer of highly-oriented monolayer MoS_2 continuous films*. ACS Nano **2017**, *11*, 12001.

[208] X. Liu, I. Balla, H. Bergeron, M. C. Hersam, *Point defects and grain boundaries in rotationally commensurate MoS_2 on epitaxial graphene*. J. Phys. Chem. C **2016**, *120*, 20798.

[209] B. Schuler, D. Y. Qiu, S. Refaely-Abramson, C. Kastl, C. T. Chen, S. Barja, R. J. Koch, D. F. Ogletree, S. Aloni, A. M. Schwartzberg, J. B. Neaton, S. G. Louie, A. Weber-Bargioni, *Large spin-orbit splitting of deep in-gap defect states of engineered sulfur vacancies in monolayer WS_2*. Phys. Rev. Lett. **2019**, *123*, 076801.

[210] W. Zhou, X. Zou, S. Najmaei, Z. Liu, Y. Shi, J. Kong, J. Lou, P. M. Ajayan, B. I. Yakobson, J. C. Idrobo, *Intrinsic structural defects in monolayer molybdenum disulfide*. Nano Lett. **2013**, *13*, 2615.

[211] D. J. Trainer, Y. Zhang, F. Bobba, X. Xi, S. W. Hla, M. Iavarone, *The effects of atomic-scale strain relaxation on the electronic properties of monolayer MoS_2*. ACS Nano **2019**, *13*, 8284.

[212] P. Vancsó, G. Z. Magda, J. Pető, J. Y. Noh, Y. S. Kim, C. Hwang, L. P. Biró, L. Tapasztó, *The intrinsic defect structure of exfoliated MoS_2 single layers revealed by scanning tunneling microscopy*. Sci. Rep. **2016**, *6*, 29726.

[213] J. Hong, Z. Hu, M. Probert, K. Li, D. Lv, X. Yang, L. Gu, N. Mao, Q. Feng, L. Xie, J. Zhang, D. Wu, Z. Zhang, C. Jin, W. Ji, X. Zhang, J. Yuan, Z. Zhang, *Exploring atomic defects in molybdenum disulphide monolayers*. Nat. Commun. **2015**, *6*, 6239.

[214] H. Qiu, T. Xu, Z. Wang, W. Ren, H. Nan, Z. Ni, Q. Chen, S. Yuan, F. Miao, F. Song, G. Long, Y. Shi, L. Sun, J. Wang, X. Wang, *Hopping transport through defect-induced localized states in molybdenum disulphide*. Nat. Commun. **2013**, *4*, 2642.

[215] I. S. Kim, V. K. Sangwan, D. Jariwala, J. D. Wood, S. Park, K. S. Chen, F. Shi, F. Ruiz-Zepeda, A. Ponce, M. Jose-Yacaman, V. P. Dravid, T. J. Marks, M. C. Hersam, L. J. Lauhon, *Influence of stoichiometry on the optical and electrical properties of chemical vapor deposition derived MoS_2*. ACS Nano **2014**, *8*, 10551.

[216] T. Y. Jeong, H. Kim, S. J. Choi, K. Watanabe, T. Taniguchi, K. J. Yee, Y. S. Kim, S. Jung, *Spectroscopic studies of atomic defects and bandgap renormalization in semiconducting monolayer transition metal dichalcogenides*. Nat. Commun. **2019**, *10*, 3825.

[217] C. Kastl, R. J. Koch, C. T. Chen, J. Eichhorn, S. Ulstrup, A. Bostwick, C. Jozwiak, T. R. Kuykendall, N. J. Borys, F. M. Toma, S. Aloni, A. Weber-Bargioni, E. Rotenberg, A. M. Schwartzberg *Effects of defects on band structure and excitons in WS_2 revealed by nanoscale photoemission spectroscopy*. ACS Nano **2019**, *13*, 1284.

[218] S. Park, T. Schultz, X. Xu, B. Wegner, A. Aljarb, A. Han, L. J. Li, V. C. Tung, P. Amsalem, N. Koch, *Demonstration of the key substrate-dependent charge transfer*

mechanisms between monolayer MoS_2 and molecular dopants. Commun. Phys. **2019**, *2*, 109.

[219] S. Park, N. Mutz, T. Schultz, S. Blumstengel, A. Han, A. Aljarb, L. J. Li, E. J. List-Kratochvil, P. Amsalem, N. Koch, *Direct determination of monolayer MoS_2 and WSe_2 exciton binding energies on insulating and metallic substrates*. 2D Mater. **2018**, *5*, 025003.

[220] P. C. Shen, Y. Lin, C. Su, C. McGahan, A. Y. Lu, X. Ji, X. Wang, H. Wang, N. Mao, Y. Guo, J. H. Park, Y. Wang, W. Tisdale, J. Li, X. Li, K. E. Aidala, T. Palacios, J. Kong, *Healing of donor defect states in monolayer molybdenum disulfide using oxygen-incorporated chemical vapour deposition*. Nat. Electron. **2022**, *5*, 28.

[221] H. Nan, Z. Wang, W. Wang, Z. Liang, Y. Lu, Q. Chen, D. He, P. Tan, F. Miao, X. Wang, *Strong photoluminescence enhancement of MoS_2 through defect engineering and oxygen bonding*. ACS Nano **2014**, *8*, 5738.

[222] R. Dagan, Y. Vaknin, A. Henning, J. Shang, L. Lauhon, Y. Rosenwaks, *Two-dimensional charge carrier distribution in MoS_2 monolayer and multilayers*. Appl. Phys. Lett. **2019**, *114*, 101602.

[223] Y. Zhang, M. M. Ugeda, C. Jin, S.-F. Shi, A. J. Bradley, A. Martín-Recio, H. Ryu, J. Kim, S. Tang, Y. Kim, B. Zhou, C. Hwang, Y. Chen, F Wang, M. F. Crommie, Z. Hussain, Z. X. Shen, S. K. Mo, *Electronic structure, surface doping, and optical response in epitaxial WSe_2 thin films*. Nano Lett. **2016**, *16*, 2485.

[224] P. V. Nguyen, N. C. Teutsch, N. P. Wilson, J. Kahn, X. Xia, A. J. Graham, V. Kandyba, A. Giampietri, A. Barinov, G. C. Constantinescu, N Yeung, N. D M Hine, X. Xu, D. H. Cobden, N. R. Wilson, *Visualizing electrostatic gating effects in two-dimensional heterostructures*. Nature **2019**, *572*, 220.

[225] M. Kang, S. W. Jung, W. J. Shin, Y. Sohn, S. H. Ryu, T. K. Kim, M. Hoesch, K. S. Kim, *Holstein polaron in a valley-degenerate two-dimensional semiconductor*. Nat. Mater. **2018**, *17*, 676.

[226] S. Park, T. Schultz, A. Han, A. Aljarb, X. Xu, P. Beyer, A. Opitz, R. Ovsyannikov, L. J. Li, M. Meissner, T. Yamaguchi, S. Kera, P. Amsalem, N. Koch, *Electronic band dispersion determination in azimuthally disordered transition-metal dichalcogenide monolayers*. Commun. Phys. **2019**, *2*, 68.

[227] W. Jin, P.-C. Yeh, N. Zaki, D. Zhang, J. T. Sadowski, A. Al-Mahboob, A. M. van Der Zande, D. A. Chenet, J. I. Dadap, I. P. Herman, P. Sutter, J. Hone, R. M. Osgood. Jr, *Direct measurement of the thickness-dependent electronic band structure of MoS_2 using angle-resolved photoemission spectroscopy*. Phys. Rev. Lett. **2013**, *111*, 106801.

[228] S. Barja, S. Refaely-Abramson, B. Schuler, D. Y. Qiu, A. Pulkin, S. Wickenburg, H. Ryu, M. M. Ugeda, C. Kastl, C. Chen, C. Hwang, A. Schwartzberg, S. Aloni, S. K. Mo, D. F. Ogletree, M. F. Crommie, O. V. Yazyev, S. G. Louie, *Identifying substitutional oxygen as a prolific point defect in monolayer transition metal dichalcogenides*. Nat. Commun. **2019**, *10*, 3382.

[229] K. Greben, S. Arora, M. G. Harats, K. I. Bolotin, *Intrinsic and extrinsic defect-related excitons in TMDCs*. Nano Lett. **2020**, *20*, 2544.

[230] M. H. Naik, M. Jain, *Substrate screening effects on the quasiparticle band gap and defect charge transition levels in MoS_2*. Phys. Rev. Mater. **2018**, *2*, 084002.

[231] K. Yao, A. Yan, S. Kahn, A. Suslu, Y. Liang, E. S. Barnard, S. Tongay, A. Zettl, N. J. Borys, P. J. Schuck, *Optically discriminating carrier-induced quasiparticle band gap and exciton energy renormalization in monolayer MoS_2*. Phys. Rev. Lett. **2017**, *119*, 087401.

[232] S. Gao, L. Yang, *Renormalization of the quasiparticle band gap in doped two-dimensional materials from many-body calculations*. Phys. Rev. B **2017**, *96*, 155410.

[233] Y. Liang, S. Huang, R. Soklaski, L. Yang, *Quasiparticle band-edge energy and band offsets of monolayer of molybdenum and tungsten chalcogenides*. Appl. Phys. Lett. **2013**, *103*, 042106.

[234] C. Zhang, C. Gong, Y. Nie, K. A. Min, C. Liang, Y. J. Oh, H. Zhang, W. Wang, S. Hong, L. Colombo, *Systematic study of electronic structure and band alignment of monolayer transition metal dichalcogenides in Van der Waals heterostructures*. *2D Mater.* **2017**, *4*, 015026.

[235] W. Lee, Y. Lin, L. S. Lu, W. C. Chueh, M. Liu, X. Li, W. H. Chang, R. A. Kaindl, C. K. Shih, *Time-resolved ARPES determination of a quasi-particle band gap and hot electron Dynamics in Monolayer MoS_2*. Nano Lett. **2021**, *21*, 7363.

[236] P. Giannozzi, S. Baroni, N. Bonini, M. Calandra, R. Car, C. Cavazzoni, D. Ceresoli, G. L. Chiarotti, M. Cococcioni, I. Dabo, *Quantum espresso: a modular and open-source software project for quantum simulations of materials*. J. Phys.: Condens. Matter **2009**, *21*, 395502.

[237] J. P. Perdew, K. Burke, M. Ernzerhof, *Generalized gradient approximation made simple*. Phys. Rev. Lett. **1996**, *77*, 3865.

[238] H. Shi, H. Pan, Y. W. Zhang, B. I. Yakobson, *Quasiparticle band structures and optical properties of strained monolayer MoS_2 and WS_2*. Phys. Rev. B **2013**, *87*, 155304.

[239] R. Sahu, D. Radhakrishnan, B. Vishal, D. S. Negi, A. Sil, C. Narayana, R. Datta, *Substrate induced tuning of compressive strain and phonon modes in large area MoS_2 and WS_2 van der Waals epitaxial thin films*. J. Cryst. Growth **2017**, *470*, 51.

[240] R. Guo, Q. Li, Y. Zheng, B. Lei, H. Sun, Z. Hu, J. Zhang, L. Wang, E. Longhi, S. Barlow, S. R. Marder, J. Wang, W. Chen, *Degenerate electron-doping in two-dimensional tungsten diselenide with a dimeric organometallic reductant*. Mater. Today **2019**, *30*, 26.

[241] R. Schlesinger, F. Bianchi, S. Blumstengel, C. Christodoulou, R. Ovsyannikov, B. Kobin, K. Moudgil, S. Barlow, S. Hecht, S. R. Marder, F. Henneberger, N. Koch, *Efficient light emission from inorganic and organic semiconductor hybrid structures by energy-level tuning*. Nat. Commun. **2015**, *6*, 6754.

[242] E. Mitterreiter, B. Schuler, A. Micevic, D. Hernangómez-Pérez, K. Barthelmi, K. A. Cochrane, J. Kiemle, F. Sigger, J. Klein, E. Wong, E. S. Barnard, K. Watanabe, T. Taniguchi, M. Lorke, F. Jahnke, J. J. Finley, A. M. Schwartzberg, D. Y. Qiu, S. Refaely-Abramson, A. W. Holleitner, A. Weber-Bargioni, C. Kastl, *The role of chalcogen vacancies for atomic defect emission in MoS_2*. Nat. Commun. **2021**, *12*, 3822.

[243] H. Liu, N. Han, J. Zhao, *Atomistic insight into the oxidation of monolayer transition metal dichalcogenides: from structures to electronic properties*. Rsc Adv. **2015**, *5*, 17572.

[244] S. Y. Lee, U. J. Kim, J. Chung, H. Nam, H. Y. Jeong, G. H. Han, H. Kim, H. M. Oh, H. Lee, H. Kim, Y. G. Roh, J. Kim, S. W. Hwang, Y. Park, Y. H. Lee, *Large work function modulation of monolayer MoS_2 by ambient gases*. ACS Nano **2016**, *10*, 6100.

[245] H. P. Komsa, S. Kurasch, O. Lehtinen, U. Kaiser, A. V. Krasheninnikov, *From point to extended defects in two-dimensional MoS_2: evolution of atomic structure under electron irradiation*. Phys. Rev. B **2013**, *88*, 035301.

[246] B. H. Kim, M. Park, M. Lee, S. J. Baek, H. Y. Jeong, M. Choi, S. J. Chang, W. G. Hong, T. K. Kim, H. R. Moon, Y. W. Park, N. Park, Y. Jun, *Effect of sulphur vacancy on geometric and electronic structure of MoS_2 induced by molecular hydrogen treatment at room temperature*. RSC Adv. **2013**, *3*, 18424.

[247] D. Jariwala, A. R. Davoyan, J. Wong, H. A. Atwater, *Van der Waals materials for atomically-thin photovoltaics: promise and outlook*. ACS Photonics **2017**, *4*, 2962.

[248] A. Vollmer, X. Feng, X. Wang, L. Zhi, K. Müllen, N. Koch, J. Rabe, *Electronic and structural properties of graphene-based transparent and conductive thin film electrodes*. Appl. Phys. A **2009**, *94*, 1.

[249] Y. Wu, P. Ye, M. A. Capano, Y. Xuan, Y. Sui, M. Qi, J. A. Cooper, T. Shen, D. Pandey, G. Prakash, R. Reifenberger, *Top-gated graphene field-effect-transistors formed by decomposition of SiC*. Appl. Phys. Lett. **2008**, *92*, 092102.

[250] M. Burghard, H. Klauk, K. Kern, *Carbon-based field-effect transistors for nanoelectronics*. Adv. Mater. **2009**, *21*, 2586.

[251] J. Fontanella, C. Andeen, D. Schuele, *Low-frequency dielectric constants of α-quartz, sapphire, MgF_2, and MgO*. J. Appl. Phys. **1974**, *45*, 2852.

[252] R. J. Papoular, R. Papoular, *Some optical properties of graphite from IR to millimetric wavelengths*. *Mon. Not. R. Astron. Soc.* **2014**, *443*, 2974.

[253] S.-S. Chee, C. Oh, M. Son, G.-C. Son, H. Jang, T. J. Yoo, S. Lee, W. Lee, J. Y. Hwang, H. Choi, B. H. Lee, M. H. Ham, *Sulfur vacancy-induced reversible doping of transition metal disulfides via hydrazine treatment*. Nanoscale **2017**, *9*, 9333.

[254] S. Salehi, A. Saffarzadeh, *Atomic defect states in monolayers of MoS_2 and WS_2*. Surf. Sci. **2016**, *651*, 215.

[255] M. Remškar, A. Mrzel, A. Jesih, J. Kovač, H. Cohen, R. Sanjinés, F. Lévy, *New composite MoS_2–C_{60} crystals*. Adv. Mater. **2005**, *17*, 911.

[256] L. Y. Gan, Q. Zhang, Y. Cheng, U. Schwingenschlögl, *Photovoltaic heterojunctions of fullerenes with MoS_2 and WS_2 monolayers*. J. Phys. Chem. Lett. **2014**, *5*, 1445.

[257] R. Chen, C. Lin, H. Yu, Y. Tang, C. Song, L. Yuwen, H. Li, X. Xie, L. Wang, W. Huang, *Templating C_{60} on MoS_2 Nanosheets for 2D Hybrid van der Waals p–n Nanoheterojunctions*. Chem. Mater. **2016**, *28*, 4300.

[258] Z. Song, T. Schultz, Z. Ding, B. Lei, C. Han, P. Amsalem, T. Lin, D. Chi, S. L. Wong, Y. J. Zheng, M. Y. Li, L. J. Li, W. Chen, N. Koch, Y. L. Huang, A. T. S. Wee, *Electronic properties of a 1D intrinsic/p-doped heterojunction in a 2D transition metal dichalcogenide semiconductor*. ACS Nano **2017**, *11*, 9128.

[259] X. Xu, T. Schultz, Z. Qin, N. Severin, B. Haas, S. Shen, J. N. Kirchhof, A. Opitz, C. T. Koch, K. Bolotin, J. P. Rabe, G. Eda, N. Koch, *Microstructure and elastic constants of transition metal dichalcogenide monolayers from friction and shear force microscopy*. Adv. Mater. **2018**, *30*, 1803748.

[260] I. Tanabe, M. Gomez, W. C. Coley, D. Le, E. M. Echeverria, G. Stecklein, V. Kandyba, S. K. Balijepalli, V. Klee, A. E. Nguyen, E. Preciado, I. H. Lu, S. Bobek, D. Barroso, D. Martinez-Ta, A. Barinov, T. S. Rahman, P. A. Dowben, P. A. Crowell, L.

Bartels, *Band structure characterization of WS_2 grown by chemical vapor deposition*. Appl. Phys. Lett. **2016**, *108*, 252103.

[261] M. T. Edmonds, M. Wanke, A. Tadich, H. Vulling, K. J. Rietwyk, P. L. Sharp, C. Stark, Y. Smets, A. Schenk, Q. H. Wu, L Ley, C. I. Pakes, *Surface transfer doping of hydrogen-terminated diamond by $C_{60}F_{48}$: Energy level scheme and doping efficiency*. J. Chem. Phys. **2012**, *136*, 124701.

[262] A. Opitz, A. Falchier, C. G. Yan, E. M. Yeagle, G. S. Linn, P. Megevand, A. Thielscher, R. Deborah A, M. P. Milham, A. D. Mehta, C. E. Schroeder, *Spatiotemporal structure of intracranial electric fields induced by transcranial electric stimulation in humans and nonhuman primates*. Sci. Rep. **2016**, *6*, 31236.

[263] A. Hanbicki, M. Currie, G. Kioseoglou, A. Friedman, B. Jonker, *Measurement of high exciton binding energy in the monolayer transition-metal dichalcogenides WS_2 and WSe_2*. Solid State Commun. **2015**, *203*, 16.

[264] W. T. Hsu, J. Quan, C. Y. Wang, L. S. Lu, M. Campbell, W. H. Chang, L. J. Li, X. Li, C. K. Shih, *Dielectric impact on exciton binding energy and quasiparticle bandgap in monolayer WS_2 and WSe_2*. 2D Mater. **2019**, *6*, 025028.

[265] A. Chernikov, T. C. Berkelbach, H. M. Hill, A. Rigosi, Y. Li, O. B. Aslan, D. R. Reichman, M. S. Hybertsen, T. F. Heinz, *Exciton binding energy and nonhydrogenic Rydberg series in monolayer WS_2*. Phys. Rev. Lett. **2014**, *113*, 076802.

[266] F. Zhang, A. Vollmer, J. Zhang, Z. Xu, J. Rabe, N. Koch, *Energy level alignment and morphology of interfaces between molecular and polymeric organic semiconductors*. Org. Electron. **2007**, *8*, 606.

[267] J. Choi, H. Zhang, J. H. Choi, *Modulating optoelectronic properties of two-dimensional transition metal dichalcogenide semiconductors by photoinduced charge transfer*. ACS Nano **2016**, *10*, 1671.

[268] I. G. Oliva, F. Caruso, P. Pavone, C. Draxl, *Hybrid excitations at the interface between a MoS_2 monolayer and organic molecules: a first-principles study*. Phys. Rev. Mater. **2021**, 6, 054004.

[269] T. Zhu, L. Yuan, Y. Zhao, M. Zhou, Y. Wan, J. Mei, L. Huang, *Highly mobile charge-transfer excitons in two-dimensional WS_2/tetracene heterostructures*. Sci. Adv. **2018**, *4*, eaao3104.

[270] T. R. Kafle, B. Kattel, S. D. Lane, T. Wang, H. Zhao, W. L. Chan, *Charge transfer exciton and spin flipping at organic–transition-metal dichalcogenide interfaces*. ACS Nano **2017**, *11*, 10184.

[271] P. Beyer, D. Pham, C. Peter, N. Koch, E. Meister, W. Brütting, L. Grubert, S. Hecht, D. Nabok, C. Cocchi, C. Draxl, A. Optiz, *State-of-matter-dependent charge-transfer interactions between planar molecules for doping applications*. Chem. Mater. **2019**, *31*, 1237.

[272] F. Zhang, A. Kahn, *Investigation of the High Electron Affinity Molecular Dopant F6-TCNNQ for Hole-Transport Materials*. Adv. Funct. Mater. **2018**, *28*, 1703780.

[273] M. O. Krause, J. G. Ferreira, *K X-ray emission spectra of Mg and Al*. J. Phys. B: Atom. Mol. Phys. **1975**, *8*, 2007.

8 Appendix

8.1 X-ray source parameters

Main satellite ($\mathbf{K}_{\alpha 3}$ and $\mathbf{K}_{\alpha 4}$) contributions (relative intensity and relative energy with respect to $\mathbf{K}_{\alpha 1,2}$) of the X-ray excitation sources. Mg $\mathbf{K}_{\alpha 1,2}$ = 1253.6 eV, Al $\mathbf{K}_{\alpha 1,2}$ = 1486.6 eV [273].

	Relative intensity (%)		**Relative energy shift (eV)**	
Satellite	**Mg**	**Al**	**Mg**	**Al**
$\mathbf{K}_{\alpha 3}$	9.1	7.3	8.5	9.7
$\mathbf{K}_{\alpha 4}$	5.1	3.1	10.1	11.7

8.2 Additional data

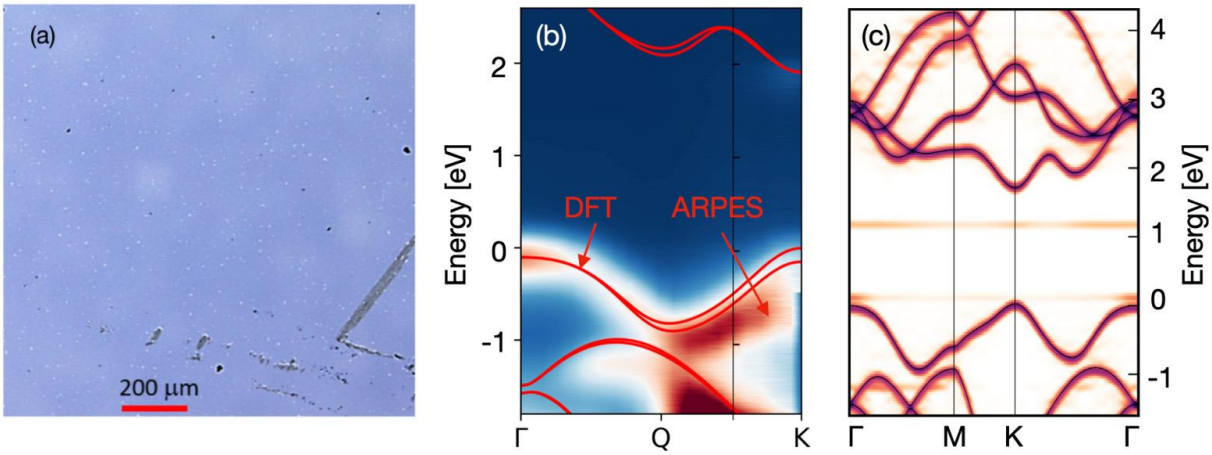

Figure 8.1. *(a) Optical micrograph of the ML-MoS_2 samples on the sapphire substrate. (b) Experimental ARPES spectral function of n-doped ML-MoS_2 on the sapphire substrate along the Γ-K path in the Brillouin zone. The ARPES plot are based on the data shown in* ***Figure 5.3*** *(h). The DFT band structure for a freestanding ML-MoS_2 is superimposed (red lines), where a scissor shift of 0.3 eV has been applied to the conduction band. The doping-induced population of the conduction band is reflected by the weak spectral intensity at K. (c) Spectral function of monolayer MoS_2 calculated using a 7×7×1 supercell with one S vacancy. The DFT band structure of pristine ML-MoS_2 is superimposed as a black line, corresponds to a carrier density of 4.6×10^{13} cm^{-2}. Figures are taken from [201]*

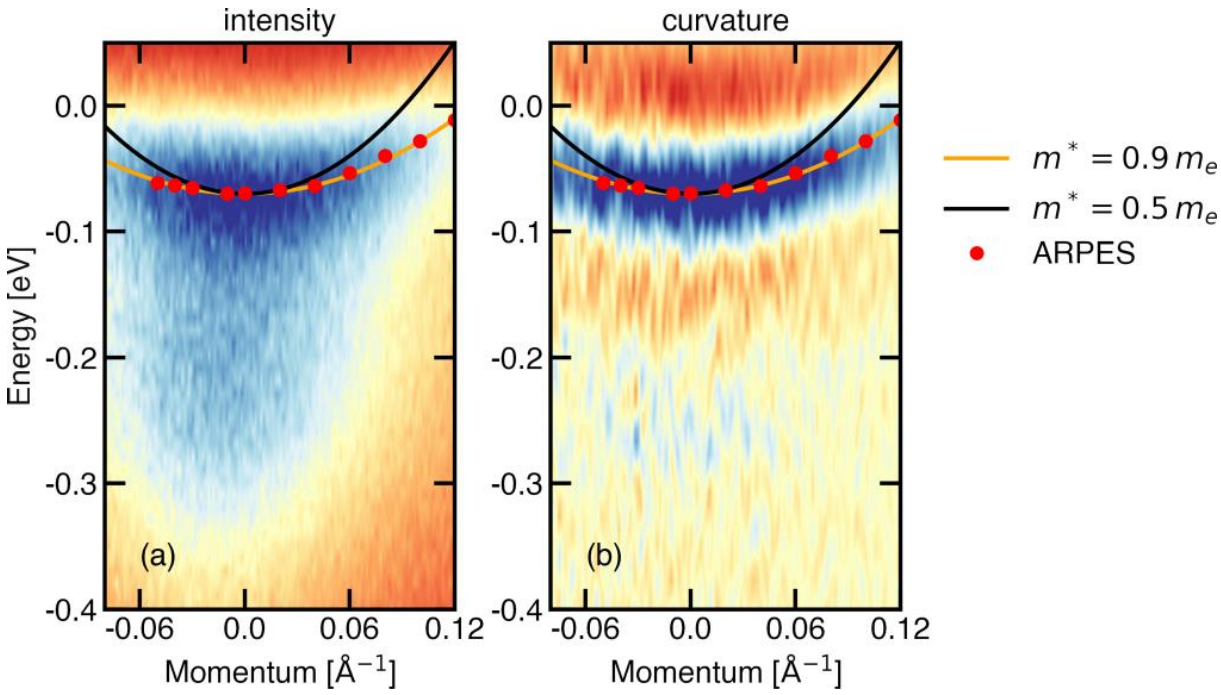

Figure 8.2 *(a) ARPES measurements of the conduction-band bottom of single-crystal ML-MoS_2 and (b) curvature of the ARPES intensity for the third annealing step. Crystal momentum is relative to the K high symmetry point. Red dots indicate the quasiparticle peak position as determined from fitting the spectral function at selected momentum. Parabolic bands with effective mass values $m^* = 0.5\ m_e$ and 0.9 m_e are included for comparison. Figures are taken from [201]*

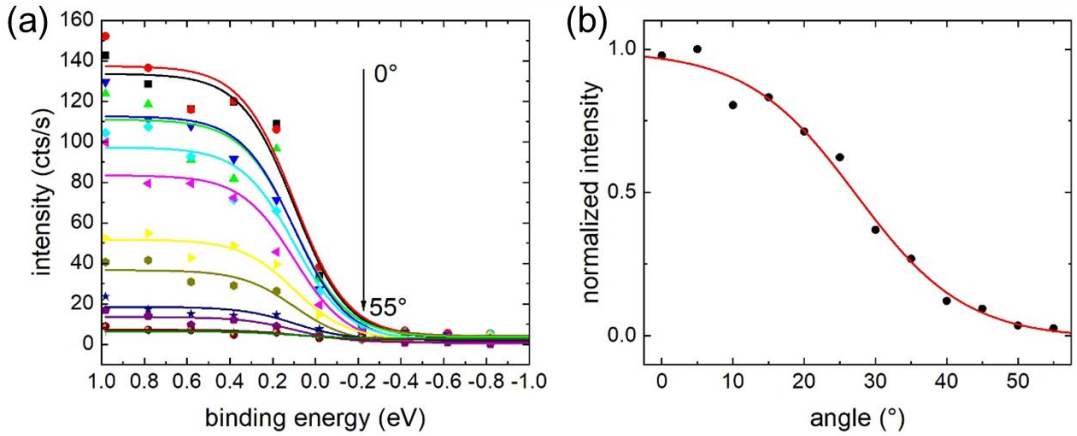

Figure 8.3 *(a) ARPES measurements of the Fermi level of a polycrystalline gold sample from 0° (normal emission) to 55°, measured every 5°. (b) Intensity attenuation of the Fermi edge as a function of angle (black dots) and best empirical fit (red curve). This attenuation has been utilized to correct the intensity of the ARPES spectra of the near E_F region in* ***Figure 5.5*** *(b, e, h) and* ***Figure 5.15*** *(b, e, g, i).*

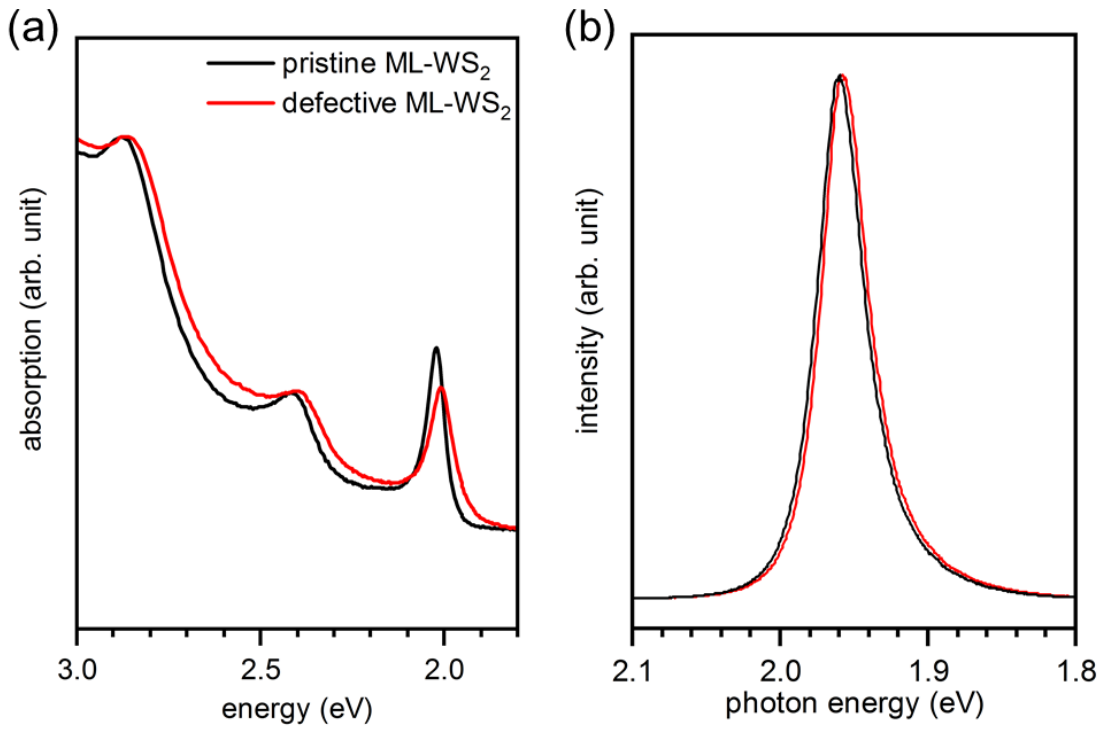

Figure 8.4 *(a) Absorption and (b) PL spectra of pristine (black curve) and defective (red curve) ML-WS_2 in air. The intensity is normalized for better clarity.*

Publications

1. **J. Ma**, P. Amsalem, T. Schultz, D. Shin, X. Xu, N. Koch, *Energy level alignment at the C_{60}/Monolayer-WS_2 interface on insulating and conductive substrates*. Adv. Electron. Mater. **2021**, *7*, 2100425
2. F. Caruso, P. Amsalem, **J. Ma**, A. Aljarb, T. Schultz, M. Zacharias, V. Tung, N. Koch, C. Draxl, *Two-dimensional plasmonic polarons in n-doped monolayer MoS_2*. Phys. Rev. B **2021**, *103*, 205152.
3. J. Shang, T. Feng, S. Zhao, T. Li, **J. Ma**, X. Xu, N. Koch, J. Zhao, *Chemical vapor deposition synthesized monolayer* MoS_2 *for Q-switching pulse generation in the 2 μm spectral region*. Opt. Mater. Express **2020**, *10*, 2321.
4. J. Ma, P. Amsalem, X. Xu, Q. Wang, R. B. Wang, N. Koch, *Direct observation of charge transfer within the F_6TCNNQ-WS_2 van der Waals interface*. In preparation.
5. P. Amsalem[#], **J. Ma**[#] (first co-author), A. Aljarb, F. Caruso, B. Haas, X. Xu, D. Shin, A. Aljarb, E. Longhi, S. Barlow, S. R. Marder, C. Koch, C. Draxl, V. Tung, S. Park and N. Koch, *Sulfur-vacancy induced band structure renormalization and doping of monolayer MoS_2 and WS_2*. In preparation.

Acknowledgements

First of all, I would like to sincerely thank my two supervisors Prof. Emil List-Kratochvil and Prof. Norbert Koch, who provided me the opportunity to pursue my PhD study at Humboldt Universität zu Berlin. Thank you for providing support in every respect and huge expertise in the field of semiconductors. I would thank for financial support through the IMPRS, the SFB951 and HZB.

I want to thank all my colleagues from Supramolecular Systems for their support over the past four years. In particular, I would like to thank Dr. Patrick Amsalem and Dr. Fengshuo Zu for numerous discussions and supports. A big thank you goes to Dr. Xiaomin Xu and Dr. Soohyung Park for helping start my project.

I want to thank all my friends who supported me during these many years.

Finally, I want to thank my family for their unconditional love and support for me.

Selbstständigkeitserklärung

Hiermit erkläre ich, die Dissertation selbstständig und nur unter Verwendung der angegebenen Hilfen und Hilfsmittel angefertigt zu haben. Ich habe mich nicht anderwärts um einen Doktorgrad in dem Promotionsfach beworben und besitze keinen entsprechenden Doktorgrad. Die Promotionsordnung der Mathematisch-Naturwissenschaftlichen Fakultät, veröffentlicht im Amtlichen Mitteilungsblatt der Humboldt-Universität zu Berlin Nr. 42 am 11. Juli 2018, habe ich zur Kenntnis genommen.

Jie Ma
Berlin 03.06.2022